2019

Fiber-based high energy ultrafast sources for nonlinear microscopy

BOSTON UNIVERSITY

COLLEGE OF ENGINEERING

Dissertation

FIBER-BASED HIGH ENERGY ULTRAFAST SOURCES FOR NONLINEAR MICROSCOPY

by

BOYIN TAI

B.S., Nankai University, 2008
M.S.E., Nankai University, 2011

Submitted in partial fulfillment of the

requirements for the degree of

Doctor of Philosophy

2019

Approved by

First Reader

Siddarth Ramachandran, Ph.D.
Professor of Electrical and Computer Engineering
Professor of Materials Science and Engineering

Second Reader

David Boas, Ph.D.
Professor of Biomedical Engineering
Professor of Electrical and Computer Engineering

Third Reader

Jerome C. Mertz, Ph.D.
Professor of Biomedical Engineering
Professor of Electrical and Computer Engineering

Fourth Reader

Ji-Xin Cheng, Ph.D.
Moustakas Chair Professor in Optoelectronics and Photonics
Professor of Biomedical Engineering
Professor of Electrical and Computer Engineering
Professor of Materials Science and Engineering
Professor of Chemistry
Professor of Physics

Acknowledgements

The work covered in this thesis has been made possible through the support from funding agencies, including Office of Naval Research (ONR), Air Force Office of Scientific Research (AFOSR), and National Institutes of Health (NIH).

I would like to thank my advisor, Professor Siddharth Ramachandran, for giving me the opportunity to work in his lab on exciting research projects, and providing his guidance during the entire course of my research. Every time I have difficulty in understanding my experimental data or figuring out how to solve a problem, he is patient to have insightful discussion with me, not only pointing out the directions for tackling the specific issues, but also instilling me the scientific ways of thinking. Without the constant and deep discussion, it is impossible for me to finish the work presented in the thesis.

I would like to thank our collaborators for their great help to advance the work. Many thanks to Dr. Poul Kristensen at OFS Fitel, LLC. in Denmark for fabricating the high numerical aperture (NA) step-index multimode fibers (MMFs) that have been used in almost all of my work. Many thanks to Professor Govind P. Agrawal and his student Aku Antikainen at University of Rochester, who have simulated the interpulse intermodal Raman scattering process, helping us to get a better understanding on the phenomenon.

Many thanks to my committee members, Professor David Boas, Professor Jerome Mertz, and Professor Ji-Xin Cheng, for being patient and willing to spend time and effort evaluating and aiding this work.

I would like to thank all my group members, past and present. Special thanks to Dr. Lars Rishøj for his help on my experiments. He has taught me lots of basic but important

experimental skills, such as using the spatial light modulator (SLM) to purely excite a specific fiber mode. He has also given me some detailed, specific and very useful advice based on his experience, such as the proper cutback fiber length. We constantly have exciting discussion on each other's experimental observation, and try solving problems together. I have been surprised more than once by his great patience in helping and teaching others, including myself and any other person in our group. Thanks to Dr. Paul Steinvurzel, Dr. Michael Grogan, Dr. Nenad Bozinovic, Yuhao Chen, Dr. Lu Yan, Dr. Jeffery Demas, Dr. Patrick Gregg, Kris Goldizen, Gautam Prabhakar, Asher McGuffin, Dr. Debangshu Mukherjee, Dr. Mustafa Ordu, Kasper Ingerslev, Dr. Tao He, Dr. Duri Song, Dr. Geo Muppathiyil, Guang Yang, Xiao Liu, Zelin Ma, Dr. Xinglin Zeng, Dr. Niharika Singh, Havva Kabagoz, and Erik Christensen, for their help and support.

Thanks to all my friends for their continued support.

Thanks to Kevin Kern for his beautiful music, especially the album *In the Enchanted Gauden*, which accompanied me through the entire thesis writing.

Thanks to my girlfriend, Xi Meng, for her company and support. Finally, I would like to thank my families, especially my parents and grandmother, for their endless and immeasurable love, support and encouragement, which have helped me to get through with the hard times in the past several years.

FIBER-BASED HIGH ENERGY ULTRAFAST SOURCES

FOR NONLINEAR MICROSCOPY

BOYIN TAI

Boston University, College of Engineering, 2019

Major Professor: Siddharth Ramachandran, Ph.D., Professor of Electrical and Computer Engineering, Professor of Materials Science and Engineering

ABSTRACT

Nonlinear microscopy (NM) techniques are important for biologists. For example, two-/three-photon excited fluorescence (2PEF/3PEF) microscopy helps deep visualization of the brain; and coherent anti-Stokes Raman scattering (CARS) and stimulated Raman scattering (SRS) allow the acquisition of chemical information in biological tissues. However, in contrast to conventional, linear microscopy, the minuscule cross-sections of nonlinear interactions require the use of specialized high energy ultrafast sources. Furthermore, in order to reduce scattering and heating related problems, ~1300 nm is the preferred imaging wavelength window, given maximal tissue transparency. Currently, these requirements are met by commercial solid-state optical parametric oscillators (OPOs) and optical parametric amplifiers (OPAs), which are bulky, costly, require significant user-expertise for operation, and often yield non-perfect (i.e. non-Gaussian-shaped) beam profiles.

Fiber-based sources are alternative options. They are alignment-free, lightweight, compact, cost-effective, and have high output beam quality (perfect Gaussian or a pure higher order mode (HOM)). Moreover, the flexibility of a fiber can be exploited to

implement endoscopy, which enables imaging studies in freely moving animals. In these schematics, a commercial, alignment-free fiber laser can be combined with another specialty fiber that utilizes its own nonlinear interactions to produce pulses, on-demand, at user-desired wavelengths. One such effect is soliton self-frequency shift (SSFS)—an intrapulse Raman scattering process in optical fibers—using which one can continuously transfer energy to longer wavelengths, such as from ~1050 nm (Yb fiber laser wavelength) to a desired target wavelength (e.g. ~1300 nm). SSFS using HOMs in step-index multimode fibers (MMFs) has been demonstrated to generate pulses with pulse energies of ~30 nJ and peak powers of ~0.5 MW at ~1300 nm. More recently, using both SSFS and an intermodal interpulse Raman scattering process called soliton self-mode conversion (SSMC), strong pulses with pulse energies of ~80 nJ and peak powers of ~1.1 MW have been generated at ~1300 nm. The efficacy of this fiber-based source generation technique has been validated by the fact that it has been successfully utilized for acquiring 3PEF images from mouse brain samples.

In this thesis, we conduct an in-depth study of this newly discovered SSMC phenomenon. We show that this effect can be cascaded to produce multiple temporally aligned, but spectrally separated pulses, as may be needed from schematics that use more than one excitation or readout source, and that it can be extended across wide bandwidths, satisfying the needs of multiple microscopy applications. Salient results we have obtained include the following: (1) both higher input powers and longer fiber lengths keep lowering the mode order, and at the same time red-shifting the soliton wavelength, without loss of spatial coherence; (2) group refractive index matching plays a key role, and hence this process can

be controlled by simple fiber design; (3) pump-to-soliton energy conversion efficiencies are ≥ ~30%, and inter-soliton conversion always results in the transfer of ~100% of the photons; and (4) these attributes can be combined to yield wavelength translations as much as ~62% of the carrier wavelength (1045-1696 nm), with further translation currently limited by the pump power available in the lab, and ultimately by the self-action/dielectric breakdown effect in the fiber.

The second focus of the thesis is using the SSFS process to develop a compact fiber-based dual color source for CARS/SRS microscopy. In the Stokes arm, the HOM excitation and HOM-to-Gaussian conversion are both implemented using commercially available physical axicons. The pump output is at 1045nm, with a pulse energy of ~400 nJ and peak power of ~4 MW. The Stokes output is tunable from 1339 nm to 1376 nm, with a pulse energy of ~14.5 nJ and peak power of ~0.2 MW.

Finally, we conduct theoretical simulations, based on initial conditions obtained from experimental values, on the prospects of using SSFS and SSMC in MMFs for further power-scalability and wider wavelength tunability. We find that the power scaling by way of dispersion-area product scaling is ultimately limited by the fiber numerical aperture (NA) and self-action/dielectric breakdown. However, the soliton pulse energy/peak power can still potentially approach the level of commercial solid-state OPOs/OPAs. Furthermore, the SSFS/SSMC mechanisms can also be applied in fluoride and chalcogenide glass fibers to generate strong pulses in the mid infrared (MIR) range.

Our study indicates SSFS and SSMC in step-index MMFs are effective ways to generate high energy, ultrafast pulses covering both near infrared (NIR) and MIR windows. This

source can be useful for nonlinear microscopy, endoscopy, spectroscopy, chemical sensing, and potentially offer an attractive alternative to bulk, alignment-sensitive OPOs and OPAs that are currently the only known options for high-power source development at wavelengths where lasing gain media do not exist.

Contents

List of Tables

List of Figures

List of Abbreviations

ANDi	all-normal-dispersion
BPF	band-pass filter
BPP	binary phase plate
CARS	coherent anti-Stokes Raman scattering
DCF	dispersion compensation fiber
ECL	external cavity laser
FMF	few-mode fiber
FT	Fourier transform
FUT	fiber under test
FWHM	full width at half maximum
FWM	four-wave mixing
GNLSE	generalized nonlinear Schrödinger equation
GRIN	graded-index
GVD	group velocity dispersion
HCPBGF	hollow-core photonic bandgap fiber
HOM	higher order mode
InGaAs	Indium-Gallium-Arsenide
LP	linearly polarized
LPF	long-pass filter
LPFG	long period fiber grating
MIR	mid infrared
MMF	multimode fiber
MPI	multipath interference
NA	numerical aperture
NIR	near infrared
NM	nonlinear microscopy
OI	overlap integral

OPA ..... optical parametric amplifier
OPO ..... optical parametric oscillator
OSA ..... optical spectrum analyzer
PBS ..... polarization beam splitter
PCF ..... photonic crystal fiber
RTJ ..... relative timing jitter
SHG ..... second-harmonic generation
SLM ..... spatial light modulator
SMF ..... single mode fiber
SNR ..... signal to noise ratio
SPM ..... self-phase modulation
SRS ..... stimulated Raman scattering
SSFS ..... soliton self-frequency shift
SSMC ..... soliton self-mode conversion
TAP ..... turn-around point
THG ..... third-harmonic generation
2PEF ..... two-photon excitation fluorescence
3PEF ..... three-photon excitation fluorescence

Chapter 1

Introduction

1.1 From linear to nonlinear microscopy

Since the fluorescence microscopy was invented, it has become possible to image the cellular, subcellular and molecular structures inside biological tissues with high contrast between the target (signal) and other (background noise) regions (Lichtman and Conchello, 2005). With the discovery (Shimomura et al., 1962) and subsequent extensive, successful development (Chalfie et al., 1994; Heim et al., 1995) of green fluorescence protein (GFP) and its derivatives (fluorescence labels that are much less harmful to living cells and that can be genetically tagged to protein components inside living biological systems), fluorescence microscopy has been more and more used to study living cells, such as in vivo detection of gene expression, and monitoring the locations and transportation of host proteins (Tsien, 1998).

While the fluorescence microscopy offers great imaging contrast, for a long time, scientists could only observe thin specimens or superficial layers of thick specimens. Meantime there was strong desire in deep tissue imaging in biological and medical areas. For example, in neuroscience researchers needed a noninvasive imaging tool to look inside the brain to understand more about the structure, function and dynamic activity of the nervous system at a cellular/subcellular level and then improve the diagnosis and treatment of brain diseases, such as Alzheimer's disease. The contradiction between the desire and lack of deep tissue imaging technique has been mitigated by the nonlinear microscopy

(NM), which uses a fundamentally different manner of light-matter interaction than the traditional linear microscopy. The typical linear microscopy techniques include widefield

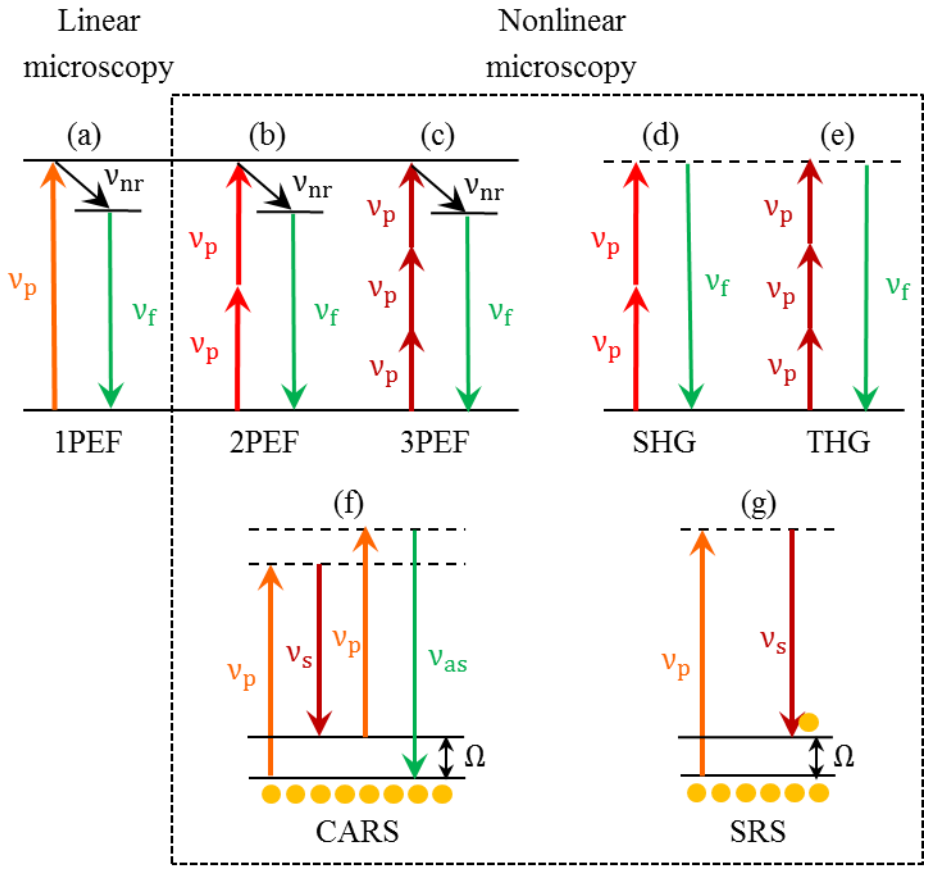

Figure 1.1: Jablonski diagram of (a) linear microscopy, including widefield and confocal, (b) 2PEF, (c) 3PEF, (d) SHG, (e) THG, (f) CARS, and (g) SRS. All the imaging techniques inside the dotted line box belong to nonlinear microscopy. Solid line: read energy level, dashed line: virtual energy level, solid yellow circle: vibrational mode, ν_p: pump frequency, ν_f: fluorescence frequency, ν_{nr}: nonradiative transition frequency, ν_s: Stokes frequency, ν_{as}: anti-Stokes frequency, Ω: Raman-active molecular vibration frequency.

and confocal microscopy (Minsky, 1957; Pawley, 2006), and NM generally consists of two-photon excitation fluorescence (2PEF) (Denk et al., 1990; Helmchen and Denk, 2005), three-photon excited fluorescence (3PEF) (Gryczynski et al., 1995; Horton et al., 2013; Ouzounov et al., 2017), second-harmonic generation (SHG) (Freund and Deutsch, 1986;

Campagnola and Loew, 2003), and third-harmonic generation (THG) microscopy (Barad et al., 1997; Weigelin et al., 2016). The Jablonski diagrams of light-matter interactions used by these techniques are shown in Fig. 1.1. As seen in the figure, the linear microscopy is based on the process in which only one photon from the excitation light interacts with the specimen to obtain one photon at the signal wavelength. In contrast, the NM is based on the processes in which more than one photon from the excitation light is involved to obtain one photon at the signal wavelength.

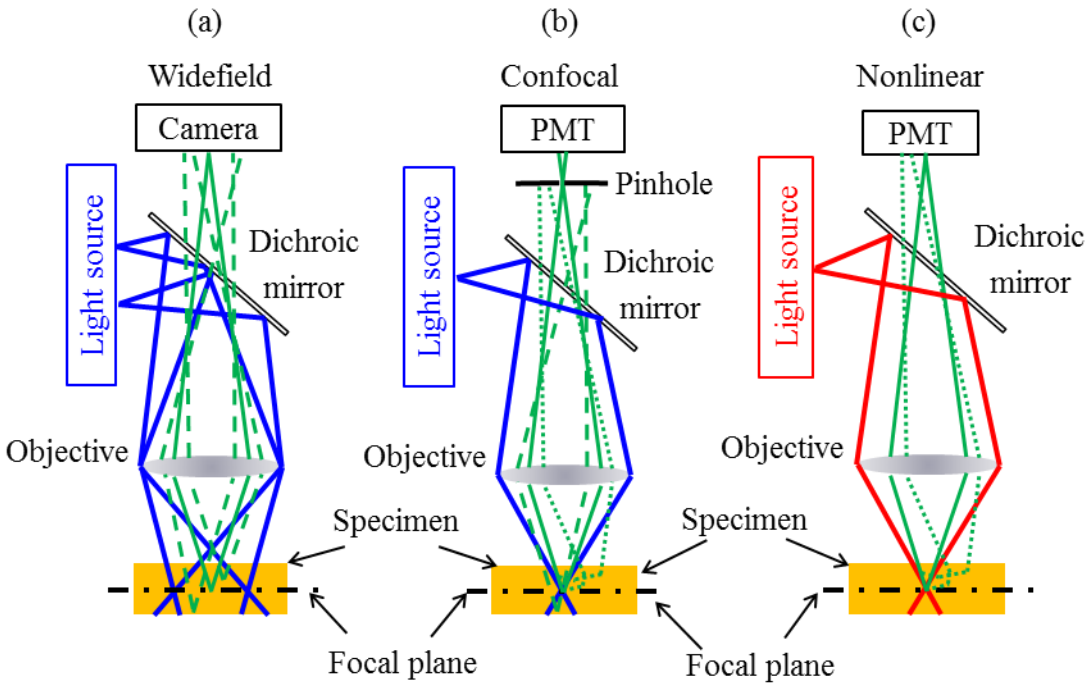

Figure 1.2: Schematic configuration of (a) widefield microscopy, (b) confocal microscopy, and (c) nonlinear microscopy. The solid green lines represent the signal received by the detector. The dashed green lines represent the light at the signal wavelength, but emitted from out-of-focus regions. The dotted lines represent the scattered signal light.

Signal to noise ratio (SNR) is the parameter determining the capability of a microscopy technique to implement deep tissue imaging. In the widefield microscopy setup, the

excitation light illuminates a large area of the specimen, and the fluorescence generated within this entire area is collected by the objective and imaged onto the camera. The advantage of widefield microscopy is the fast imaging speed. However, this technique is only applicable to thin specimens (<5 μm) (Combs and Shroff, 2017). For a thick specimen, as shown in Fig. 1.2(a), the entire illumination region, including both the focal (desired) and the out-of-focus (undesired) planes, emits fluorescence, and thus both signal (solid green lines in Fig. 1.2(a)) and background noise (dashed green lines in Fig. 1.2(a)) enter the camera, resulting in low SNR.

In order to get imaging depth information, confocal microscopy was invented (Minsky, 1957). The key element in this technique is the pinhole placed in front of the detector. As shown in Fig. 1.2(b), the pinhole is in the conjugate image plane to the focus of excitation light inside the sample, so only the fluorescence signal from the focus (solid green lines in Fig. 1.2(b)) is seen by the detector. All the other fluorescence (dashed green lines in Fig. 1.2(b)) are almost blocked. Using this method, optical sectioning capability along the depth direction is achieved, but the imaging depth is generally limited to only ~100 μm (Combs and Shroff, 2017). The reason originates from the strong scattering property of biological tissues (Taddeucci et al., 1996). Due to the scattering, only the ballistic photons of the excitation light reach the focus and generate the desired fluorescence, this is essentially equivalent to the loss of fluorescence signal. In addition, part of the desired fluorescence does not appear to come from the focus due to the scattering (dotted green lines in Fig. 1.2(b)), and thus cannot pass through the pinhole, also resulting in the loss of signal. Furthermore, the fluorescence from out-of-focus regions can be scattered and appears to

be emitted from the focus and then received by the detector, increasing the background noise. Therefore, the effect of scattering is lowering the SNR, and this problem becomes more serious with increasing imaging depth.

The shallow imaging depth issue is mitigated by using the nonlinear imaging (Fig. 1.2(c)) techniques based on three reasons (Helmchen and Denk, 2005). 1) Due to the involvement of more than one excitation photon to generate the signal, the wavelength(s) of excitation light(s) generally fall(s) in the near-infrared window. Compared with visible light used in the linear microscopy, near-infrared light is less susceptible to scattering, i.e. more excitation photons reach the focus. 2) Due to the need of high intensity to excite the nonlinear light-matter interaction, the desired signal (solid and dotted green lines in Fig. 1.2(c)) is generated mainly from the focus, i.e. there is much less background noise from the out-of-focus regions than linear microscopy. 3) Based on reason 2), there is no need to put a pinhole in front of the detector. Instead, a detector with a large sensing area is desired, and as much fluorescence as possible should be collected. Simply speaking, compared with confocal microscopy, NM improves SNR. In addition, NM benefits from that photobleaching is confined in the focal plane rather than distributed across the entire illumination region like in the linear microscopy (Denk et al., 1990; Helmchen and Denk, 2005).

Chemical information is also very important for the biologists studying the metabolism of living cells. Fluorescence labels are attached to specific targets, but the broadband and featureless fluorescence spectra limit the number of resolvable chemical contents (Wei et al., 2017). Instead, Raman scattering is a good mechanism for chemical discrimination due

to the nature of narrow bandwidth of molecular vibration energy level. Spontaneous Raman microscopy (Abraham and Etz, 1979) was used in the past, but because of the weak signal and slow image acquisition, nowadays it has been substituted by its coherent counterpart, including coherent anti-Stokes Raman scattering (CARS) (Duncan et al., 1982; Zumbusch et al., 1999; Zhang and Cheng, 2018) and stimulated Raman scattering (SRS) microscopy (Ploetz et al., 2007; Freudiger et al., 2008; Zhang and Cheng, 2018), whose Jablonski diagrams are shown in Fig. 1.1(f) and (g).

1.2 From bulky solid-state to flexible fiber laser

1.2.1 Commercial solid-state laser for nonlinear microscopy

High excitation power is needed in NM due to the minuscule interaction cross-section (Xu and Wise, 2013). Indeed, the widespread use of NM did not begin until the advent of mode-locking ultrafast solid-state lasers (Negus et al., 1991; Spence et al., 1991). In the early experiments, Ti:sapphire laser, such as Mai Tai of Spectra-Physics, was the main excitation source (wavelength range: 710-920 nm, pulse energy: ~5-20 nJ, pulse duration: <100 fs, peak power: ~0.05-0.2 MW, repetition rate: 80 MHz). Using this type of laser, the status of Alzheimer's disease was visualized based on 2PEF microscopy (Bacskai et al., 2001), and three-dimensional high spatial resolution CARS imaging was achieved (Zumbusch et al., 1999).

The high peak power is not the only factor affecting the imaging depth. Both theoretical and experimental work showed that the maximal imaging depth of 2PEF could be improved using excitation sources with larger scattering lengths, higher peak powers and lower duty

cycles (Oheim et al., 2001; Theer and Denk, 2006; Balu et al., 2009; Kobat et al., 2009). Based on this rule, 2PEF imaging depth of 1 mm was demonstrated (Theer et al., 2003) using a regenerative amplifier that featured high peak power and low repletion rate (center wavelength: 925 nm, pulse energy: 3 μJ, pulse duration: ~150 fs, peak power: ~20 MW, repetition rate: 200 kHz). By using a longer wavelength excitation source (1280 nm), a record 2PEF imaging depth of 1.6 mm was realized (Kobat et al., 2011). The source used in the experiment was an optical parametric oscillator (OPO) (wavelength range: 1100-1600 nm, pulse energy: >6 nJ, pulse duration: 140 fs, peak power: >0.04 MW, repetition rate: 80 MHz).

There is one more factor affecting the maximal imaging depth, i.e. absorption, since it influences how much excitation power can reach the focus (Horton et al., 2013). Because the absorption inside tissues is mainly from water content, it basically becomes stronger with wavelength. On the other hand, it is known the scattering becomes weaker with wavelength. Therefore, in terms of penetration depth the optimal excitation wavelength windows are determined by the trade-off between the scattering and absorption. Theoretical calculation and experimental measurement showed the optimal windows are around 1300 nm and 1700 nm, which have similar effective attenuation lengths (a characteristic length considering the influence from both scattering and absorption) (Horton et al., 2013). Between these two windows, 1300 nm window should be better, because of 1) less absorption and resultant weaker heating issue on the biological specimens, and 2) having access to more fluorescence labels, such as GFP, for fluorescence microscopy.

Based on the above knowledge accumulated over the past decades, an ideal excitation source for NM techniques using only one excitation beam should deliver a pulse train with wavelength access to 1300 nm and/or 1700 nm, pulse energy of >>10 nJ, pulse duration <100 fs, peak power > ~1 MW, and repetition rate that is as high as possible in order to get fast image acquisition as long as there is no specimen heating issue (Xu and Wise, 2013). This standard has led the recent rapid improvement of the commercial solid-state lasers (OPO and optical parametric amplifier (OPA)). The representative products are Spirit-NOPA-IR of Spectra-Physics (1200-1600 nm, 600 nJ @ 1300 nm, <80 fs, >7.5 MW @ 1300 nm, 2 MHz) and Opera-F of Coherent (1200-2500 nm, ~1000 nJ @ 1300 nm & ~750 nJ @ 1700 nm, <100 fs, >~10 MW @ 1300 nm & >~7.5 MW @ 1700 nm, 2 MHz).

For CARS and SRS, the requirements (Xu and Wise, 2013) are a little more complicated because of the need of two excitation beams. 1) The wavelength of at least one source should be tunable in order to selectively excite a specific molecular Raman peak. 2) If the deep imaging is needed, the wavelength of at least one source should be around 1300 nm or 1700 nm. 3) The two excitation beams should be synchronized in order to reach the focus at the same time. The timing jitter should be only a small fraction of the pulse durations. 4) Both beams should have high peak power to efficiently start the nonlinear process. 5) The repetition rate should be as high as possible to get fast imaging as long as there is no specimen heating issue. One typical commercial laser for CARS/SRS is an OPO system from Spectra-Physics (Insight X3, arm 1 (pump arm): 1045 nm, > ~44 nJ, < 200 fs, > ~0.2 MW, 80 MHz; arm 2 (Stokes arm): 680-1300 nm, > ~19 nJ, < 120 fs, > ~0.2 MW, 80 MHz).

1.2.2 Alternative to bulky solid-state laser—fiber source

Although the solid-state lasers can provide high peak power pulses within the optimal windows, they are bulky, costly, have non-perfect output beam shape (non-Gaussian shaped profile), and need precise alignment. These factors tie their use mainly to research labs. An alternative option is fiber-based source, which is lightweight, compact, without the need of alignment due to the nature of waveguide, has a perfect output beam shape (a perfect Gaussian or a pure higher order mode (HOM)), and cost less than solid-state lasers. More importantly, with a fiber-based source it is possible to implement nonlinear endoscope and image the neuron activities in freely moving animals (Helmchen et al., 2013; Ozbay et al., 2018).

The performance, especially output peak power and wavelength tunability, of fiber lasers has historically fallen behind the solid-state products until the recent demonstration of all-normal-dispersion (ANDi) fiber laser (Chong et al., 2006), which formed a stable intracavity dissipative soliton with the pules energy at least one order of magnitude higher than the tradition soliton lasers. Along with lots of following effort, ANDi laser was the first fiber laser reaching the power level of a standard Ti:sapphire laser (Kieu et al., 2009). In this work after pules compression the laser emitted pulses with energy of 20 nJ and duration of 80 fs. Afterwards, the output peak power was improved to 1 MW (Lefrancois et al., 2010) and even 6 MW (Baumgartl et al., 2012), by using a Yb-doped large-mode-area photonic crystal fiber (PCF) and a PCF rod, respectively. However, the wavelength range of ANDi lasers is locked to ~1000-1100 nm, which is determined by the emission spectral range of Ytterbium—the rare earth dopant used as the gain medium in active fibers

(Paschotta et al., 1997). While NM has been demonstrated using ANDi laser (Liu et al., 2011; Wise, 2012), the benefit of optimal excitation wavelength windows for deep tissue imaging was not utilized and the effort to push the wavelength of fiber lasers to these windows was still needed.

One solution is using a fiber to deliver 1300 nm and/or 1700 nm light from OPO/OPA to biological specimens. In this configuration, the optical fiber is basically a light transportation medium. The pulse laser delivery has been studied in different fibers. In the cases of solid-core large-mode-area PCF (Ouzounov et al., 2002) and high dispersion fiber (Ramachandran et al., 2005), the pulse energy was limited to 3 nJ with pulse duration of ~150 fs before introducing significant temporal and spectral distortion. In the case of hollow-core photonic bandgap fiber (HCPBGF) (Gobel et al., 2004), the distortion-free pulse delivery with energy of 4.6 nJ and duration of 170 fs was demonstrated. It is expected that by using HCPBGF even stronger pulses can be delivered with no or slight distortion, but no continued work has been reported. Perhaps the high coupling loss (~3 dB), fragile fiber facet and the difficulty of splicing it to the other types of fibers hindered the further development.

Another way to get around the wavelength limitation is using optical fibers as both nonlinearity and transportation media, i.e. the 1300 nm and/or 1700 nm light is generated inside the fiber based on nonlinear processes and then emitted at the fiber output end. Different fiber-based nonlinear processes have been investigated. The OPO based on four-wave mixing (FWM) in normally dispersive PCF generated high energy pulses (250 nJ) at 1250 nm, but the pulse duration was long (960 fs), resulting in relatively low peak power

(~0.3 MW) (Gottschall et al., 2015). Besides, in this configuration the pulses out of fiber had to be put in a grating pair for compression, which weakened the alignment-free benefit of fiber systems. Self-phase modulation (SPM) effect was exploited to broaden the spectrum of pump toward the optimal windows (Liu et al., 2016; Liu et al., 2017), and strong pulses were acquired at both 1300 nm (130 nJ, 94 fs, ~1.4 MW) and 1700 nm (110 nJ, 150 fs, ~0.7 MW), but the fiber length was only 1.3 cm in order to mitigate the dispersion effect (Chung et al., 2018). Such a short fiber does not possess the flexibility nature of optical fibers any more, and thus there is no way to use this type of system to implement endoscopy. An alternative nonlinear process, i.e. soliton self-frequency shift (SSFS) (Mitschke and Mollenauer, 1986), was also exploited. In this process, short transform-limited pulses (Raman solitons) with duration of <~100 fs (indicating the potential high peak power) can be generated with fiber length at least tens of centimeters, so SSFS is a promising mechanism for building up an endoscopy-compatible fiber source. Lots of work has been done on SSFS using single mode waveguides (Beaud et al., 1987; Liu et al., 2001), and the excellent result has been demonstrated around 1700 nm (Horton et al., 2013). Using SSFS in a 35 cm PCF rod, the strong pulses were generated at 1675 nm (67 nJ, 65 fs, ~1 MW), which was then used to implement 3PEF within an intact mouse brain, achieving ~1.4 mm imaging depth and high-resolution neuron images in hippocampus (Horton et al., 2013). However, the performances of SSFS demonstrations in SMFs around 1300 nm were not satisfying. The pulses generally had energies of <1 nJ and peak power of <10 kW (Cormack et al., 2002; Lim et al., 2004; Takayanagi et al., 2006).

The limitation on Raman soliton energy/peak power around 1300 nm in SMFs comes

from that waveguide dispersion and effective mode area are coupled to each other for the fundamental mode (This coupling relation will be discussed in details in chapter 2) (Ramachandran et al., 2008). Simply speaking, in order to form a soliton in the fundamental mode for wavelength ≤ ~1300 nm, the fiber core or effective mode area need to be very small (<10 μm^2) (Cormack et al., 2002; Lim et al., 2004; Takayanagi et al., 2006). Because the soliton energy is proportional to effective mode area, low energy is expected (van Howe et al., 2007; Lee et al., 2008). Also, small core size indicates weak power handling capability, i.e. the fiber is more easily damaged by dielectric breakdown. Fortunately, the requirement of small core size does not apply to HOMs (Ramachandran et al., 2008). This important difference between fundamental mode and HOMs has motived the researchers to start using multimode fibers (MMFs) to implement SSFS, trying to generate strong pulses around 1300 nm (van Howe et al., 2007). Indeed, by using HOMs the strong soliton (~30 nJ, ~0.5 MW) at 1317 nm has been achieved (Rishoj et al., 2016). Recently, using both SSFS and an intermodal inerpulse Raman scattering process called soliton self-mode conversion (SSMC), even stronger pulses (~80 nJ, ~1.1 MW) were generated at ~1300 nm (Rishoj et al., 2018).

1.3 From single mode fiber to multimode fiber

It is not a completely new regime to implement HOM nonlinear processes. The early demonstrations of FWM achieved phase-matching by using HOMs (Stolen et al., 1974; Stolen, 1975). However, the impure mode excitation and unstable mode propagation prevented the HOM platform developing further. With the subsequent advent of low-loss

SMFs, the attention was transferred to this simpler but more reliable platform (Marhic et al., 1996), which was the reason why the early SSFS was mainly investigated in SMFs.

The recent demonstration of HOMs (so-called Bessel-like $LP_{0,m}$ (Steinvurzel et al., 2011) and OAM modes (Bozinovic et al., 2012)) being able to propagate stably over long distances (Ramachandran et al., 2006b; Bozinovic et al., 2013; Gregg et al., 2016) based on proper fiber design, combined with the application of free-space Bessel and OAM beams in the areas of free-space communication (Wang et al., 2012), volumetric imaging (Lu et al., 2017), and particle manipulation (McGloin and Dholakia, 2005), has led to the resurgence of HOMs. Indeed, lots of research has been done using HOMs, consisting of high power fiber amplifier (Nicholson et al., 2012), monomode (Demas et al., 2017) and intermodal (Demas et al., 2018) FWM, ultrafast nonlinear dynamics (Rishoj et al., 2016; Rishoj et al., 2018), mode division multiplexing telecommunication (Bozinovic et al., 2013), supercontinuum generation (Prabhakar et al., 2016), phase conjugation via stimulated Brillouin scattering (Prabhakar et al., 2018), and fiber-based stimulated emission depletion microscopy (Yan et al., 2016).

It needs to be mentioned that among all the HOM-based applications listed above, different types of MMFs were used, including step-index MMFs, graded-index (GRIN) MMFs, solid-core and air-core vortex fibers. The effective mode area of vortex fibers is relatively small, so it is not a good choice to generate strong soliton pulses using this type of fibers. GRIN MMFs have shown some interesting phenomenon, such as spatial beam self-cleaning (Krupa et al., 2017) and strong pulse generation based on soliton entity (Wright et al., 2015), but due to the unstable mode propagation and impure mode launching

in those experimental work, the output is either a low quality Gaussian-like beam with M^2 ≥ ~4 or speckly, looking like the interference pattern among multiple modes, and thus inappropriate to be used for microscopy that has strict requirements on beam quality. Step-index MMFs, instead, by proper design can have stably propagating HOMs with large effective mode areas and desired dispersions (Ramachandran et al., 2008), so this type of fiber should be the waveguide where the strong soliton pulse is generated, and it is the focus of this thesis.

1.4 Thesis content and organization

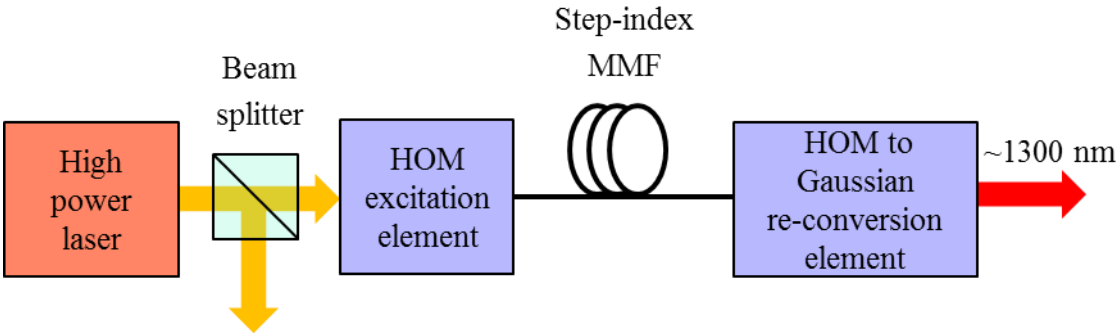

Figure 1.3: Schematic configuration of the compact source for NM.

This thesis focuses on the study of HOMs ultrafast nonlinear optics, aiming to build up a compact and robust strong pulse source that is useful to do NM by exploiting SSFS (and SSMC). The wavelength of the soliton should cover ~1300 nm so that the optimal excitation wavelength window can be utilized. The schematic configuration of this source is shown in Fig. 1.3. A high power ultrafast laser is used as the pump light to excite SSFS (and SSMC) process in the step-index MMF. A mode conversion module is needed to purely launch a specific mode in the MMF. The output ~1300 nm HOM needs to be re-

converted to a Gaussian beam by a mode re-conversion module.

The thesis is organized as follows:

Chapter 2 outlines the theoretical framework of optical fiber modes. The mathematical form of electric fields of fiber modes is given for a specific type of fiber, i.e. step-index MMF, followed by the discussion on basic properties of fiber modes, including stable propagation criterion, dispersion, effective mode area, dispersion-area (DA) product and so on.

Chapter 3 describes the theoretical framework of SSFS and SSMC. The generalized nonlinear Schrodinger equation (GNLSE) is given, based on which the pulse propagation is simulated to show the soliton power scaling through DA product scaling at the pump wavelength for both SSFS and SSMC.

Chapter 4 first presents different HOM excitation methods, including both free-space techniques, e.g. binary phase plates (BPPs) and axicons, and in-fiber techniques, e.g. long period fiber gratings (LPFGs). The characterizations of fiber mode properties, such as dispersion, are then described.

Chapter 5 shows the experimental demonstration of repeatedly alternative occurrence of SSFS and SSMC in a step-index MMF, which achieves the efficient and wideband wavelength conversion. The competition between SSFS and SSMC is also briefly discussed in this chapter.

Chapter 6 presents a compact dual color femtosecond fiber source used for CARS/SRS. The optimizations of HOM excitation and HOM-to-Gaussian conversion with axicons are described. The performance of the source, including pulse energy, peak power, beam size,

wavelength stability, and so on, is characterized.

Chapter 7 presents the soliton power scaling and wavelength extension. The power scaling strategies and their respective limitations are described first, based on which the limit of power scaling is predicted using GNLSE simulation. The second section discusses the wavelength extension of SSFS and SSMC to the mid infrared (MIR) wavelength range.

Chapter 8 summarizes the thesis and discusses the potential future directions for the work.

Chapter 2

Theory of Optical Fiber Modes

As mentioned in chapter 1, by proper fiber design the higher order modes (HOMs) can stably propagate over long distances (Ramachandran et al., 2006b; Bozinovic et al., 2013; Gregg et al., 2016), and also possess unique properties, such as high dispersion, and thus offer the platform where strong soliton pulses are generated around 1300 nm. In this chapter, the mathematical form of electric field of the eigenmodes in weakly guiding fibers is derived first, followed by the discussion on the conditions for the modes to stably propagate. After that, the unique properties of HOMs are presented to show their advantages over the fundamental mode.

2.1 Eigenmodes in weakly guiding step-index fibers

The derivation below does not give all the details. The readers, who are interested in the full procedure, should read A. Ghatak and K. Thyagarajan (Ghatak and Thyagarajan, 1998), or A. W. Snyder and J. D. Love (Snyder and Love, 1983).

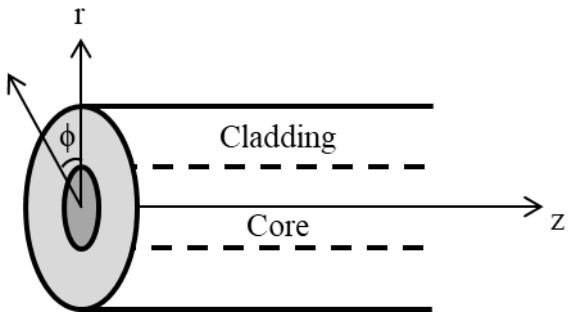

Figure 2.1: A typical optical fiber consisting of core and cladding.

Optical fibers are cylindrical waveguides, which consist of core and cladding, and generally possess azimuthally independent refractive index profile (Fig. 2.1). The refractive index profile of most fibers can be written as

$$n(r) = \begin{cases} f(r) & (r < a) \\ n_2 & (r \geq a) \end{cases} \tag{2.1}$$

where a is the core radius, and $f(r)$ represents the index profile inside the core. The maximal refractive index of the core, i.e. $f(r)$, is denoted by n_1. The refractive index of the cladding is n_2 $(n_2 < n_1)$. An optical fiber is regarded as weakly guiding if $n_1 \approx n_2$. In this type of fiber, the eigenmodes are nearly transverse and have arbitrary states of polarization, indicating they assume two orthogonal polarization directions and the propagation constants are degenerate in the polarization dimension. When the two orthogonal polarizations are chosen to be x and y, the eigenmodes are called linearly polarized (LP) modes. The transverse electric field Ψ (representing E_x or E_y) of LP modes satisfies

$$\nabla^2 \Psi = \varepsilon_0 \mu_0 n^2 \frac{\partial^2 \Psi}{\partial t^2} \tag{2.2}$$

The electric field Ψ consists of complex amplitude and phase which can be separated. In the cylindrical coordinate (r, ϕ, z), Ψ is written as

$$\Psi(r, \phi, z, t) = \psi(r, \phi) e^{i(\omega t - \beta z)} \tag{2.3}$$

where ω and β are angular frequency and propagation constant, respectively. For step-index multimode fibers (MMFs), the refractive index profile is

$$n(r)=\begin{cases} n_1 & (r<a) \\ n_2 & (r\geq a) \end{cases} \tag{2.4}$$

Replacing Ψ in Eq. (2.2) with the right-hand side of Eq. (2.3), we can derive the mathematical form of $\psi(r,\phi)$ after a lengthy derivation

$$\psi(r,\phi)=\begin{cases} \dfrac{A}{J_l(U)}J_l(\dfrac{Ur}{a})\begin{bmatrix}\cos(l\phi)\\ \sin(l\phi)\end{bmatrix} & (r<a) \\ \dfrac{A}{K_l(W)}K_l(\dfrac{Wr}{a})\begin{bmatrix}\cos(l\phi)\\ \sin(l\phi)\end{bmatrix} & (r\geq a) \end{cases} \tag{2.5}$$

where $U=a(k_0^2n_1^2-\beta^2)^{1/2}$, $W=a(\beta^2-k_0^2n_2^2)^{1/2}$, and $k_0=2\pi/\lambda_0$ is the wavenumber in vacuum (λ_0 is the wavelength in vacuum). The field $\psi(r,\phi)$ and propagation constant β can be solved using the boundary condition.

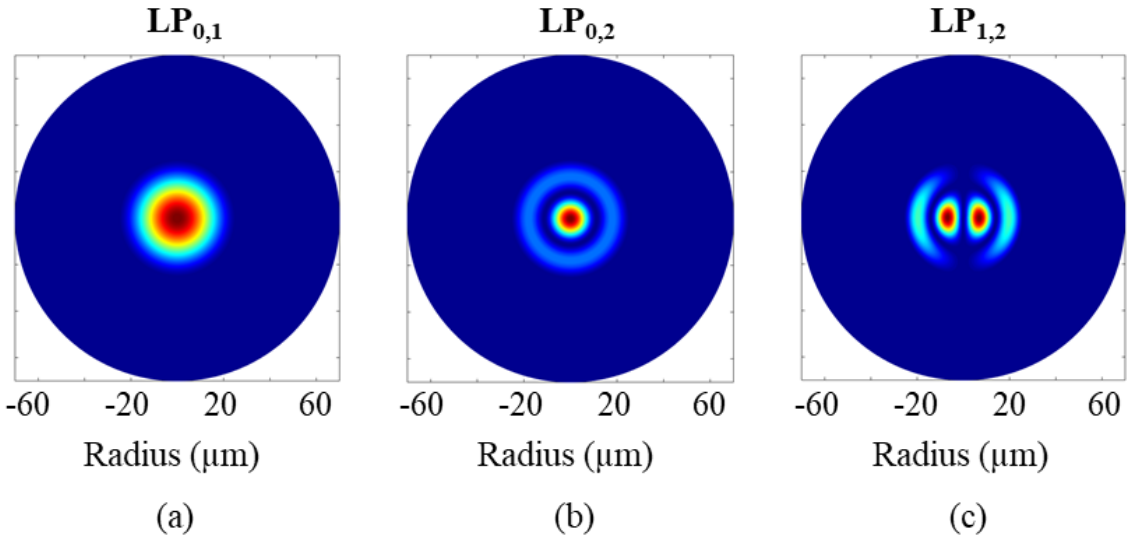

Figure 2.2: Intensity profiles of (a) $LP_{0,1}$, (b) $LP_{0,2}$ and (c) $LP_{1,2}$ at 1050 nm in a step-index MMF with a core diameter of 50 μm and NA of 0.2.

For any given l, there are a finite number of β solutions, and the eigenmode corresponding to the m^{th} one (the one having the m^{th} largest propagation constant) is called

$LP_{l,m}$ mode. In the intensity profile, the value of l represents the number of nodes along the azimuthal direction, and that of m represents the number of local maximum along the radial direction. In optical fibers, the terminology "numerical aperture (NA)" is often used. Its definition is given by

$$NA = \sqrt{n_1^2 - n_2^2} \tag{2.6}$$

The intensity distributions of $LP_{0,1}$, $LP_{0,2}$, and $LP_{1,2}$ at 1050 nm (the typical Yb fiber laser wavelength) in a step-index MMF with a core diameter of 50 μm and NA of 0.2 are shown in Fig. 2.2 to illustrate the meaning of l and m.

Some important properties of fiber modes, including effective refractive index n_{eff}, group refractive index n_g, group velocity dispersion (GVD) D (a quantity describing the change in transit time of a pulse per unit wavelength and per unit length), and effective mode area A_{eff} are calculated using the expressions below.

$$n_{eff} = \frac{\beta}{k_0} \tag{2.7}$$

$$n_g = c\frac{d\beta}{d\omega} \tag{2.8}$$

$$D = \frac{1}{c}\frac{dn_g}{d\lambda} = -\frac{\lambda}{c}\frac{d^2 n_{eff}}{d\lambda^2} = -\frac{2\pi c}{\lambda^2}\frac{d^2\beta}{d\omega^2} \tag{2.9}$$

$$A_{eff} = \frac{\left(\iint_{\infty} |\psi(r,\phi)|^2 \, r dr d\phi\right)^2}{\iint_{\infty} |\psi(r,\phi)|^4 \, r dr d\phi} \tag{2.10}$$

Note that GVD is generally simply called dispersion. Throughout this entire thesis, unless specified, the word “dispersion” means GVD.

As seen from Eq. (2.5), the electric fields of $LP_{0,m}$ modes do not have the azimuthal dependence. In other words, the fields are completely determined by Bessel functions, and thus $LP_{0,m}$ modes are called Bessel-like modes, and they are the focus of this thesis.

2.2 Stable propagation of fiber modes

2.2.1 Mode stability

One reason causing the slower and less progress in HOMs than the fundamental mode in the past decades was the intermodal coupling during propagation, i.e. part or all of the power confined in one mode at the input is transferred to the other modes at the output. This intermodal coupling can be explained using coupled-mode theory (Kashyap, 1999). Simply speaking, the coupling is induced by any perturbation changing the refractive index profile, and the coupling strength between any two modes is closely related to differential propagation constant between them, i.e. $\Delta\beta = \beta_a - \beta_b$, which is proportional to differential effective refractive index (also called neff splitting) $\Delta n_{eff} = n_{eff,a} - n_{eff,b}$. The subscripts a and b represent the two coupled modes. When Δn_{eff} increases, the coupling becomes weaker. Therefore, it is reasonable to use Δn_{eff} as the key parameter to determine whether a mode suffers from the intermodal coupling. In other words, there is expected to be a Δn_{eff} threshold, when Δn_{eff} between two modes is higher (or lower) than the threshold, the coupling occurs strongly (or very weakly so that it is thought the modes do not mix).

However, the actual coupling process is not solely determined by Δn_{eff}, the other parameters, such as perturbation strength and overlap integral between their electric fields, also matter. Therefore, there is not a universally valid Δn_{eff} threshold which works for any wavelength, any fiber, and any type of perturbation. Instead, only rough phenomenological rules have been developed based on the experimental results. In polarization-maintaining optical fibers, it has been demonstrated that $\Delta n_{eff} > 1\times10^{-4}$ allows the two $LP_{0,1}$ modes with orthogonal polarizations (x and y) to stably propagate over 100 m. This rule has also been verified in the previous work on HOMs. Thus, 1×10^{-4} is the rough Δn_{eff} threshold (Ramachandran and Kristensen, 2013). Because bending, which introduces the anti-symmetric perturbation, is the most common perturbation in fibers, the intermodal coupling mainly happens between the target mode ($LP_{0,m}$) and its nearest (in terms of n_{eff}) anti-symmetric mode ($LP_{1,m}$), and $\Delta n_{eff} = n_{eff,(0,m)} - n_{eff,(1,m)}$ needs to be compared with the threshold (Ramachandran et al., 2006b; Ramachandran et al., 2008). As one example, the neff splitting Δn_{eff} v.s. $LP_{0,m}$ mode order, i.e. m, at 1050 nm in a step-index MMF with a core diameter of 50 μm and NA of 0.28 is shown in Fig. 2.3. All the guided $LP_{0,m}$ modes in this fiber have $\Delta n_{eff} > 1\times10^{-4}$, indicating they are potentially able to stably propagate. It is clear that the neff splitting increases with mode order, meaning the chance the intermodal coupling happens to HOMs is lower than the fundamental mode.

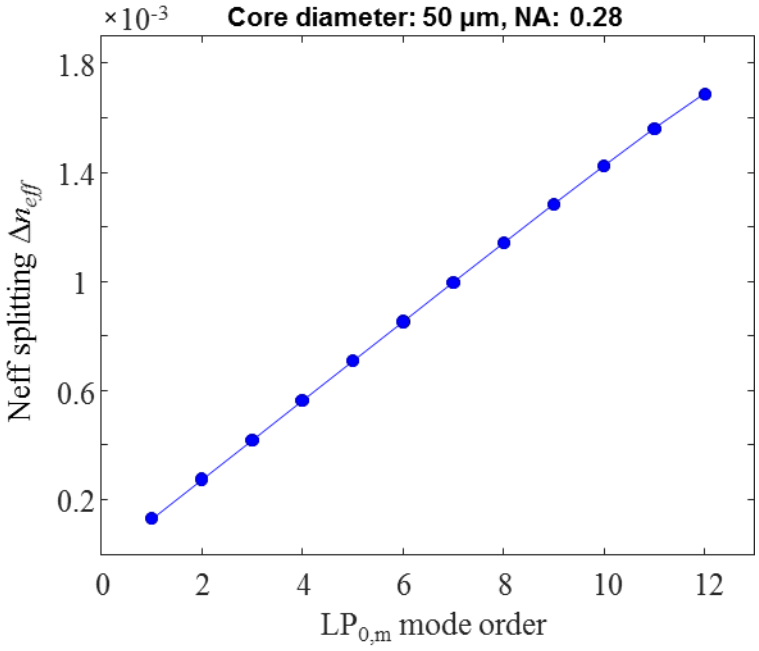

Figure 2.3: Neff splitting Δn_{eff} versus $LP_{0,m}$ mode order at 1050 nm in a step-index MMF with a core diameter of 50 μm and NA of 0.28.

It is important to understand how the fiber refractive index profile, including core diameter and NA, influences Δn_{eff}, because this knowledge provides a guidance on fiber design, and helps to predict and explain the experimental results. The Δn_{eff} vs. $LP_{0,m}$ mode order at 1050 nm for different fiber core diameters and NA's is given in Fig. 2.4. As seen from Fig. 2.4(a), when NA is fixed, for any mode order, the Δn_{eff} decreases with core diameter. In addition, although the larger core size offers more guided modes, the maximal Δn_{eff} also decreases with core diameter. Therefore, the stability of $LP_{0,m}$ modes decreases with core size. This phenomenon can be explained using the concept of density of mode distribution. For any guided mode, the effective refractive index needs to sit between the refractive index of core and cladding, i.e. $n_2 < n_{eff} < n_1$, so the more the number of guided

modes, the denser their effective indices are distributed within the range, resulting in smaller Δn_{eff} .

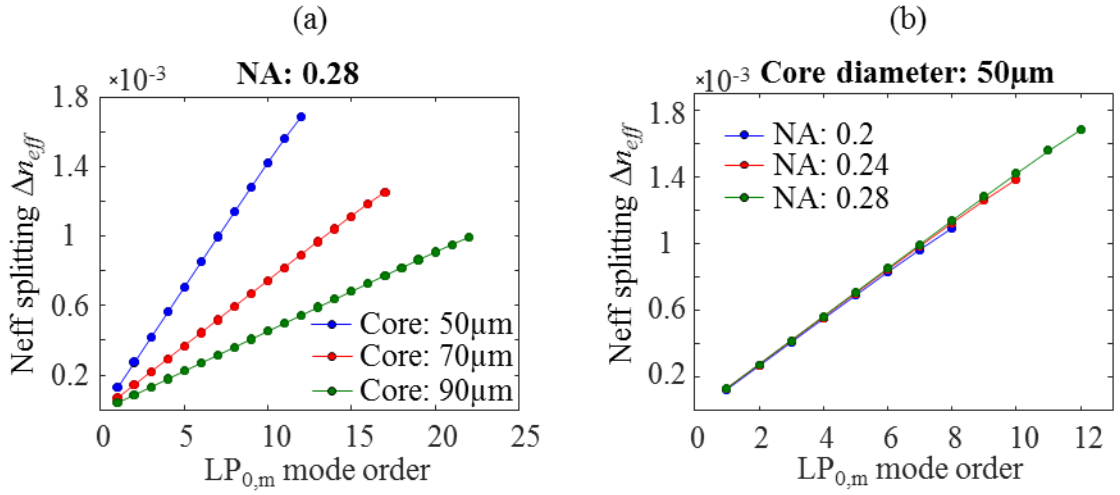

Figure 2.4: Neff splitting Δn_{eff} versus $LP_{0,m}$ mode order at 1050 nm in different step-index MMFs. (a) The NA is fixed at 0.28, and the core diameter varies between 50 μm and 90 μm. (b) The core diameter is fixed at 50 μm, and the NA varies between 0.2 and 0.28.

Figure 2.4(b) shows Δn_{eff} vs. $LP_{0,m}$ mode order for different NA's. When core size is fixed, for any mode order, Δn_{eff} barely changes with NA. The main contribution of larger NA is offering more guided modes, leading to a larger maximal Δn_{eff} . Therefore, by increasing NA the stability of $LP_{0,m}$ modes does not change, but the number of stable modes increases.

2.2.2 Mode distortion

Another factor affecting the propagation stability of fiber modes is mode distortion (Fini and Ramachandran, 2007; Ramachandran et al., 2008). The discussion on mode distortion is done by way of the comparison between step-index and graded-index (GRIN) MMFs.

Both types of MMFs have been used to implement nonlinear frequency conversion to extend the wavelength range of traditional fiber lasers (Wright et al., 2015; Rishoj et al., 2016; Rishoj et al., 2018). A natural question is which type of MMF is better. Since lots of applications based on fiber sources, such as microscopy, need to focus the beam, one criterion to make this comparison is the output beam quality. The beam quality out of a fiber is related to both mode(s) excitation at the fiber input and propagation through the fiber. Since Both types of MMFs are weakly guiding, and confine LP modes, so they should be equivalent in terms of excitation. Thus, the comparison is focused on the propagation and implemented from two aspects: mode stability and mode distortion.

As discussed in the last section, mode stability is characterized by $\Delta n_{eff} = n_{eff,(0,m)} - n_{eff,(1,m)}$. The simulated Δn_{eff} at 1050 nm in two fibers available in our lab (one step-index and one GRIN MMF) is given in Fig. 2.5 for comparison. The step-index MMF has a core diameter of 48 μm and NA of 0.34, and the GRIN MMF has a core diameter of 62.5 μm and NA of 0.28 (In GRIN MMFs, NA is still given by Eq. (2.31), and n_1 is the refractive index at the center, i.e. the maximal index inside the core). In both fibers, the Δn_{eff} is higher than the threshold (1×10^{-4}), indicating there is barely intermodal coupling. In the step-index MMF, as expected, Δn_{eff} increases with mode order; however, in the GRIN MMF, Δn_{eff} is basically constant, staying at $\sim 1\times10^{-3}$, which is a natural result of the key property in GRIN MMFs, i.e. all modes sharing the same group refractive index. Based on the Δn_{eff} result, for low mode order, the GRIN MMF is more stable, and for high mode order, the step-index MMF is more stable.

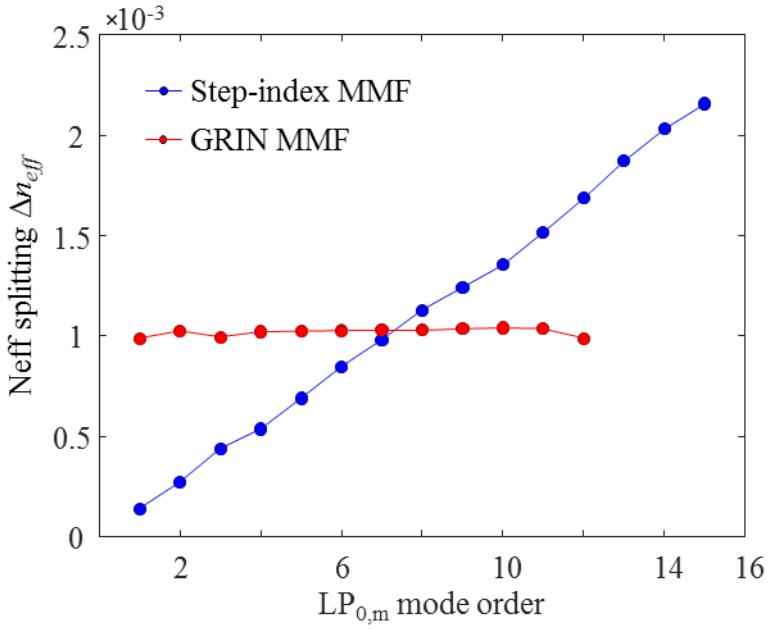

Figure 2.5: Neff splitting Δn_{eff} versus $LP_{0,m}$ mode order at 1050 nm in one step-index MMF (blue, core diameter: 48 μm, NA: 0.34), and one GRIN MMF (red, core diameter: 62.5 μm, NA: 0.28).

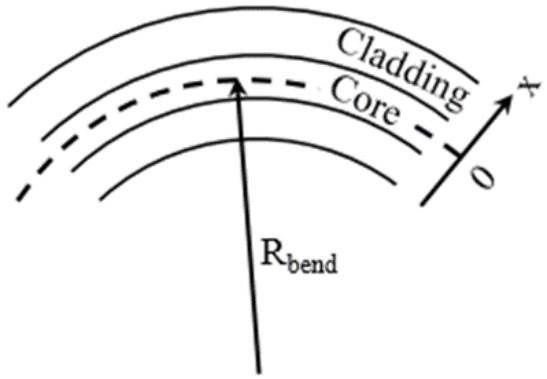

Figure 2.6: A piece of bent fiber.

Since bending (Fig. 2.6) is the most common factor influencing the refractive index profile of a fiber, and further distorting the field distribution, the comparison of mode distortion induced by fiber bending between step-index and GRIN MMFs is done in both

simulation and experiments. Figure 2.7 shows the simulation results at 1050 nm in two fibers which are basically the same as those in Fig. 2.5, except the center burn-off is removed. In the plane of bending, i.e. the plane comprising the bent fiber, the refractive index profile of the fiber can be seen as a straight fiber with a slanted index profile based on the relation (Marcuse, 1982; Tsuchida et al., 2005)

$$n_{bent} = n_{straight}(1 + x / R_{bend}) \tag{2.11}$$

It is known the effective index n_{eff} of a mode must be lower than the refractive index of the waveguide in order to be confined. In both step-index and GRIN MMFs (Fig. 2.7(a) and (b)), the slanted refractive index profile of the core can intersect $n_{eff}{}'s$ of a mode. As a result, part of core region, which has a higher refractive index than the n_{eff} in a straight fiber, becomes lower due to the bending. This region is called the forbidden region. Its appearance means the electric field of the mode is distorted by the bending and pushed into the high-index side.

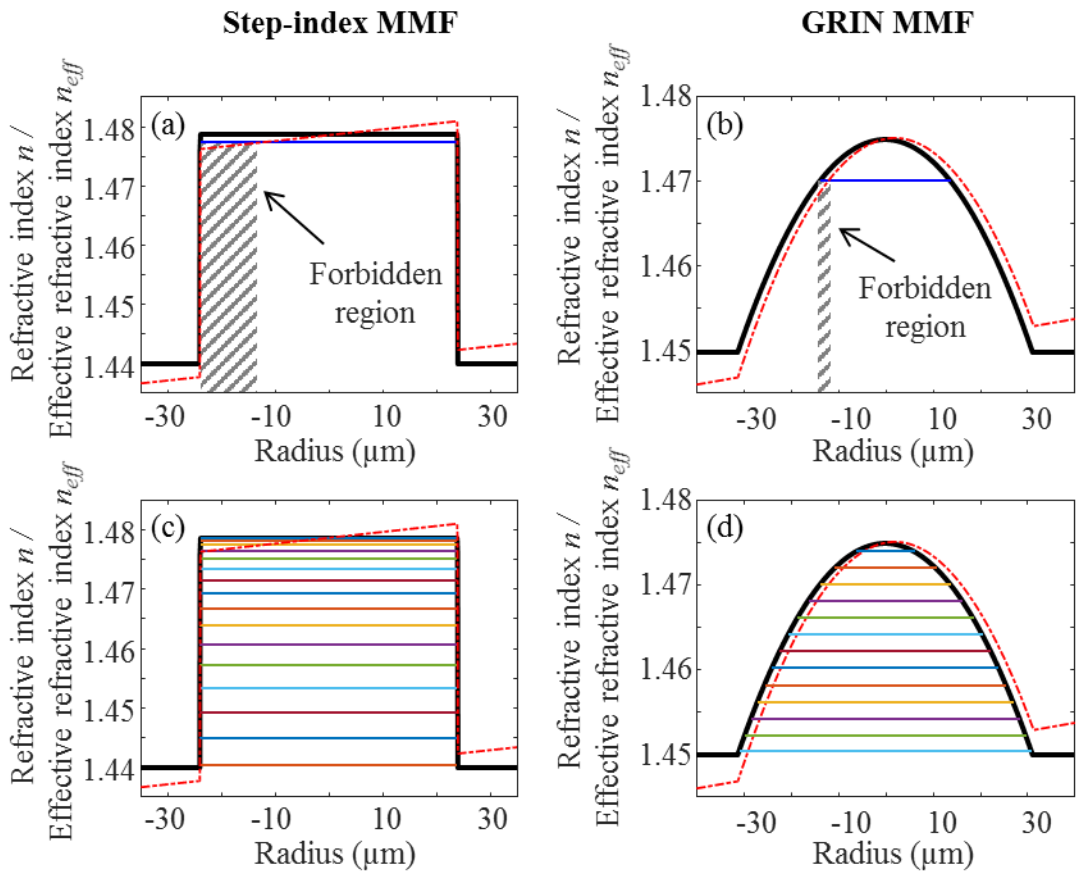

Figure 2.7: Illustration of forbidden region in a bent fiber for both (a) step-index MMF and (b) GRIN MMF. (c) The HOMs in step-index MMFs can be distortion-free in bent fibers. (d) All modes in GRIN MMFs are distorted by fiber bending. Step-index MMF: core diameter: 48 μm, NA: 0.34. GRIN MMF: core diameter: 62.5 μm, NA: 0.28.

As seen in Fig. 2.7 (c), in step-index MMFs, $n_{eff}{}'s$ of the modes of low order are intersected by the slanted core refractive index, and their fields are distorted. However, $n_{eff}{}'s$ of the modes of high order are lower than the slanted refractive index across the entire core, and thus their fields are immune to the bending. In contrast, in GRIN MMFs (Fig. 2.7(d)), $n_{eff}{}'s$ of all the modes are intersected by the slanted core index profile, indicating they are all distorted by the bending. It should be noted that strong field

distortion means the eigenmode(s) is(are) modified, and is generally accompanies by the intermodal coupling, so the output image can be a mixture of multiple modes.

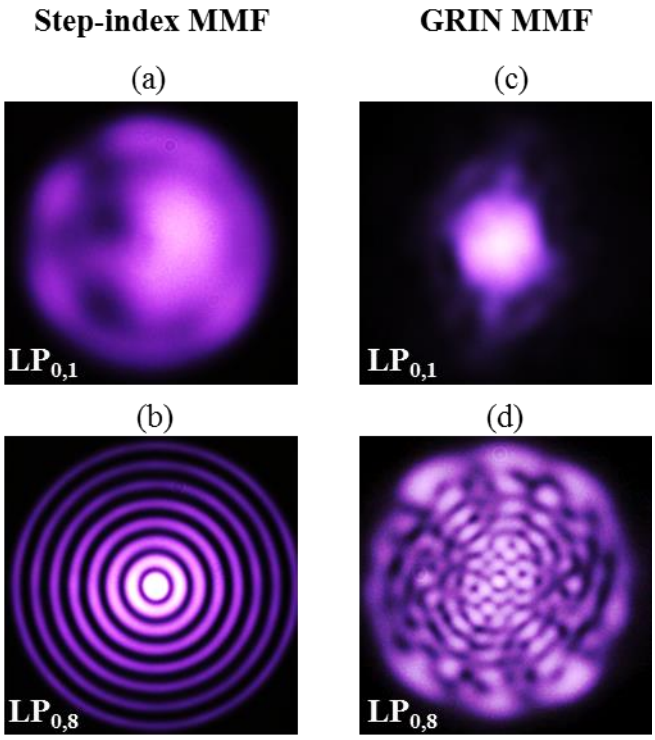

Figure 2.8: Output images from MMFs while a specific mode is excited at the input at 1050 nm. (a) step-index MMF, $LP_{0,1}$ excitation. (b) step-index MMF, $LP_{0,8}$ excitation. (c) GRIN MMF, $LP_{0,1}$ excitation. (d) GRIN MMF, $LP_{0,8}$ excitation. Step-index MMF: core diameter: 48 μm, NA: 0.34. GRIN MMF: core diameter: 62.5 μm, NA: 0.28. (Data courtesy of Dr. Lars Rishøj)

The experiments are done to verify the field distortion theory. The output mode images of one-meter-long bent fibers (the same fibers as those in Fig. 2.5) are recorded while exciting a specific mode at 1050 nm (The mode excitation is discussed in chapter 4). The results are given in Fig. 2.8. Clearly, in the step-index MMF while $LP_{0,1}$ is strongly distorted, $LP_{0,8}$ stably propagates through the fiber. However, in the GRIN MMF, both $LP_{0,1}$ and $LP_{0,8}$ are distorted.

In addition, as will be in Sec. 2.3.1, step-index MMFs have the flexibility in dispersion engineering. However, in GRIN MMFs because of the nature of all modes having the same group refractive index, the dispersions of different modes are quite similar, and close to the material dispersion of pure silica (SiO_2).

Through the comparison it is clear that in terms of output beam shape/quality and dispersion engineering flexibility, step-index MMFs are better than GRIN MMFs.

2.3 Important HOM properties

2.3.1 Dispersion

Dispersion is a very important fiber property because of its influence in lots of areas, such as optical communication and nonlinear fiber optics. In communication systems, dispersion compensation fibers (DCFs), which have strong normal dispersion at 1550 nm, were used a lot in the past to cancel the pulse broadening (Ramachandran, 2005) induced by SMF-28—the widely used single mode fiber (SMF) in communication. In nonlinear fiber optics, because dispersion changes the pulse duration and peak power, it affects nonlinear effects. Along with the pulse duration modification, dispersion also adds chirp in the pulse, which, properly combined with self-phase modulation (SPM) (Ippen et al., 1974), facilitates spectral compression (Planas et al., 1993) and soliton formation (Mitschke and Mollenauer, 1986). Since chirp puts different frequency components into different time bins, dispersion can also be used to build a time-domain spectrometer, which was demonstrated in single photon spectrum measurement (Avenhaus et al., 2009).

Under the weakly guiding approximation, the total dispersion of a mode D can be decomposed into two parts: material dispersion D_m and waveguide dispersion D_w.

$$D = D_m + D_w \tag{2.12}$$

Since the main material in most fibers is silica (SiO_2), the material dispersion D_m is fixed. Dispersion engineering boils down to tuning the waveguide dispersion D_w. Both high normal and high anomalous waveguide dispersion have been demonstrated. In this thesis we focus on the discussion on anomalous dispersion, since it is related to the soliton formation. Before starting the deeper discussion, it needs to be mentioned, normal dispersion corresponds to $D < 0$, and anomalous dispersion corresponds to $D > 0$.

The high normal waveguide dispersion is introduced by exploiting the fast transition of mode field from high refractive index to low refractive index region (Ramachandran, 2005). This transition produces quick decrease of group refractive index n_g (or quick increase of group velocity $v_g = c/n_g$) with wavelength, and thus high normal waveguide dispersion. The typical refractive index profile is a three-layer structure, i.e. high-index core, low-index trench, and a high-index outer ring. The example of one DCF is shown Fig. 2.9. The refractive index profile relative to silica cladding, and the fast transition of $LP_{0,2}$ field from core to outer ring around 1550 nm are shown in Fig. 2.9(a). The total dispersion D is numerically simulated and plot in Fig. 2.9(b). To show the influence of the strong waveguide dispersion, the material dispersion D_m is also given.

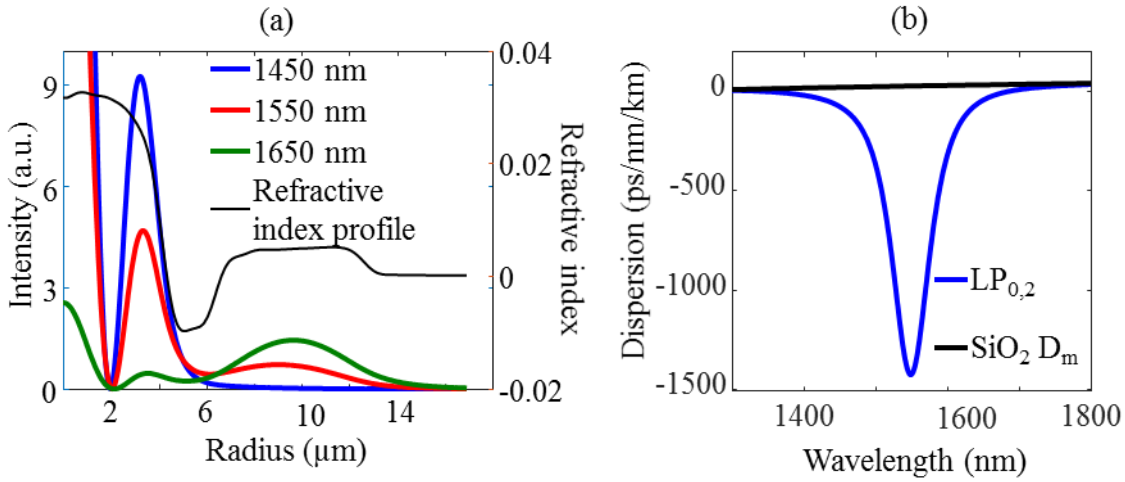

Figure 2.9: (a) The $LP_{0,2}$ field transition from the core to the outer ring around 1550 nm (left y axis), and the refractive index profile (right y axis) of a DCF. (b) The dispersion of $LP_{0,2}$ of the DCF and material dispersion of pure silica.

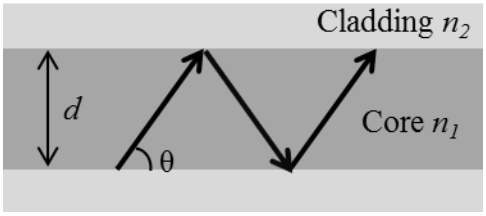

Figure 2.10: The dielectric planar waveguide for anomalous waveguide dispersion illustration.

The high anomalous waveguide dispersion is induced by a different way—strong confinement (Ramachandran et al., 2006a; Ramachandran et al., 2008). The underlying mechanism can be illustrated using a simplified waveguide structure—dielectric planar waveguide with core and cladding indices of n_1 and n_2, and a core diameter of d (Fig. 2.10). Since we focus on the engineering of waveguide dispersion, the material dispersion is neglected, i.e. n_1 and n_2 are both constants.

An eigenmode has a given transverse electric field solution, this means the phase in the

transverse plane experiences a phase shift of an integer times of 2π after a round trip, and this can be written as

$$2k_t d + 2\phi_{GH} = 2m\pi \tag{2.13}$$

where k_t the transverse wavenumber ($k_t = n_1 k_0 \sin\theta$), ϕ_{GH} is Goos-Hänchen phase shift which is induced when the light bounces at the core-cladding interface, the integer m represents the mode order. Goos-Hänchen phase shift ϕ_{GH} is expressed as

$$\phi_{GH} = 2\tan^{-1}\left[\frac{\sqrt{n_1^2\cos^2\theta - n_2^2}}{n_1\sin\theta}\right] \tag{2.14}$$

When a mode is strongly confined, the angle θ is very small, resulting in $\phi_{GH} \sim 2\pi$. So Eq. (2.13) can be rewritten as

$$k_t d = (m-2)\pi \tag{2.15}$$

The angle θ can be derived.

$$\theta = \sin^{-1}\left[\frac{(m-2)\lambda_0}{2n_1 d}\right] \tag{2.16}$$

It is clear that for a given mode order (a fixed value of m), when wavelength increases, the angle θ also increases. Under the strong confinement condition, the transit time taken by a mode to propagate a unit length can be calculated according to ray optics.

$$\tau = \frac{n_1}{c\cdot\cos\theta} \tag{2.17}$$

The waveguide dispersion D_w then can be calculated by

$$D_w = \frac{d\tau}{d\lambda} = \frac{n_1}{c}\frac{d}{d\lambda_0}\left(\frac{1}{\cos\theta}\right) \tag{2.18}$$

After a lengthy derivation, the expression for D_w can be written as

$$D_w = \frac{2\pi n_1^2 k_t^2}{c\lambda_0^2 (n_1^2 k_0^2 - k_t^2)^{3/2}} \tag{2.19}$$

The derivation can also start with Eq. (2.9).

$$\beta = \sqrt{n_1^2 k_0^2 - k_t^2} \tag{2.20}$$

Using Eq. (2.9) $D_w = -\frac{2\pi c}{\lambda^2}\frac{d^2\beta}{d\omega^2}$, the expression for D_w can also be derived, and the result is the same as Eq. (2.19).

For any guided mode, both k_t and β are real numbers, i.e. $0 < k_t < n_1 k_0$, so all the factors in Eq. (2.19) are positive, and D_w is positive, meaning anomalous waveguide dispersion. Therefore, the strong confinement of a mode produces anomalous waveguide dispersion. The influence of mode order m and core diameter d on waveguide dispersion is included in transverse wavenumber k_t. Equation (2.15) tells us k_t increases with m. Therefore, when mode order m increases, the numerator of Eq. (2.19) increases, but denominator decreases, resulting in the increase of the waveguide dispersion. Similarly, it can be deduced that larger core leads to smaller waveguide dispersion. These two points should be understood from the angle of strong confinement. Strong confinement means the mode field "feels" the high index difference at the core-cladding interface when "touching" it. The physical intuition is that the "feeling" of the confinement becomes stronger when the field expands outwards and has more intensity distributed around the interface. From Eq. (2.16) it can be seen that when the mode order increases, the angle θ increases, which, based on ray optics, means the guided light is closer to the critical situation (where the

refraction angle is 90°), and is expected to penetrate more outside the core, i.e. the evanescent wave becomes stronger, so the field "feels" the confinement more strongly, and the waveguide dispersion increases correspondingly. When the core size becomes larger, for any mode the intensity distribution around core-cladding interface becomes less, so the "feeling" of the confinement is weaker, and the waveguide dispersion decreases correspondingly.

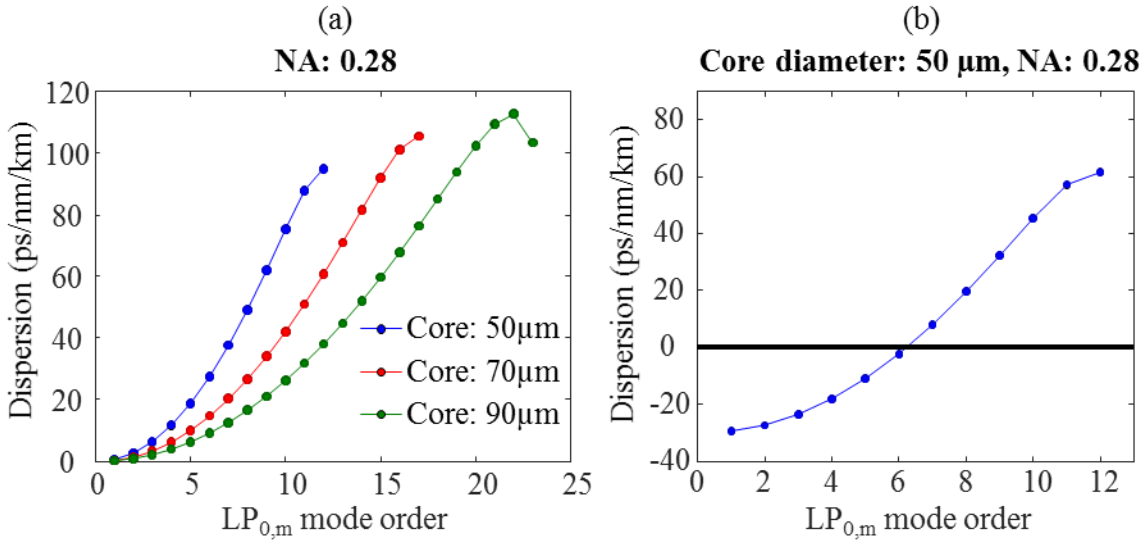

Figure 2.11: (a) The waveguide dispersion D_w versus mode order at 1050 nm in step-index MMFs with NA of 0.28 and different core diameters (from 50 μm to 90 μm). (b) The total dispersion D versus mode order at 1050 nm in a step-index MMF with a core diameter of 50 μm and NA of 0.28.

Figure 2.11(a) plots the waveguide dispersion versus $LP_{0,m}$ mode order at 1050 nm in step-index MMFs with NA of 0.28 and different core sizes (from 50 μm to 90 μm). As expected from the analysis above, the strong confinement from the high NA gives anomalous waveguide dispersion, which increases with mode order, but decreases with core size. The total dispersion D versus $LP_{0,m}$ mode order at 1050 nm is shown in Fig.

2.11(b) in a step-index MMF with a core diameter of 50 μm and NA of 0.28. Clearly, due to the strong anomalous waveguide dispersion, the normal material dispersion can be compensated, and the total dispersion starts being anomalous from $LP_{0,7}$.

The coupling between waveguide dispersion and effective mode area mentioned in chapter 1 can be explained better now. Figure 2.11(a) shows how small the waveguide dispersion is for the fundamental mode ($LP_{0,1}$). In order to force $LP_{0,1}$ to have large waveguide dispersion, the core needs to very small so that the core-cladding interface is "felt" by the mode very strongly. This is the underlying mechanism of dispersion engineering in photonic crystal fibers (PCFs). To make the anomalous dispersion available for wavelength ≤ 1300 nm, the core size of a PCF is generally smaller than 4 μm, which, combined with the large refractive index step between silica core and air-silica cladding, makes the confinement on fundamental mode very strong, so the anomalous dispersion can be even pushed into the visible wavelength range. However, as mentioned in chapter 1, the small core size (and thus the small effective mode area) sacrifices the high power property. For any HOM, the coupling between the waveguide dispersion and effective mode area still exists. However, the existence of a set of stable HOMs offers a new degree of freedom for nonlinear optics, using which the strong anomalous waveguide dispersion and large effective mode area can be achieved simultaneously.

2.3.2 Effective mode area

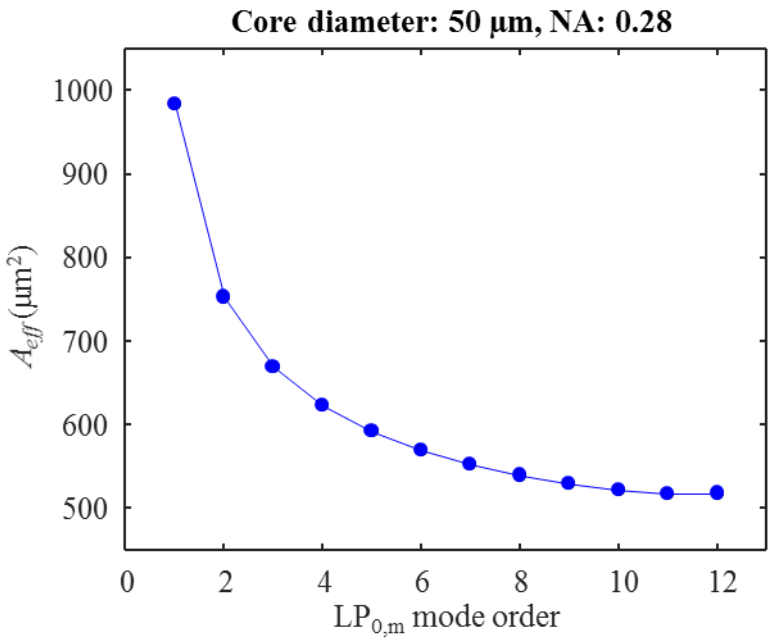

Figure 2.12: Effective mode area A_{eff} versus mode order at 1050 nm in a step-index MMF with a core diameter of 50 µm and NA of 0.28.

Effective mode area (A_{eff}) is another important fiber property due to its influence on the efficiency of nonlinear process and soliton energy. The effective mode area versus $LP_{0,m}$ mode order at 1050 nm in a step-index MMF with a core diameter of 50 µm and NA of 0.28 is given in Fig. 2.12. The effective mode area A_{eff} decrease with mode order, this is because the expansion of the mode field of a higher order is prohibited by the strong confinement at the core-cladding interface, meantime the higher mode order means there are more nodes in the intensity profile, so the effective area taken by the mode (effective mode area) becomes less. Clearly, the effective mode areas of HOMs are more than one order of magnitude higher than that of the fundamental mode in PCFs.

2.3.3 Dispersion-area product

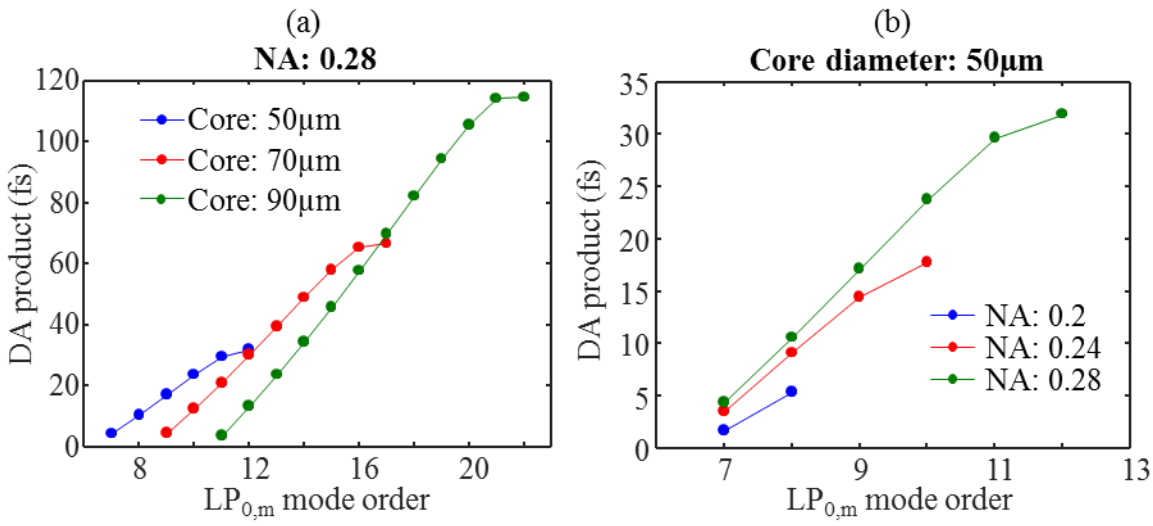

Figure 2.13: The DA product versus mode order at 1050 nm in different step-index MMFs. (a) Fixed NA: 0.28, and different core diameters (from 50 μm to 90 μm). (b) Fixed core diameter: 50 μm, and different NAs (from 0.2 to 0.28).

The soliton energy is proportional to the product of dispersion and effective mode area (called DA product hereafter) (van Howe et al., 2007; Lee et al., 2008), and soliton energy at a certain wavelength can be calculated using that at the pump wavelength, assuming the loss only comes from photon-phonon interaction. Therefore, the calculation of DA product at the pump wavelength is useful to predict the performance of soliton self-frequency shift (SSFS) in a fiber. Figure 2.13 shows the DA product versus mode order at 1050 nm for anomalously dispersive modes in step-index MMFs, and the influence of core size (Fig. 2.11(a)) and NA (Fig. 2.11(b)) on the product. Two conclusions can be obtained from the two sub-figures. 1) DA product increases with mode order, indicating a mode of higher order can generate more energetic solitons. 2) For a given mode order, the increase of core size or NA does not improve much on (or even degrades) the DA product, but it provides

more guided modes which improve the maximal DA product a fiber has. Therefore, larger core or higher NA step-index MMFs can potentially generate more powerful solitons.

2.4 Summary

This chapter has described the theoretical frame on eigenmodes in weakly guiding fibers, focusing on the important aspects about high power fiber sources. The main conclusions are listed below.

1. The comparison among different mode orders in terms of Δn_{eff} shows that the mode stability increases with mode order.

2. The comparison of DA product among different mode orders shows that the soliton energy at a certain wavelength potentially increases with mode order. A more rigorous comparison will be done in chapter 3 using the generalized nonlinear Schrödinger equation (GNLSE).

3. The influence of fiber refractive index profile on the mode properties points out larger core size and higher NA are helpful for power scaling, but might with the sacrifice of mode stability.

4. Step-index MMFs are more resistant to fiber bending than GRIN MMFs.

5. Step-index MMFs have the dispersion engineering flexibility, but GRIN MMFs do not.

These conclusions indicate the HOMs in step-index MMFs are proper tools for developing high power fiber sources, including traditional rare earth doped fiber lasers, and frequency conversion systems based on nonlinear optical effects, such as SSFS.

Chapter 3

Theory of Soliton Based Frequency Conversion

Soliton self-frequency shift (SSFS) (Mitschke and Mollenauer, 1986), and the recently discovered intermodal interpulse Raman scattering process, i.e soliton self-mode conversion (SSMC) (Rishoj et al., 2018), are the main mechanisms exploited in this thesis for building up the strong pulse source around 1300 nm. In this chapter, the theory is first introduced for both SSFS and SSMC, and then the soliton power scaling by way of dispersion-area (DA) product scaling at the pump wavelength is shown in both theoretical simulation and experimental measurements.

3.1 Soliton self-frequency shift

3.1.1 Theory of soliton

A soliton (Mollenauer et al., 1980) is an optical pulse of which both the temporal and spectral shapes does not change during propagation. Its formation originates from the balance between group velocity dispersion (GVD) and self-phase modulation (SPM) (Ippen et al., 1974) effects. This balance can be understood from the angle of chirp (Ghatak and Thyagarajan, 1998). With the influence of SPM, the modified refractive index n can be written as

$$n = n + n_2 \left| E(t) \right|^2 \tag{3.1}$$

where n is the original linear refractive index, n_2 is the nonlinear-index coefficient, and $E(t)$ is the electric field. The resultant propagation constant at the carrier frequency ω_0 can be written as

$$\beta = \beta_0 + n_2 |E(t)|^2 k_0 \tag{3.2}$$

where β_0 and k_0 are propagation constant and wavenumber in vacuum at the carrier frequency. Assuming there is no GVD or higher order dispersion effect, the phase is then

$$\varphi = \beta_0 z + n_2 |E(t)|^2 k_0 z - \omega_0 t \tag{3.3}$$

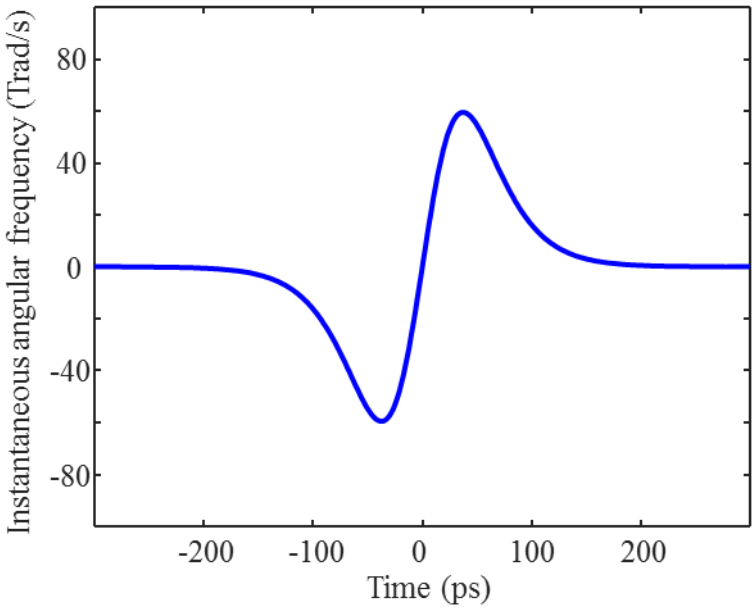

Figure 3.1: The SPM induced chirp on a sech^2 pulse (functional form defined in Eq. (3.5)) with P_0 =14.6 kW, and T_0 =56.7 fs.

It can be derived the deviation of instantaneous angular frequency from the carrier frequency is

$$\Delta\omega(t) = -n_2 k_0 z \frac{\partial |E(t)|^2}{\partial t} \propto -n_2 k_0 z \frac{\partial P(t)}{\partial t} \tag{3.4}$$

It is clear from Eq. (3.4) that the instantaneous frequency deviation, spectral broadening, and chirp are dependent on the pulse shape. The chirp on a sech^2 pulse (defined below in Eq. (3.5)) is shown in Fig. 3.1. At the central portion the chirp is positive, i.e. the frequency increases with time. In order to balance the SPM induced chirp and keep the bandwidth unchanged, GVD must apply a negative chirp ($\beta_2 < 0$, or $D > 0$) to the pulse meantime. This is where the need of anomalous GVD for soliton formation is from.

The balance between GVD and SPM can also be expressed using two characteristic length scales, dispersion length L_D and nonlinear length L_{NL} (Agrawal, 2007). They are the lengths over which the GVD and nonlinear effects start becoming important for the pulse evolution. The pulses from lots of lasers approximately assume Gaussian or squared hyperbolic secant (simply called sech^2) shape. The functional forms of their electric fields are

$$A(z=0,T) = \begin{cases} \sqrt{P_0}\, e^{-\frac{T^2}{2T_0^2}} & (Gaussian) \\ \sqrt{P_0}\,\mathrm{sech}(\frac{T}{T_0}) & (\mathrm{sech}^2) \end{cases} \tag{3.5}$$

where T_0 is the characteristic pulse duration relating to T_{FWHM} (full width at half maximum) by $T_{FWHM} = 2\sqrt{\ln 2}T_0 \approx 1.665T_0$ for the Gaussian pulse, and $T_{FWHM} \approx 1.763T_0$ for the sech^2 pulse; P_0 is the peak instantaneous power. The definitions of the characteristic length scales are

$$L_D = \frac{T_0^2}{|\beta_2|} \tag{3.6}$$

$$L_{NL} = \frac{1}{\gamma P_0} \tag{3.7}$$

where γ is the nonlinear coefficient, defined as

$$\gamma(\omega) = \frac{n_2(\omega)\cdot\omega}{A_{eff}(\omega)\cdot c} \tag{3.8}$$

The balance between the linear (GVD) and nonlinear (SPM) effects indicates the two length scales should be equal to each other ($L_D = L_{NL}$).

The analytical expression for a soliton is written as

$$A(z,T) = \sqrt{P_0}\,\mathrm{sech}(\frac{T}{T_0})e^{i\frac{|\beta_2|z}{2T_0^2}} \tag{3.9}$$

Clearly, the soliton is a transform-limited (seen from the time-independent phase) sech^2 pulse, with a constant shape in both time and frequency domains. Its pulse energy E_{sol} is calculated to be

$$E_{sol} = 2P_0T_0 \tag{3.10}$$

which, combined with Eqs. (2.9)-(2.10), (3.6)-(3.8), and the relation $L_D = L_{NL}$, gives us

$$E_{sol} = \frac{2cA_{eff}|\beta_2|}{\omega_0 n_2 T_0} \propto \frac{A_{eff}|\beta_2|}{T_0} \propto |\beta_2| A_{eff}\Delta\lambda \propto DA_{eff}\Delta\lambda \tag{3.11}$$

where $\Delta\lambda$ is the soliton bandwidth. The reciprocal relation between the characteristic pulse duration T_o and bandwidth $\Delta\lambda$ ($\Delta\lambda \propto 1/T_0$) is used in the derivation above.

3.1.2 Theory of soliton self-frequency shift

A soliton is perturbed by Raman scattering effect (Stolen and Ippen, 1973), the shorter wavelength (higher frequency) part transfers energy to longer wavelength (lower frequency) part, and the entire soliton keeps shifting itself to longer wavelength. This process is the so-called SSFS (Mitschke and Mollenauer, 1986), which is an intrapulse Raman scattering process. The corresponding soliton is called Raman soliton. The Raman soliton is perturbed by higher order dispersion effects, which force it to continuously adjust peak power and pulse duration to the local GVD during the frequency shift, in order to keep the relation $L_D = L_{NL}$ valid. The higher order dispersion effects also facilitate the energy transfer from Raman solitons to dispersive waves sitting in the normal GVD wavelength range. The emission of dispersive wave is called Cherenkov radiation process (Skryabin et al., 2003).

The soliton under the condition $L_D = L_{NL}$ is fundamental soliton. For most of the time, at the fiber input end, $L_D > L_{NL}$. Under this condition higher order solitons can be formed (Dudley et al., 2006; Agrawal, 2007). However, they are not able to stably propagate inside fibers due to the perturbations from higher order dispersion and Raman effects, and eventually split into a series of fundamental solitons in the order such that the one having the largest peak power is produced first, and the one having the smallest peak power is produced at last. Generally, the first produced constituent fundamental soliton is used in the experiment, its peak power and characteristic pulse duration can be expressed as (Dudley et al., 2006)

$$P_1 = P_0 \frac{(2N-1)^2}{N^2} \tag{3.12}$$

$$T_1 = \frac{T_0}{2N-1} \tag{3.13}$$

where P_0, T_0 are peak instantaneous power and characteristic pulse duration of the higher order soliton, respectively. The quantity N is the soliton order, defined as

$$N^2 = \frac{L_D}{L_{NL}} \tag{3.14}$$

Each of these constituent fundamental solitons then experiences SSFS and energy transfer to Cherenkov radiation. The readers who are interested in higher order solitons can read the relevant reference materials (Dudley et al., 2006; Agrawal, 2007). Throughout this thesis, the fundamental soliton is the focus, and unless specified otherwise, the word "soliton" represents the fundamental soliton.

The formation of Raman soliton and Cherenkov radiation can be simulated using the frequency domain generalized nonlinear Schrödinger equation (GNLSE) (Dudley and Taylor, 2010)

$$\frac{\partial A'}{\partial z} = i\frac{\gamma(\omega_0)\omega}{\omega_0} e^{-Lz} \mathcal{F}\left\{ A(z,T) \int_{-\infty}^{\infty} R(T') \left| A(z, T-T') \right|^2 dT' \right\} \tag{3.15}$$

where $A'(z,T)$ is defined as

$$A'(z,\omega) = A(z,\omega) e^{-L(\omega)z} \tag{3.16}$$

$$A(z,\omega) = \mathcal{F}[A(z,T)] \tag{3.17}$$

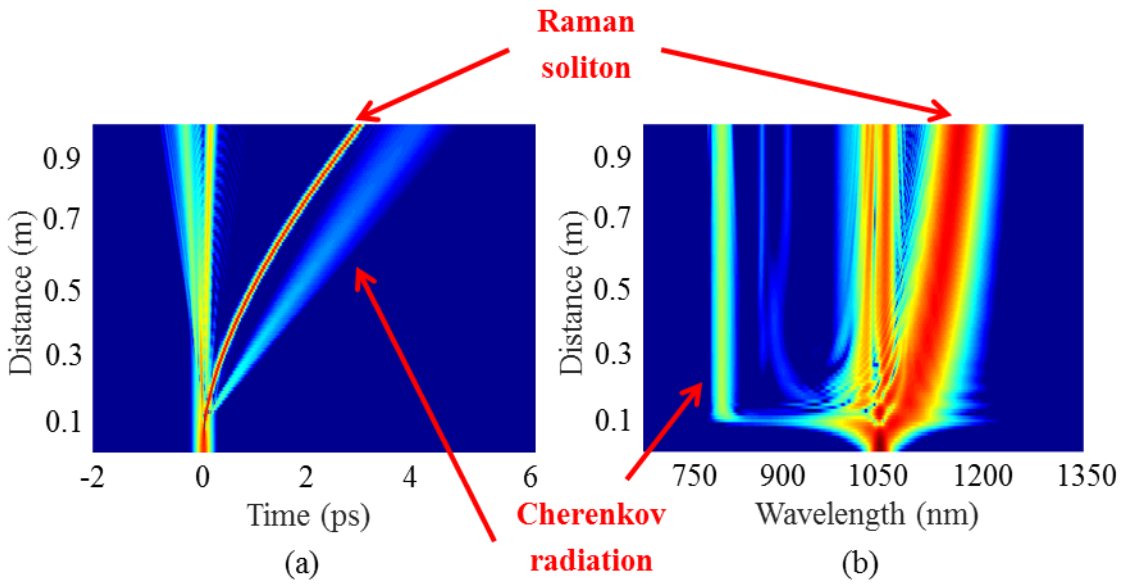

Figure 3.2: The simulated evolution in (a) time and (b) frequency domains of an input sech^2 pulse with P_0 =131.2 kW, and T_0 =56.7 fs. Fiber parameters: core diameter: 48 μm, NA: 0.34, length: 1 m. The strong Raman soliton and the Cherenkov radiation associated to it are labeled.

where $A(z,T)$ is the slowly varying pulse envelope. The linear operator $L(\omega)$ is defined as

$$L(\omega) = i[\beta(\omega) - \beta(\omega_0) - \beta_1(\omega_0)(\omega - \omega_0)] - \frac{\alpha}{2} \tag{3.18}$$

where $\beta_1 = \left.\frac{\partial \beta}{\partial \omega}\right|_{\omega=\omega_0}$, and α is the absorption coefficient. A pulse propagation simulation is implemented on the $LP_{0,9}$ mode in a step-index MMF with a core diameter of 48 μm and numerical aperture (NA) of 0.34, and the results are given in Fig. 3.2. The SSFS and Cherenkov radiation can be clearly seen. Note that since the input pump pulse is not an ideal fundamental soliton, only part of power transforms to the strong Raman soliton labelled in the figure.

3.1.3 Effect of dispersion-area product on soliton energy

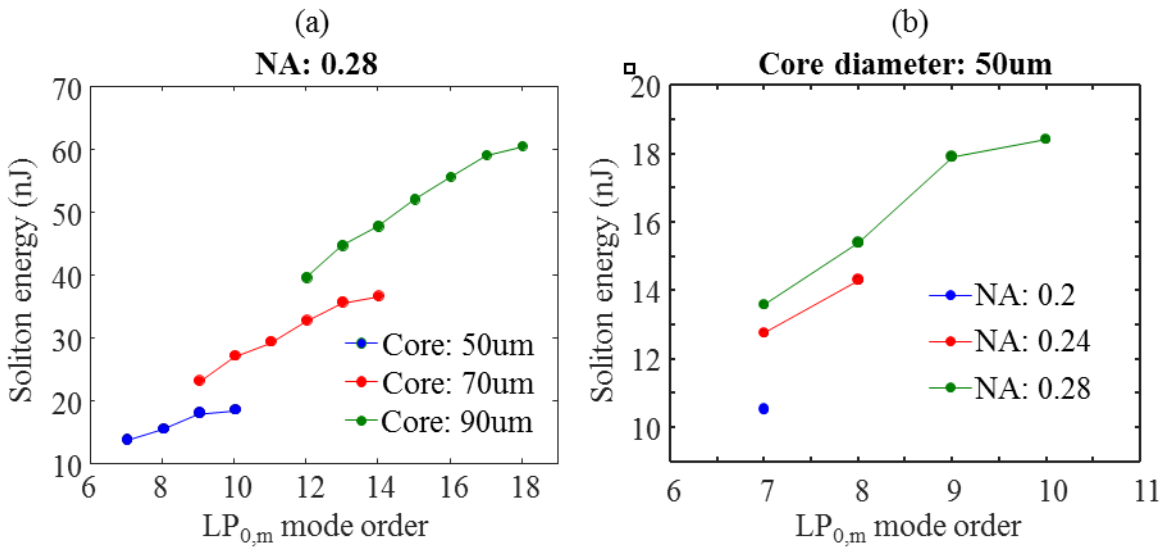

Figure 3.3: The soliton energy versus mode order around 1300 nm (1295-1305 nm) in different step-index MMFs. (a) Fixed NA: 0.28, and different core diameters (from 50 μm to 90 μm). (b) Fixed core diameter: 50 μm, and different NAs (from 0.2 to 0.28). The input pulse assumes a Gaussian shape with center wavelength of 1050nm and duration of T_0 =60.1 fs. The fiber length is 1 m.

The influence of dispersion-area product (DA product) on soliton energy was analyzed in Sec. 2.3.3. Based on the product at the pump wavelength on different mode orders in different fibers, it was pointed out at a given wavelength the soliton energy a fiber is able to offer increases with core size, NA and mode order. The simulation based on Eq. (3.12) is implemented in the step-index multimode fibers (MMFs) used in Fig. 2.13. In the simulation, a Gaussian pulse, with center wavelength of 1050nm and duration of T_0 =60.1 fs, is launched into a 1 m length of fiber, and the pulse energy is calculated on the solitons around 1300 nm (1295-1305 nm), i.e. the optimal wavelength window for deep tissue imaging. The results are shown in Fig. 3.3, and it clearly supports the previous conclusion.

Therefore, soliton energy can be scaled by scaling DA product at the pump wavelength.

The soliton energy scaling has also been observed in experiments, where the step-index MMF has a core diameter of 48 μm, NA of 0.34, and a length of 37 cm. Figure 3.4(a) shows the simulated DA product at 1050 nm (The pump wavelength is 1045 nm in the experiments). As before, the DA product increases with mode order. Figure 3.4(b) shows the simulated and experimentally measured soliton energies at ~1300 nm on different $LP_{0,m}$ modes. In the simulation, the input pump pulse is created based on the measured pump spectrum and pulse duration (the details will be given in Sec. 7.1.3). The simulated and measured energies are close to each other, indicating the validity of our model. Cleary, the energy increases with mode order, agreeing with the DA product trend.

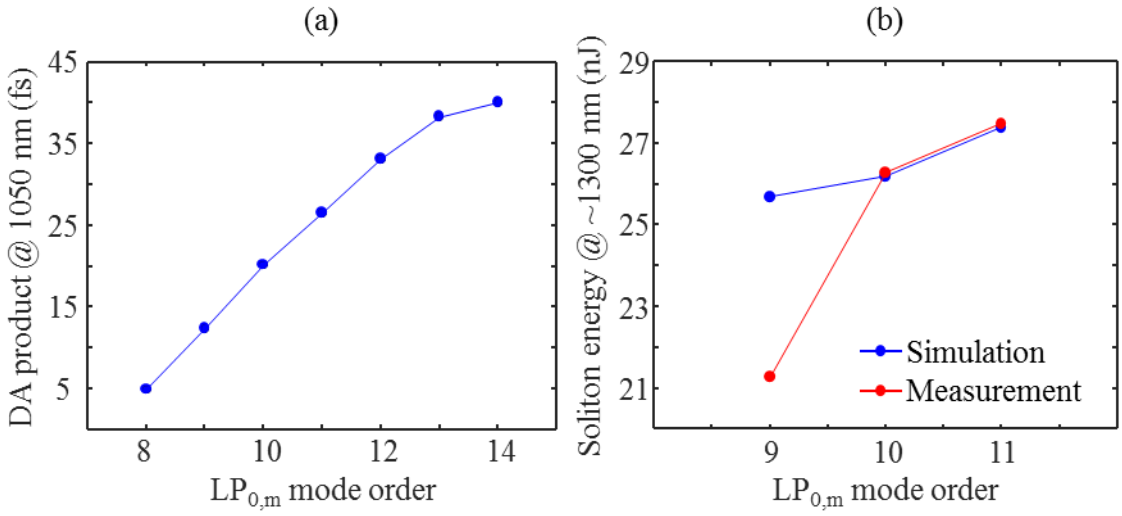

Figure 3.4: (a) Simulated DA product @ 1050 nm vs. mode order. (b) Simulated and experimentally measured soliton energy at ~1300 nm vs. mode order. Fiber parameters: core diameter: 48 μm, NA: 0.34, length: 37 cm.

3.1.4 Influence of fiber length on soliton energy and timing jitter

For the soliton at a fixed wavelength, its energy is affected by the fiber length. The physics explanation lies in the relation among wavelength shift speed, soliton bandwidth, and soliton energy. When fiber length becomes longer, the soliton wavelength shift needs to become slower in terms of the change in wavelength per fiber length, which corresponds to a smaller bandwidth and lower energy. Therefore, the longer the fiber, the lower the soliton energy. This trend is simulated (Fig. 3.5(a)), where the pump is a transform-limited Gaussian pulse width duration of 100 fs (FWHM), and the input pump power is adjusted to make the soliton wavelength reach ~1300 nm at the fiber output. As expected, the soliton energy decreases with fiber length.

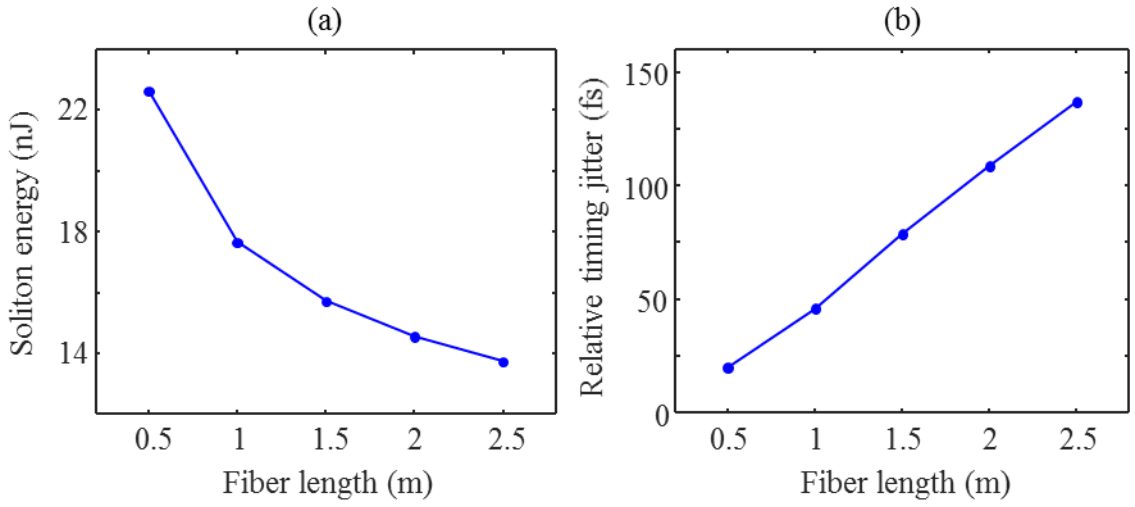

Figure 3.5: (a) The evolution of soliton energy with fiber length. (b) The evolution of RTJ with fiber length, under 1% pump power fluctuation. The pump is a Gaussian pulse with FWHM of 100 fs. The soliton wavelength is fixed to ~1300 nm. Fiber parameters: core diameter: 48 μm, NA: 0.34.

Another important property of a Raman soliton is the timing jitter. Since the dual color source, which will be described in chapter 6, requires a good temporal overlap between the

two pulses at different wavelengths, i.e. the remaining pump and Raman soliton, the discussion on the timing jitter in the thesis is only focused on the relative timing jitter (RTJ) between them. The fundamental reason causing the RTJ is the pump power fluctuation. When pump power changes, the soliton energy changes, resulting in the variation of soliton bandwidth and wavelength at the output, which translates into the RTJ due to the dispersion effect (Zhou et al., 2015). Since dispersion effect becomes stronger in longer fibers, the RTJ is expected to become more and more significant with fiber length. The trend is verified in the simulation (Fig. 3.5(b)), where the pump pulse is the same as that used in the simulation for Fig. 3.5(a), except the 1% pump power fluctuation is added.

Based on the analyses in this sub-section, it is clear that the shorter fiber length is beneficial for both enhancing soliton energy and reducing RTJ.

3.2 Soliton self-mode conversion

3.2.1 Theory

SSFS is an intrapulse Raman scattering process. Generally, the bandwidth of a soliton is only ~5 THz or even less, which is far away from that corresponding to the Raman gain peak, i.e. ~13 THz. This tells us the Raman gain SSFS uses is small, and SSFS is a weak wavelength translation process. However, in the extensive study on SSFS in single mode fibers (SMFs), to our best knowledge, it has never been seen that SSFS is suppressed and stopped by any other nonlinear wavelength conversion process except Cherenkov radiation. This seemingly surprising phenomenon can be explained using group refractive index (or group velocity) mismatch. SSFS is an ultrafast nonlinear process, the pulse

duration is generally only several hundreds of femtoseconds or even less, and any other nonlinear wavelength conversion process initiated by the soliton pulse generates new pulses at different wavelengths with comparable pulse durations, i.e. also ultrafast pulses. In SMFs, since there is only one mode (the fundamental mode), two ultrafast pulses at two different wavelengths propagate with different group velocities, so they easily walk off from each other, resulting in an insufficient interaction and inefficient conversion.

This walk-off fate in SMFs can be changed using MMFs. In MMFs, different modes at different wavelengths can have the same group refractive index (or group velocity). Therefore, if two pulses, in two different modes and at two different wavelengths, share the same group refractive index, they will temporally overlap and strongly interact with each other. However, only group refractive index matching is not enough. In Fig. 3.6(a), the relation between group refractive index and wavelength in a step-index MMF, with a core diameter of 48 μm and NA of 0.34, is shown for the $LP_{0,14}$ (solid blue), $LP_{0,13}$ (solid red), and $LP_{0,12}$ (solid green) modes. As seen from the figure, the distribution of the modes is relative sparse. When these three modes are group index matched, the frequency spans ~56 THz (~28 THz separation between two adjacent modes). Unless phase matching is properly designed, nonlinear wavelength conversion cannot happen between modes with such large frequency separation. The chance for the intermodal nonlinear wavelength conversion becomes higher when the distribution of modes becomes denser. One way to

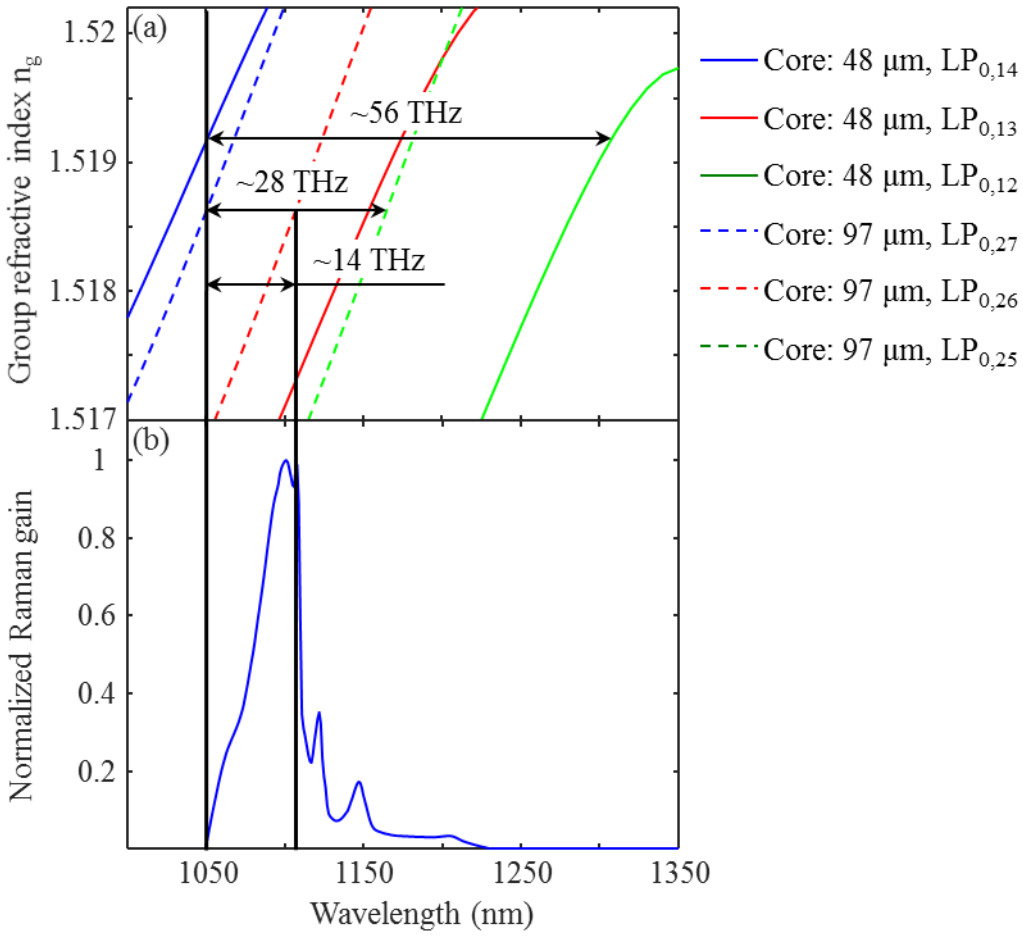

Figure 3.6: (a) Group refractive index vs. wavelength for different modes in two step-index MMFs. Fiber I: core diameter: 48 μm, NA: 0.34; fiber II: core diameter: 97 μm, NA: 0.34. (b) Normalized Raman gain profile.

enhance the distribution density is increasing the core size while keeping the NA unchanged. The dashed lines in Fig. 3.6(a) are group refractive indices for the $LP_{0,27}$, $LP_{0,26}$, and $LP_{0.25}$ modes in a MMF with a core diameter of 97 μm and NA of 0.34. In this fiber, the frequency span is reduced down to ~28 THz across the three modes when they are group index matched. Between two adjacent modes, the separation is ~14 THz, which overlaps with the high Raman gain region (Fig. 3.6(b)) (Agrawal, 2007). Under this situation, the two pulses (in $LP_{0,27}$ and $LP_{0,26}$ in this example) potentially achieves efficient

wavelength conversion, i.e. the shorter wavelength (higher frequency) pulse strongly transfers energy into the longer wavelength (lower frequency) pulse. Through the analysis above, it is learned the second requirement for the ultrafast intermodal wavelength conversion is that the modes need to stay at proper wavelengths so that either they are phase matched or the frequency separation coincide with the region of high nonlinear gain, such as Raman gain. There is one more requirement: the intermodal overlap integral needs to be non-zero. For Raman process, this quantity describes the similarity of the intensity profiles between the two interacting modes. The three requirements for the strong ultrafast intermodal interpulse (at different wavelengths) interaction are summarized below.

(1) The modes should be group refractive index matched, so that the pulses in them can propagate with the same velocity and overlap with each other.

(2) The wavelengths of the modes should allow for the phase matching, or the wavelength/frequency separation coincides with the region of high nonlinear gain.

(3) The interacting modes should have non-zero intermodal overlap integral.

When these three requirements are met, the SSFS can be suppressed, and even stopped by the intermodal interpulse process. The recently discovered SSMC is one such process (Fig. 3.7) (Rishoj et al., 2018). A soliton in a mode of high order ($LP_{0,21}$ (Fig. 3.7(b))) strongly interacts with a group refractive index matched mode of low order ($LP_{0,20}$ (Fig. 3.7(c))) based on the Raman scattering process, and achieves ~100% photon conversion from $LP_{0,21}$ to $LP_{,20}$. The generated $LP_{0,20}$ pulse is also a soliton. The SSMC process has been theoretically simulated (Antikainen et al., 2018) based on multimode GNLSEs (Poletti and Horak, 2008). The results also show that the process relies on the group index

matching and can achieve ~100% photon conversion.

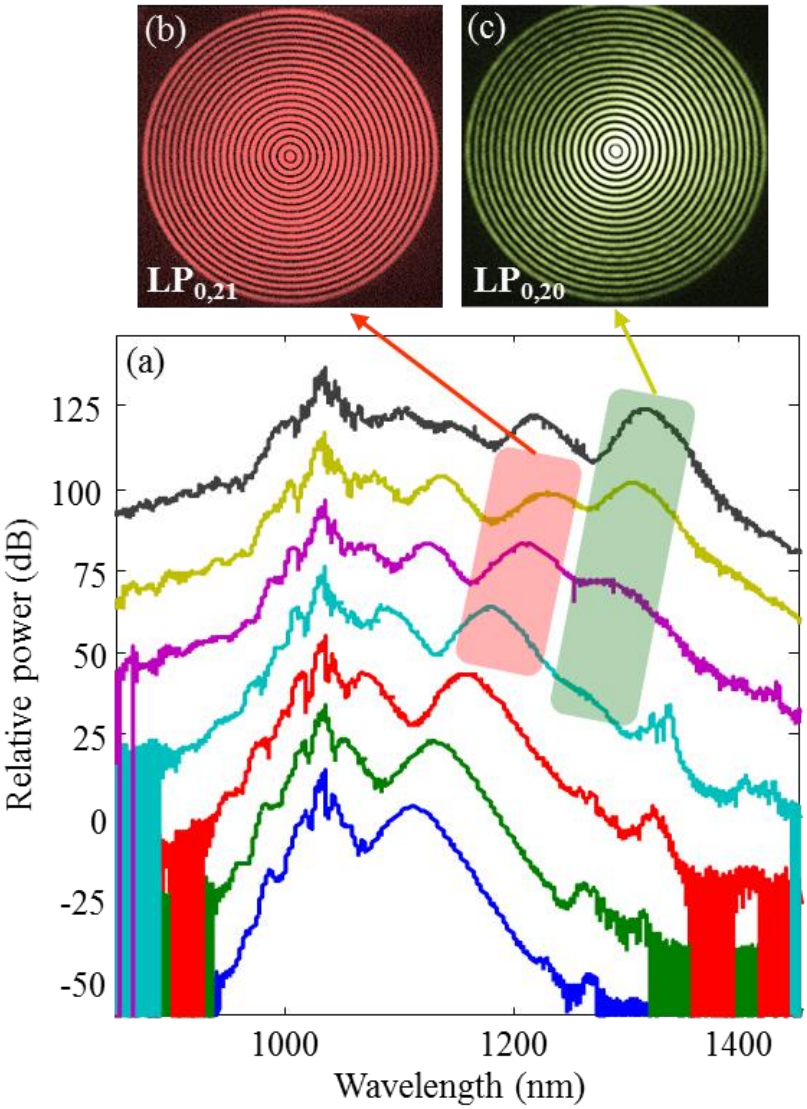

Figure 3.7: The recently discovered SSMC process. Fiber parameters: core dimeter: 97 μm, NA: 0.34, length: 54 cm. (a) Spectral evolution showing the energy transfer from (b) $LP_{0,21}$ mode to (c) $LP_{0,20}$ mode. (Data courtesy of Dr. Lars Rishøj)

3.2.2 Effect of dispersion-area product on soliton energy

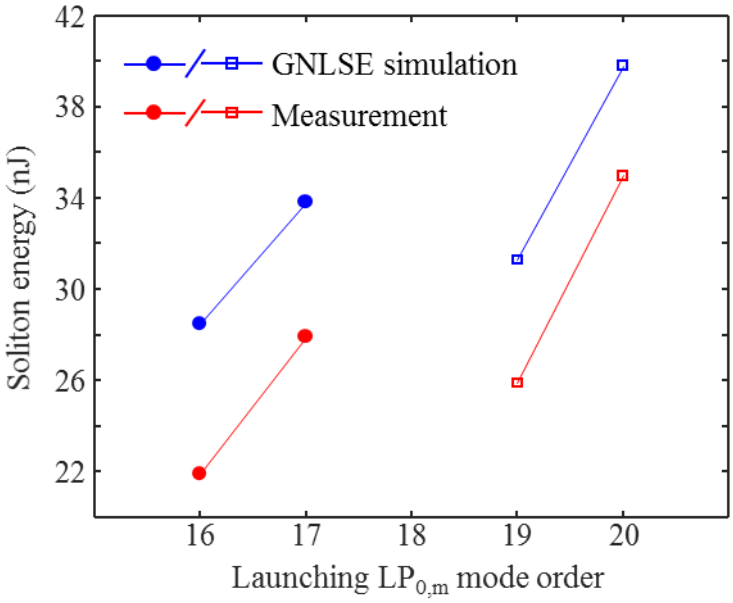

Figure 3.8: Simulated and experimentally measured soliton (generated by SSMC) energy vs. launching mode order. Fiber parameters: core diameter: 87 μm, NA: 0.34. For $LP_{0,16}$ and $LP_{0,17}$, the fiber length is ~5.02 m, and the soliton wavelength is ~1323 nm. For $LP_{0,19}$ and $LP_{0,20}$, those are ~2.51 m and ~1250 nm.

As will be shown in Chapter 5, the SSMC process conserves the number of photons, so the loss is only from photon-phonon interaction. As a result, like Raman soliton, the energy in the new soliton generated by SSMC can be calculated using the soliton energy at the pump wavelength. More importantly, the power scaling of SSMC process can also be achieved by scaling DA product at the pump wavelength. It has been shown more than once that DA product increases with mode order. Thus, it is expected for a given fiber length, and a given soliton wavelength, the energy of a soliton generated by SSMC increases with the launching mode order. The simulated and experimentally measured results are shown and compared in Fig. 3.8. In the simulation the input pump pulse is

created based on the measured pump spectrum and pulse duration. In addition, because GNLSE can only deal with SSFS, the energy of a soliton generated by SSMC is calculated using both GNLSE and the conservation of the number of photons. The details on both input pump pulse creation and soliton energy calculation will be given in Sec. 7.1.3. The simulated energies are close to the measurement, indicating the validity of our model. The increase in soliton energy with launching mode order clearly shows up, confirming the energies of solitons generated by SSMC can be scaled by scaling DA product at the pump wavelength.

3.3 Summary

This chapter has described the theory for both SSFS and SSMC. The main points are:

(1) For SSMC, it has been shown that the group refractive index matching, proper wavelength separation and non-zero intermodal overlap integral are the key parameters for the process to strongly occur.

(2) For both SSFS and SSMC, the soliton power scaling can be achieved by DA product scaling at the pump wavelength.

Chapter 4

Mode Conversion and Property Characterization

As mentioned in chapter 1, the higher order mode (HOM) excitation element is needed to implement HOM nonlinear processes. This chapter first presents several different ways to achieve mode conversion, focusing on two free-space techniques, of which the properties are discussed, such as conversion efficiency, excitation purity, and loss. The second part of this chapter focuses on the mode properties characterization, including dispersion and effective mode area, because of their close connection to soliton energy.

4.1 Binary phase plates

HOM excitation can be achieved by free-space techniques which exploit the similarity of electric fields. When two electric fields (denoted as a and b) are similar to each other in terms of both amplitude and phase, they can efficiently convert to each other. This similarity is measured using a quantity called overlap integral (OI) defined as

$$OI_{ab} = \frac{\iint_{\infty} \psi_a \psi_b^* r dr d\phi}{\sqrt{\iint_{\infty} |\psi_a|^2 r dr d\phi \cdot \iint_{\infty} |\psi_b|^2 r dr d\phi}} \tag{4.1}$$

The power conversion efficiency is the modulus square of OI

$$\eta = |OI_{ab}|^2 = \frac{\left| \iint_{\infty} \psi_a \psi_b^* r dr d\phi \right|^2}{\iint_{\infty} |\psi_a|^2 r dr d\phi \cdot \iint_{\infty} |\psi_b|^2 r dr d\phi} \tag{4.2}$$

Therefore, if a field similar to the target HOM hits on the input fiber facet, the HOM is then excited with high efficiency. Equation (2.5) shows that the electric fields of $LP_{0,m}$ modes possess assume the zeroth-order Bessel function, i.e. $E_{0,m}(r) \propto J_0(k_t r)$ in the guiding region, i.e. the core in a simple step-index multimode fiber (MMF), where k_t is the transverse wavenumber. The amplitude envelope decays in the form of $\sqrt{2/(\pi k_t r)}$ (Abramowitz and Stegun, 1965), and the phase assumes a binary profile, alternately switching between 0 and π along the radius.

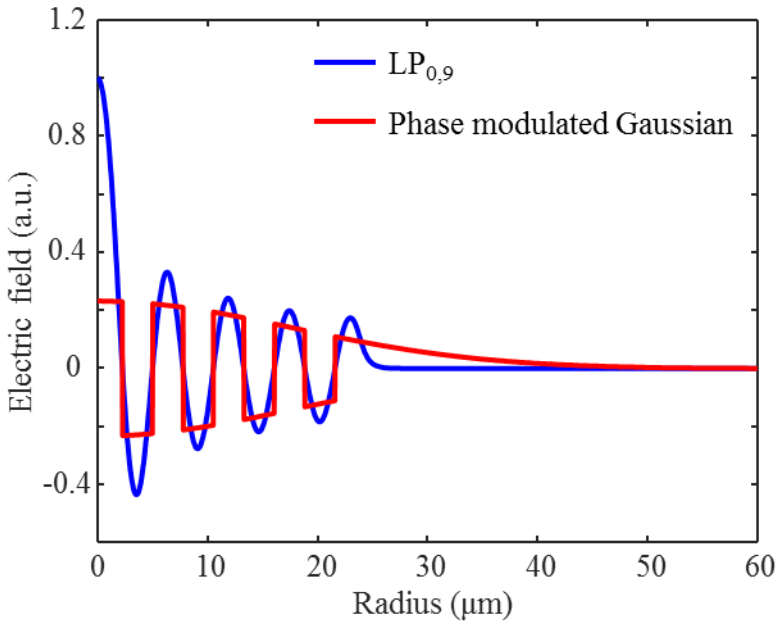

Figure 4.1: Comparison of the electric fields between the $LP_{0,9}$ mode of a step-index MMF (core diameter: 48 μm, NA: 0.34) and phase modulated Gaussian beam.

The simulated field of $LP_{0,9}$ mode in a step-index MMF with a core diameter of 48 μm and numerical aperture (NA) of 0.34 is shown in Fig. 4.1 (the blue trace). The $LP_{0,m}$ mode fields can be emulated by using a binary phase plate (BPP) which adds the alternate 0 and π phase to a collimated Gaussian beam. The switching positions between 0 and π

correspond to the nodes in the $LP_{0,m}$ mode fields. A simulated phase modulated Gaussian beam is shown in Fig. 4.1 (the red trace) for the comparison with the fiber mode. Indeed, these two fields are similar to each other, and an efficient conversion is expected.

However, the difference between the two fields is also obvious. For example, they have different envelopes. The difference limits the performance by excitation of parasitic modes, consisting of guided and radiation modes. The former parasitic content causes the so-called multipath interference (MPI) problem (Fludger and Mears, 2001), and the latter one causes the loss. The MPI is an undesired interference phenomenon originating from the existence of multiple mode channels, each of which experiences different phase shifts and interferes with the others. It can be expressed by the power ratio of parasitic to target mode. In order to measure the performance of BPP mode conversion systems exciting a specific $LP_{0,m}$ mode, three quantities are defined: conversion efficiency $\eta_{0,m}$ of which the expression is the same as Eq. (4.2), with field a being the input phase modulated Gaussian beam and field b being the target $LP_{0,m}$ mode; sum MPI defined as

$$\text{sum MPI} = 10\log_{10}\left(\sum_{n\neq m}\eta_{0,n}\Big/\eta_{0,m}\right) \tag{4.3}$$

and coupling loss defined as

$$loss = 10\log_{10}\left(\sum_{n}\eta_{0,n}\right) \tag{4.4}$$

In the definitions above, it is assumed the mode conversion system works in a azimuthally symmetric configuration, which is desired in experiments, and thus only $LP_{0,n}$ parasitic modes are considered (the overlap integral between the target $LP_{0,m}$ and any other mode is zero based on Eq. (4.1)). The sum MPI only considers the incoherent summation, i.e. the

power summation, over all the parasitic modes. Although the coherent crosstalk (Ramachandran et al., 2003), which affects performance of communication systems and also the output beam shape from a fiber source, is not taken into account, the optimization, i.e. the minimization, of the incoherent summation ultimately reduces the coherent crosstalk. Therefore, the sum MPI is still a fair metric for judging the quality of the mode conversion system.

The waist radius w_0 ($1/e^2$ radius) of the phase modulated Gaussian beam affects the performance of the BPP system. Its influence on the three quantities defined above is simulated and shown in Fig. 4.2. The fiber used in the simulation is step-index MMF with a core diameter of 48 μm and NA of 0.34. The target mode is $LP_{0,9}$. When the beam is very small, it is expected that most power is coupled into the guided modes, but due to field size mismatch, a good amount of power is in the parasitic modes, so the feature in this small beam regime is low conversion efficiency, high sum MPI and low coupling loss. With the beam size approaching the core size, the input field becomes more matched (similar) to the target $LP_{0,9}$ mode, increasing the efficiency, reducing the MPI and keeping the loss at a low level. When the input beam is roughly as big as the core, the highest efficiency and lowest MPI are achieved, and the loss is still relatively low. In the regime where the input beam is larger than the core, both the amount of power coupled into the radiation modes and the degree of field size mismatch between input field and target mode increases with the Gaussian beam size, resulting in decreased efficiency along with increased MPI and loss. Note that the Gaussian beam sizes corresponding to the maximal conversion efficiency and lowest sum MPI are not the same, but close to each other. Generally, in our

experiments the system operates at the lowest MPI point.

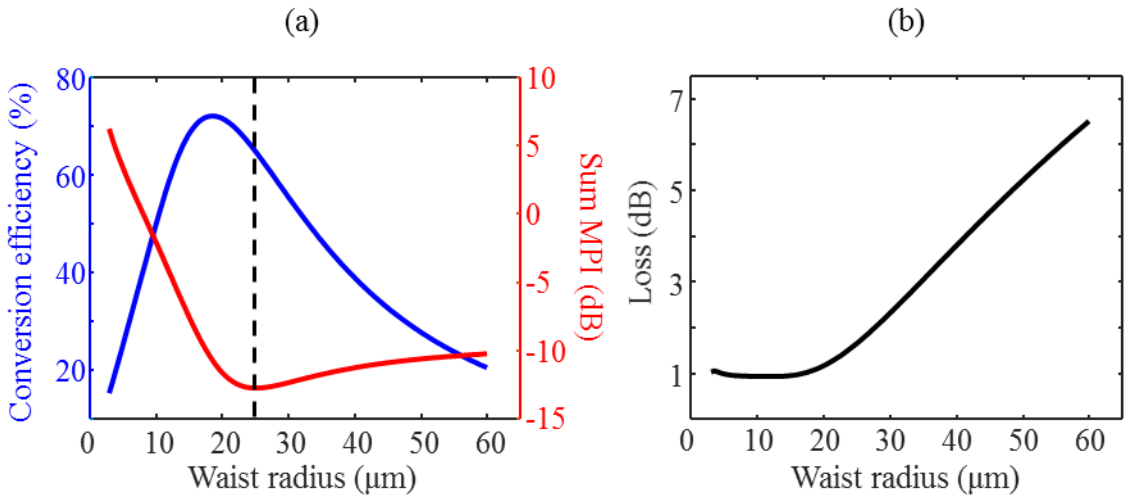

Figure 4.2: Influence of waist radius of the phase modulated Gaussian beam on the performance of BPP mode conversion system. (a) The influence on conversion efficiency and sum MPI. Note the waist radius corresponding to the lowest sum MPI is marked using the dashed line. (b) The influence on loss.

The BPP mode excitation setup in our laboratory is shown Fig. 4.3 (Demas et al., 2015). The BPP is implemented using a computer-controlled spatial light modulator (SLM) (X10468-08, Hamamatsu, Japan), The SLM has a pixel size of 20 μm × 20 μm, and responds to horizontally polarized light. The collimated Gaussian beam from the broadband laser (center wavelength: ~1045 nm, bandwidth: ~40 nm) is sent to the SLM which applies the alternate 0 and π binary phase profile. The phase modulated Gaussian beam is then imaged onto the input fiber facet by the aspherical lens. The fiber output beam is recorded using a silicon camera. In the experiments, a lensing effect needs to be added to the Gaussian beam by the SLM. The reason might be that the imaging system has some aberrations, such as spherical aberration, and the lensing effect can correct them to a large extent. The recorded pure-looking $LP_{0,9}$ mode is excited in the same MMF as that used for

the simulation in Fig. 4.2 (48 μm core diameter and 0.34 NA). It has been experimentally demonstrated that with a narrow band source (external cavity laser (ECL), center wavelength: 1050 nm, bandwidth: ~100 kHz), the HOM excitation using the BPP system can achieve the MPI and coupling loss close to the simulation results (Demas et al., 2015).

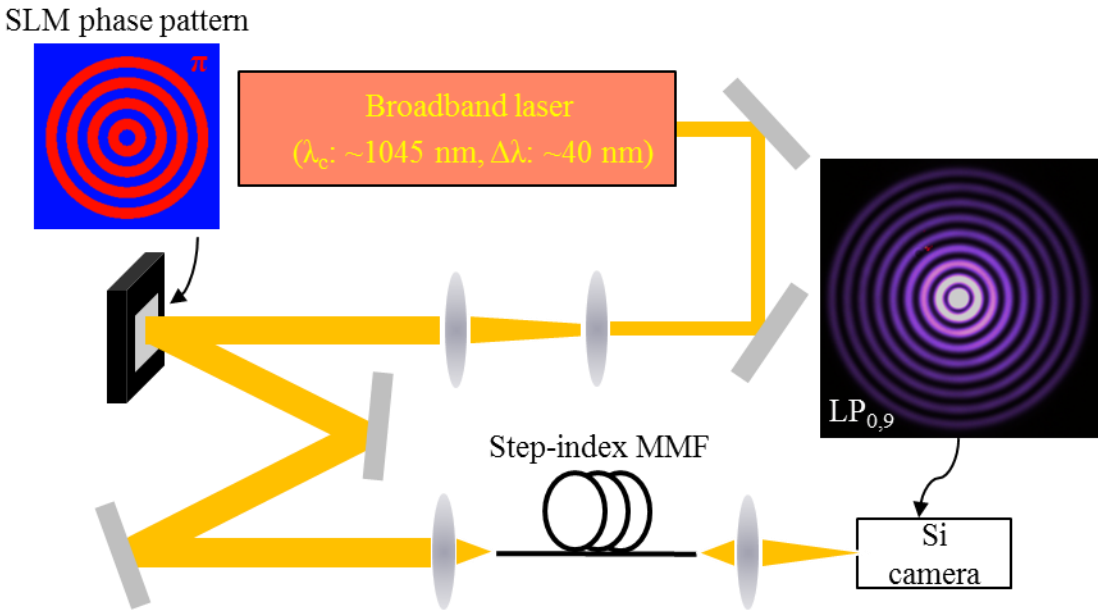

Figure 4.3: BPP mode excitation setup.

4.2 Axicons

Another free-space technique to do the HOM excitation is using an axicon. As mentioned in the previous section, free-space techniques use the field similarity to achieve mode conversion, so it is reasonable to expect that a component, which creates Bessel-like fields, can be used to excite $LP_{0,m}$ modes. Axicons are this type of components, and they have been demonstrated to be able to create Bessel beams in free space to manipulate biological samples and guide atoms (McGloin and Dholakia, 2005).

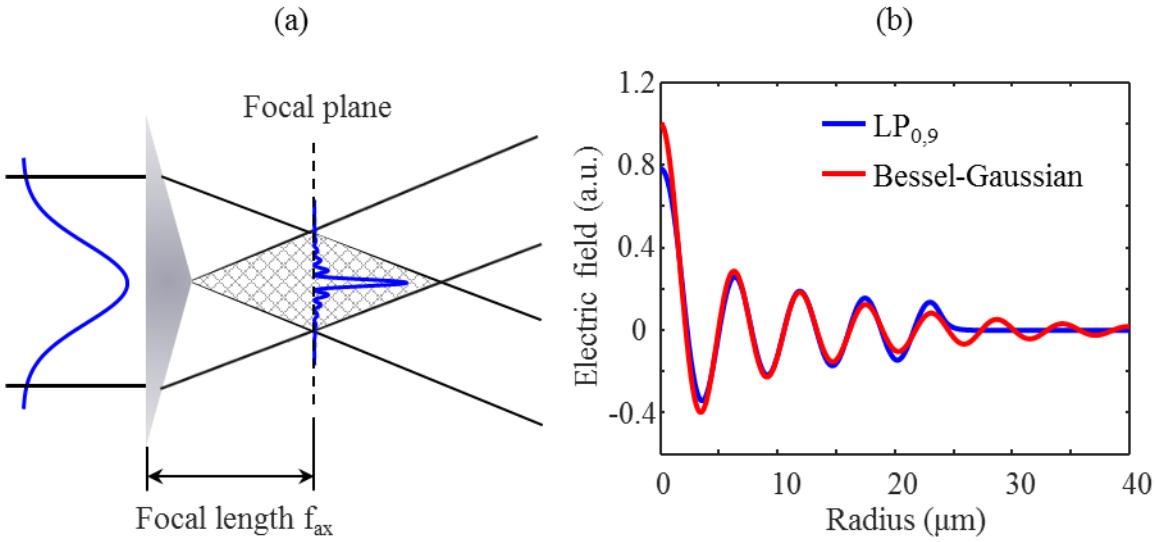

Figure 4.4: (a) The principle of operation of axicons. (b) Comparison of the electric fields between the $LP_{0,9}$ mode of a step-index MMF (core diameter: 48 μm, NA: 0.34) and Bessel-Gaussian beam.

Figure 4.4(a) shows the principle of operation of axicons. A collimated Gaussian beam is incident on an axicon, and then decomposed into a set of sub-waves, which propagate along the surface of a cone and interfere with each other. At the axicon focal plane a so-called Bessel-Gaussian beam (Demas et al., 2015), i.e. a Bessel beam with a Gaussian envelope, is created. The field of the beam is written as

$$E(r) = J_0(\kappa r)e^{-\frac{r^2}{w_{ax}^2}} \tag{4.5}$$

where κ is the transverse spatial frequency relating to the base angle α of the axicon by

$$\kappa = k_0(n-1)\alpha \tag{4.6}$$

where $k_0 = 2\pi/\lambda_0$ is the wavenumber in vacuum, and λ_0 is the wavelength in a vacuum. The parameter w_{ax} represents the size ($1/e^2$ radius) of the Gaussian envelope. To obtain a high conversion efficiency, the transverse spatial frequencies of the Bessel-Gaussian beam

and that of the target $LP_{0,m}$ mode need to match with each other. The intensity of a mode at the core-cladding interface is generally very small, which means $E_{0,m}(R_c) \propto J_0(k_t R_c) \approx 0$ and $k_t R_c \approx J_0^{(m)}$, where R_c is the core radius, and $J_0^{(m)}$ is the mth solution of $J_0(x) = 0$, so

$$k_t \approx \frac{J_0^{(m)}}{R_c} \tag{4.7}$$

Using Eqs. (4.6) and (4.7), the spatial frequency matching requirement can be written as

$$\alpha = \frac{J_0^{(m)}}{k_0 (n-1) R_c M} \tag{4.8}$$

where n is the refractive index of the axicon material, and M is the magnification factor of the imaging system (see the setup in Fig. 4.6) between the axicon and input fiber facet. The electrical field of $LP_{0,9}$ mode in a step-index MMF (core diameter: 48 μm, NA: 0.34), and that of the transverse spatial frequency matched Bessel-Gaussian beam are given in Fig. 4.4(b) to show the field similarity. Like the BPP system, although these two fields are similar to each other, they also have difference from each other. For instance, the Bessel-Gaussian beam has the Gaussian envelope, in contrast the $LP_{0,m}$ mode has the $\sqrt{2/(\pi k_t r)}$ envelope. The difference limits the performance of axicon HOM excitation systems.

The influence of Gaussian envelope size on the conversion efficiency, sum MPI and coupling loss is simulated and shown in Fig. 4.5. The fiber used in this simulation is the same step-index MMF as that used in the previous section (48 μm core diameter and 0.34 NA). The target mode is also $LP_{0,9}$. The simulation results are qualitatively the same as those of the BPP system, except part of the sum MPI result where the Gaussian envelope

is larger than fiber core. In the BPP system, in the large input beam regime, due to the field size mismatch, the sum MPI increases with the input beam size. However, in the axicon system, as seen from Eq. (4.5), the Bessel-Gaussian function monotonically approaches the ideal Bessel function with the input beam size, which improves the sum MPI at the expense of conversion efficiency.

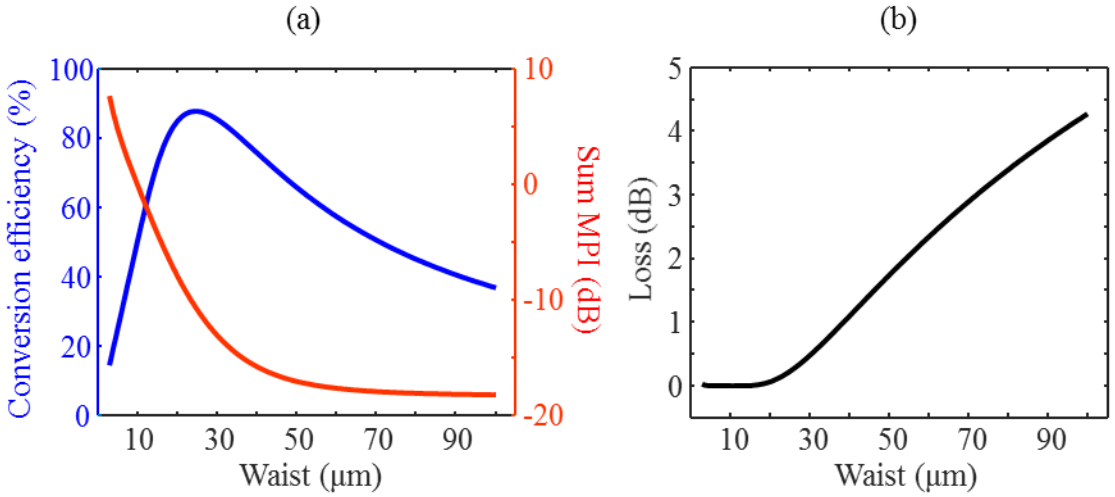

Figure 4.5: Influence of waist radius of the Gaussian envelope on the performance of axicon mode conversion system. (a) The influence on conversion efficiency and sum MPI. (b) The influence on loss.

Like BPPs, the phase profile of an axicon can be implemented using an SLM, and HOM excitation using the narrow band ECL (center wavelength: 1050 nm, bandwidth: ~100 kHz) has been demonstrated with sum MPI and coupling loss close to the simulation (Demas et al., 2015). However, for the practical applications, compact and portable light sources are preferred, and a small size or miniaturized component is a better choice than the bulky SLM. The HOM excitation setup, using a commercial physical axicon (AX252-C, Thorlabs, USA) with the base angle of 2º, is shown in Fig. 4.6. The collimated Gaussian beam from the broadband laser (center wavelength: ~1045 nm, bandwidth: ~40 nm) is sent

to the physical axicon, and forms a Bessel-Gaussian beam at the focal plane. This beam is then imaged onto the input fiber facet by the telescope between the axicon and fiber. In the experiments, when the output modes reach the purest state, this telescope does not operate in the ideal configuration, i.e. the distance between the two lenses is not the sum of their focal lengths. The reason might be this non-ideal configuration is needed to correct aberrations. The recorded pure-looking $LP_{0,9}$ mode is excited in the same MMF as that used for the simulation in Fig. 4.5 (48 μm core diameter and 0.34 NA). Since this setup is used to develop a compact source which will be presented in chapter 6, more details about the physical axicon HOM excitation can be found there.

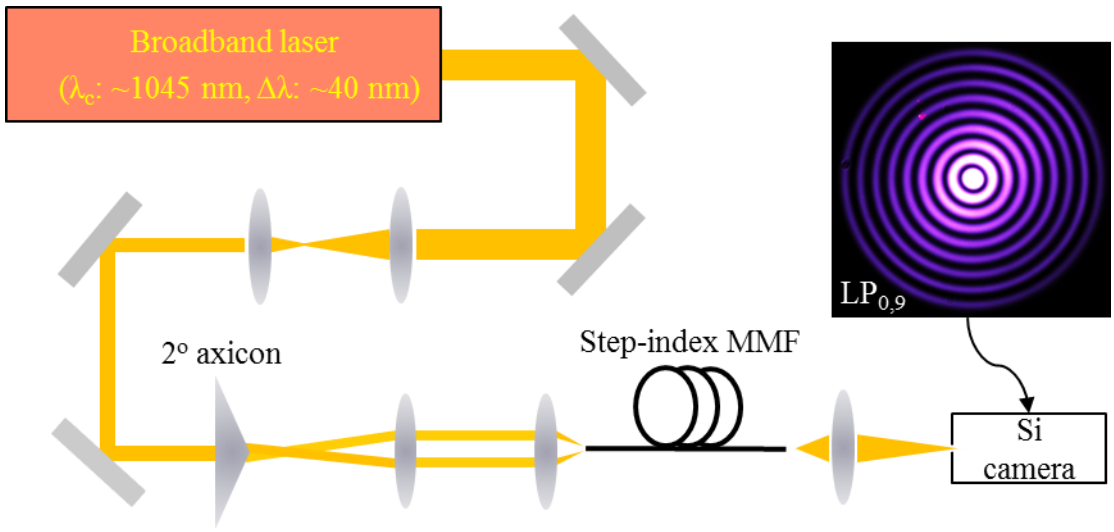

Figure 4.6: Axicon mode excitation setup.

4.3 Other mode conversion techniques

There are several in-fiber mode conversion techniques, which can have high conversion efficiency (> 99%), low insertion loss (< 0.2 dB), and large bandwidth (> 50 nm) (Ramachandran et al., 2002). Since these techniques do not serve the projects covered in

this thesis, they are just briefly described in this section.

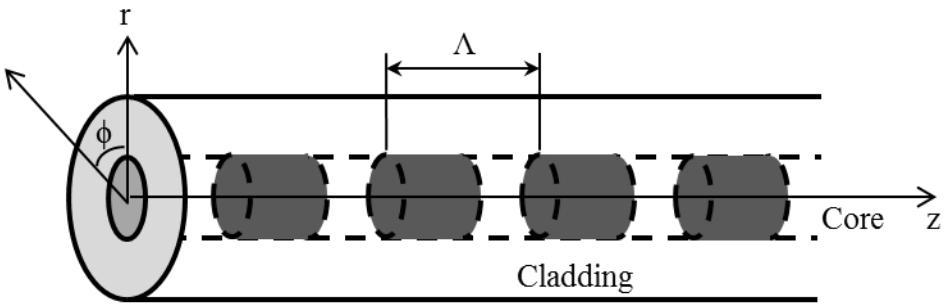

Figure 4.7: An LPFG with the grating period Λ.

One in-fiber technique is long period fiber grating (LPFG) (Erdogan, 1997). It is a device incorporating a modulation structure in the refractive index profile along the fiber axis (Fig. 4.7). Different modulation patterns can be used, including uniformly periodic, chirped, apodized, and so on, according to the specific applications. The refractive index modulation can be induced by ultraviolet light illumination (Hill et al., 1978), CO_2 laser illumination (Davis et al., 1998), mechanical pressure (Youngquist et al., 1984), electric arc discharge (Hwang et al., 1999), and acoustic wave (Kim et al., 1997). The mechanism of LPFG can be thought as conservation of momentum: a grating (periodic structure) provides a momentum of $2\pi/\Lambda$ to compensate the momentum mismatch between the two coupled modes $|\beta_1 - \beta_2|$.

Another in-fiber mode conversion technique is based on multimode interference (Yilmaz et al., 2007). In this method, a single mode fiber (SMF) is fusion spliced to a specific length of MMF. Multiple modes are excited in the MMF and interfere with each other. The resultant intensity profile evolves periodically along the propagation. At the MMF output, the target beam shape is achieved.

Fused coupler is also one fiber-based mode converter (Lai et al., 2007), where the mechanism is adiabatic propagation instead of resonant coupling, and thus is able to achieve very large operational bandwidth.

4.4 Mode property characterization

As shown in chapter 3, the soliton energy is proportional to the product of dispersion D and effective mode area A_{eff} (DA product), so it is useful (but not necessary all the time) to measure their accurate values to predict and explain the experimental phenomena. This section describes the basic methods to characterize these two properties.

4.4.1 Dispersion characterization

Dispersion describes the change in transit time of a pulse per unit wavelength and per unit length, so any measurement technique directly or indirectly reflecting the transit time τ can be used to characterize dispersion. One of these techniques is spectral interferometry (Menashe et al., 2001). The key underlying mechanism in this method is embodied by

$$\Delta\lambda = \frac{\lambda^2}{c \cdot |\Delta\tau|} \tag{4.9}$$

where $\Delta\lambda$ is the wavelength period in the interference spectrum, and $\Delta\tau$ is the differential transit time between two interference arms, i.e. the reference and fiber under test (FUT) arms. This expression clearly shows the link between the spectrum, a directly measurable property, and the transit time. The involvement of transit time of the reference arm can be erased by doing the cutback measurement on the FUT. The setup, characterizing the

dispersion of $LP_{0,2}$ mode in a few-mode fiber (FMF) around 1050 nm, is shown in Fig. 4.8. This configuration is just a fiber-based Michelson interferometer. The light from the LED (center wavelength: 1050 nm) gets split by the 3dB single mode fused coupler, and then sent to both reference and FUT arms. These two arms have ~48 cm length of SMF and ~66 cm length of FMF, spliced to the coupler pigtails, respectively. The end facet of reference arm is an angle cleave (~8°) to avoid the reflection from it, and the light sent to this arm is ultimately reflected by the mirror and coupled back into the SMF. The end facet of FUT arm is a flat cleave (< 0.5°), which reflects light with ~4% efficiency. The reflected light from both arms meets each other in the SMF of the output port, interferes, and then gets detected by the OSA.

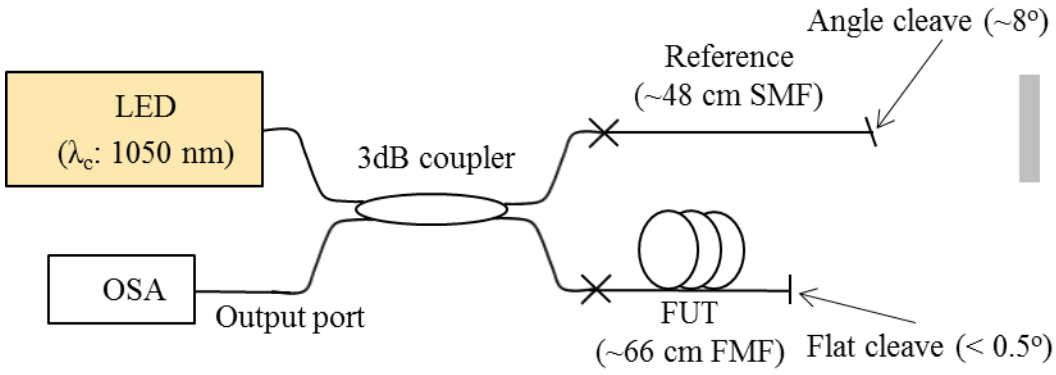

Figure 4.8: Dispersion characterization setup.

Several items need to be paid attention to. 1) The SMF-FMF splice should be optimized to mainly excite only the $LP_{0,1}$ and target mode ($LP_{0,2}$ in this example) to reduce complexity of the interference spectrum. 2) The differential transit time $\Delta\tau$ cannot be too small. Otherwise, the wavelength period is too large to observe within the wavelength range of the light source. 3) The differential transit time $\Delta\tau$ cannot be too large, either. Otherwise,

the wavelength period is too small to resolve by the OSA. 4) Any source of parasitic spectrum fluctuation/oscillation, i.e. the noise background, such as power fluctuation with wavelength from the light source and mechanical vibration of the optical table, should be minimized and/or characterized (this characterization result is then used to discriminate the signal against parasitic spectral oscillation).

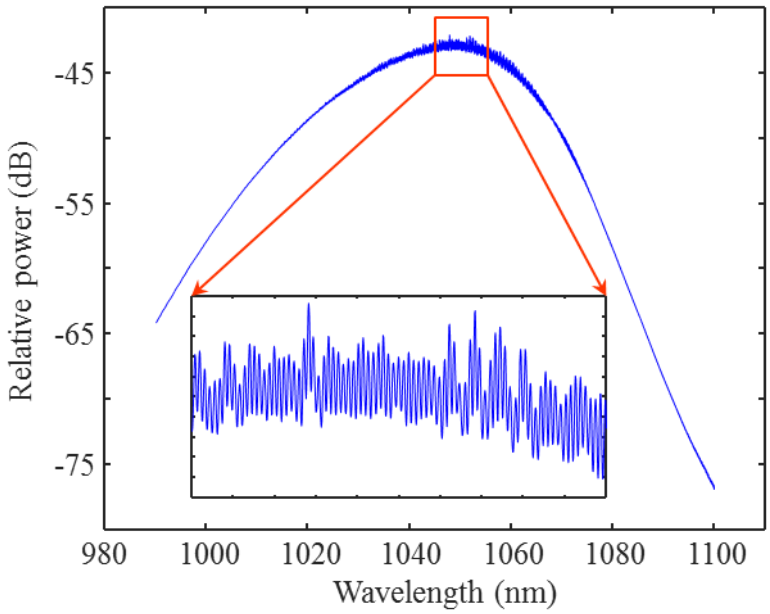

Figure 4.9: Noise background in the dispersion measurement experiment.

In the experiment, the resolution and sampling step of the OSA are set to 0.05 nm and 0.01 nm, respectively. The noise background (Fig. 4.9) is first characterized by recording the spectrum while the end facet of FUT arm is immersed in the index-matching oil, a medium having the same index as the silica fiber and preventing the reflection at the facet. The parasitic spectral fluctuation/oscillation clearly shows up, especially around the center wavelength of the light source.

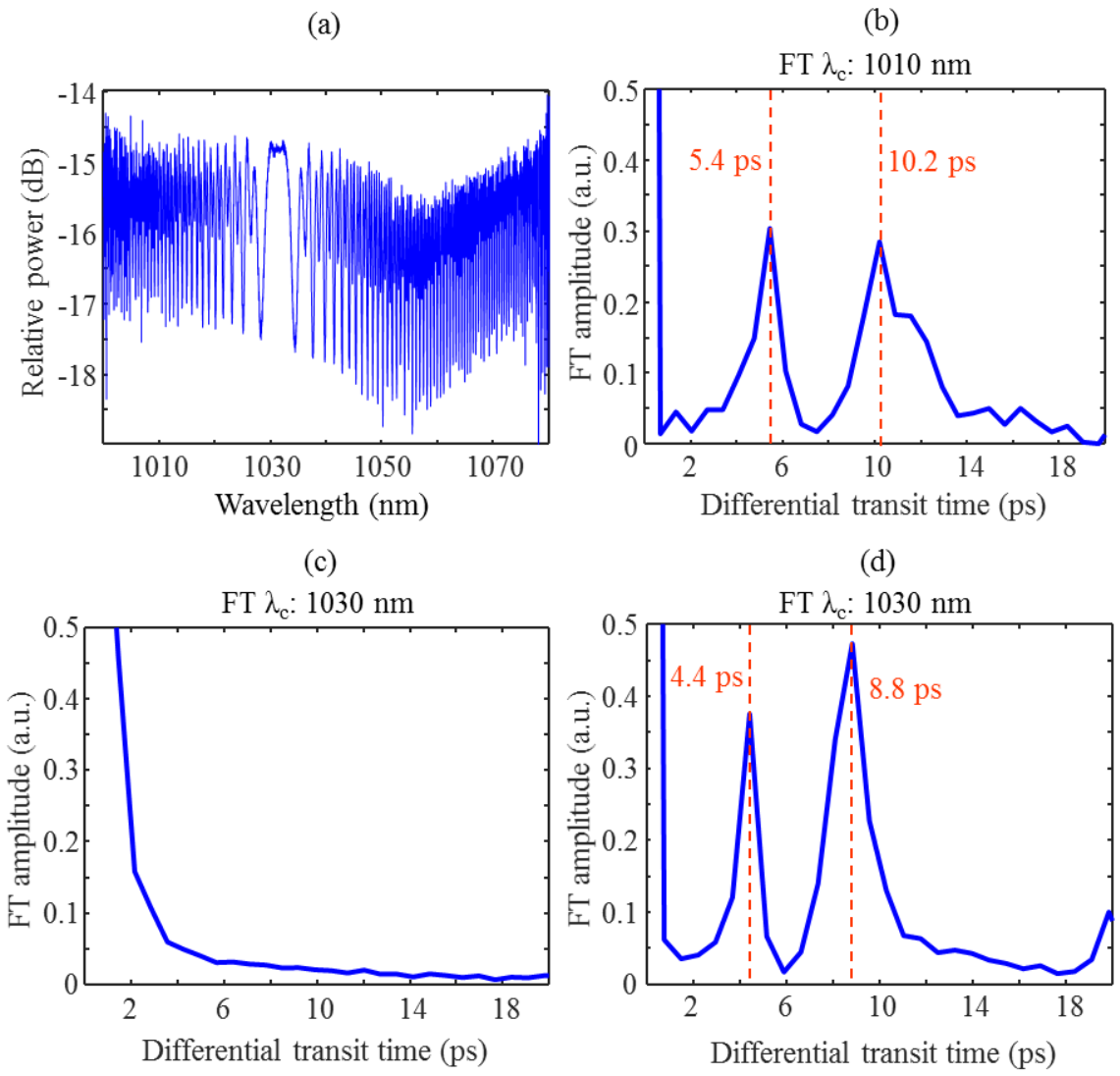

Figure 4.10: (a) The self-interference spectrum. (b)-(d) are the FT traces of the spectrum in (a) at some representative wavelengths. The two strong FT peaks, both corresponding to the $LP_{0,1}$-$LP_{0,2}$ interference, are marked using the dashed lines.

After measuring the noise background, the end facet of FUT arm is taken out of the oil and cleaned using alcohol (re-cleaved if needed). Next, the interference between the modes in the FMF itself (called self-interference) needs to be measured in order to 1) confirm the SMF-FMF splice mainly excites only the $LP_{0,1}$ and $LP_{0,2}$ modes; and 2) obtain the differential transit time between these two modes (the purpose will be shown later). In this

measurement, the beam path between the end facet of reference arm and the mirror is blocked, and the end facet can be immersed in the oil if needed (the ~8° angle cleave is able to well reduce the back-reflection from the facet, but one may still put it in the oil just to absolutely make sure the reflection does not occur). The self-interference spectrum is shown below (Fig. 4.10(a)). The nature of strong oscillation in interference clearly shows up, and the turn-around point (TAP), represented by large wavelength period, appears at ~1030 nm, agreeing with the simulation.

However, there is seemingly more than one oscillation frequency, indicating more than two interference arms exist due to the unsatisfactory SMF-FMF splice. To learn more about the spectrum, Fourier transform (FT) is implemented. The bandwidth of the FT mask, i.e. a moving wavelength window where the FT is calculated, is 5 nm, and the scan step of the mask is 1 nm. The FT operation scans from 1000 nm to 1080 nm. The FT traces at some representative wavelengths are shown in Fig. 4.10(b)-(d). These FT results are quite informative. First, except at ~1030 nm, the FT always gives two comparably strong peaks in the non-zero differential transit time regime (The strong peak, at zero differential transit time, is ignored, because it just represents incoherent power summation of all the interference arms, and has nothing to do with the oscillation feature of the interference spectrum). This seemingly indicates two different pairs of modes interfere. Second, that no strong peak appears at ~1030 nm means TAP occurs on both pairs of modes at (about) the same wavelength. According to the simulation, from 1000 nm to 1100 nm the TAP happens only on $LP_{0,1}$-$LP_{0,2}$ pair at 1027 nm. This indicates a situation where the two FT peaks actually both come from interference between the $LP_{0,1}$ and $LP_{0,2}$ modes, but correspond

to different interaction length (The interaction length is a distance over which the differential transit time $\Delta\tau$ between two interference arms accumulates). Third, the ratio of the differential transit time, corresponding to the two strong FT peaks, is always ~2. This nearly constant ratio phenomenon strengthens the previous speculation and makes it more complete: the ratio of interaction length of the two pairs of interference arms, which use the same pair of modes, is 2. In addition, the interaction length is probably independent of wavelength. Therefore, it is believed that the two pairs of interference arms, both using the $LP_{0,1}$ and $LP_{0,2}$ mode pair but with a constant differential interaction length (one is twice larger than the other), form the two oscillation frequencies in the self-interference spectrum. One pair of interference arms (pair A in Fig. 4.11(a)) are $LP_{0,1}$ and $LP_{0,2}$ co-propagating all the way together, i.e. co-propagate to the end facet, get reflected together and remain in the respective mode, and then co-propagate back. During this process, the differential transit time between the two arms accumulates over double length of the FMF. The other pair (pair B in Fig. 4.11(b)) may be that $LP_{0,1}$ propagates to the end facet and gets reflected. At the reflection, mode conversion happens: a small amount of $LP_{0,1}$ is converted to $LP_{0,2}$, and then co-propagates with the remaining $LP_{0,1}$ back to the coupler. Thus, the differential transit time only accumulates after the reflection, i.e. over single length of the FMF (half of pair A).

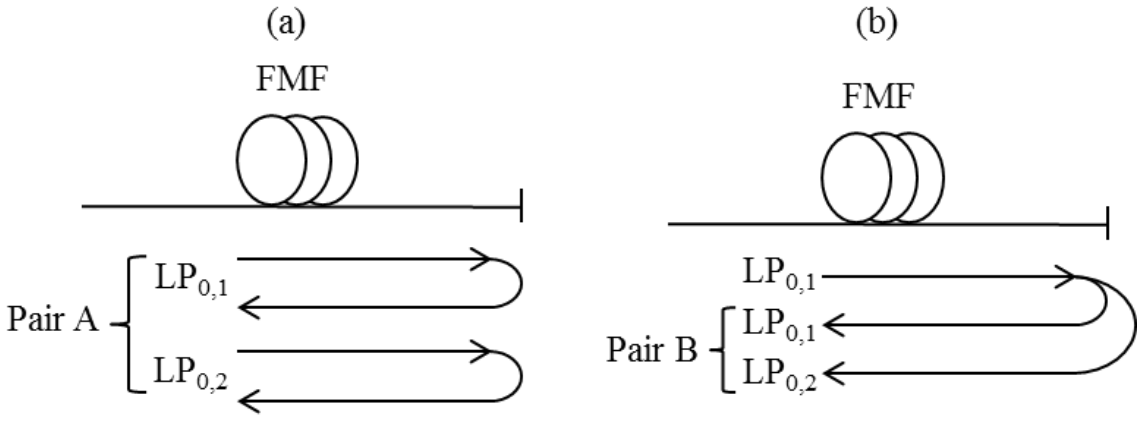

Figure 4.11: The two pairs of interference arms corresponding to the two strong peaks in FT traces of the self-interference spectrum. (a) The pair accumulating differential transit time over double length of the FMF. (b) The pair accumulating differential transit time over single length of the FMF.

Finally, the interference spectrum between the reference and FUT arms (called cross-interference) is measured (Fig. 4.12(a)). FT is implemented on this cross-interference spectrum using the same parameters as those on self-interference spectrum. The representative FT traces are given in Fig. 4.12(b)-(d) at the same wavelengths as those in Fig. 4.11 (b)-(d). There is only one strong peak in each FT trace, which should correspond to the interference between the reference and "FUT $LP_{0,1}$ only" arms. The differential transit time between the two arms is $|\Delta\tau_{0,1}| = |\tau_{ref} - \tau_{0,1}|$, where τ_{ref} and $\tau_{0,1}$ are the transit time of reference and "FUT $LP_{0,1}$ only" arms, respectively. In each cross-interference FT trace, one of the small peaks should correspond to the interference between the reference and "FUT $LP_{0,2}$ only" arms with $|\Delta\tau_{0.2}| = |\tau_{ref} - \tau_{0,2}|$, where $\tau_{0,2}$ is the transit time of "FUT $LP_{0,2}$ only" arm. Hence, the temporal separation between these two peaks should be the differential transit time between the $LP_{0,1}$ and $LP_{0,2}$ modes accumulated over double length

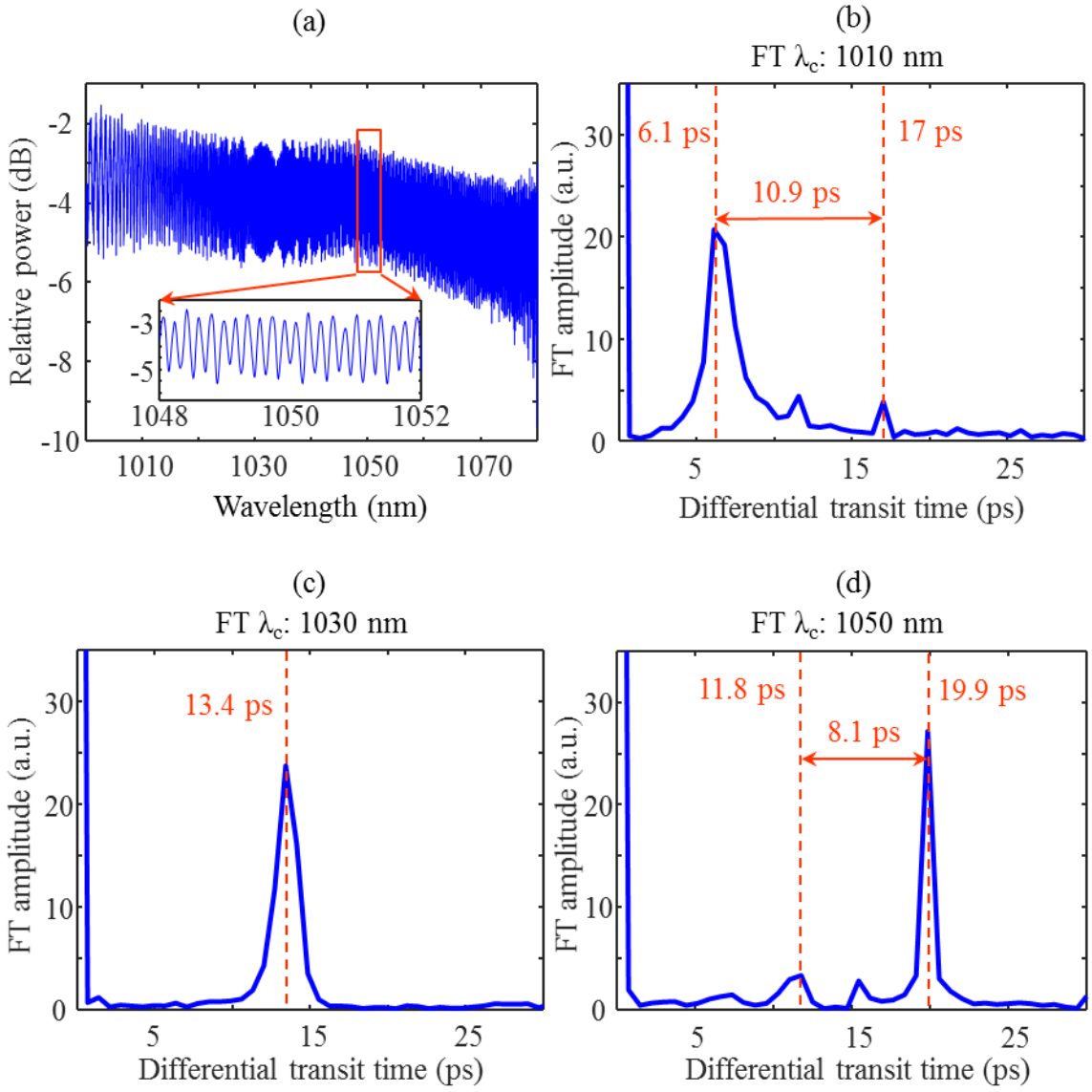

Figure 4.12: (a) The cross-interference spectrum. Part of the dense interference spectrum is zoomed in to clearly show the oscillation. (b)-(d) are the FT traces of the spectrum in (a) at some representative wavelengths. The strong FT peak corresponding to the reference-(FUT $LP_{0,1}$) interference and the small FT peak corresponding to reference-(FUT $LP_{0,2}$) interference are marked using the dashed lines.

of the FMF, which is exactly the temporal coordinate of pair A in the FT traces of self-interference spectrum. Using this relation, $\left|\Delta\tau_{0,2}\right|$ can be predicted. The validity of this relation is confirmed by the fact that there is indeed a peak appearing at the predicted

coordinate (Fig. 4.12(b)-(d)). Note that FT is also implemented on the noise background spectrum, and the comparison between these FT traces and those of self- and cross-interference spectra is done to make sure the FT peaks used to calculate the dispersion are not from the background.

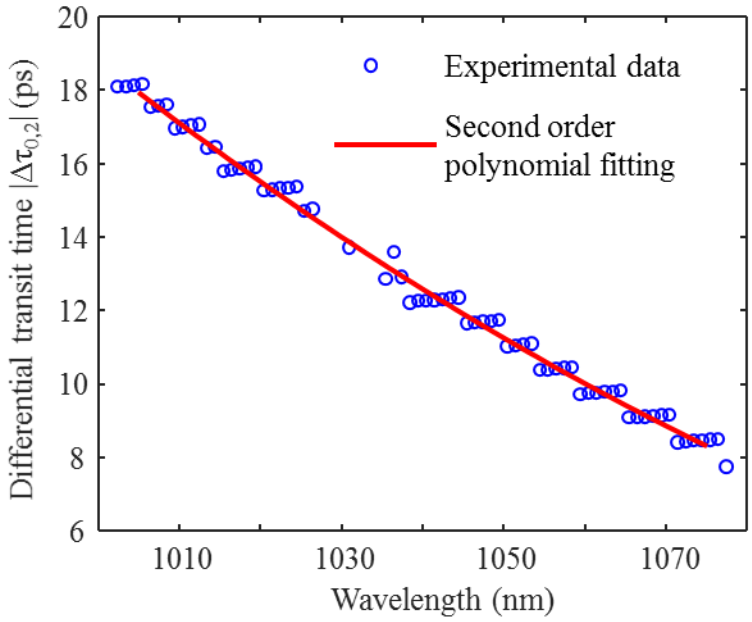

Figure 4.13: Raw data showing $|\Delta\tau_{0,2}|$ v.s. λ (the blue scattered data points) and the 2nd order polynomial fitting (the red curve).

The differential transit time $|\Delta\tau_{0,2}|$ at each FT center wavelength λ can then be calculated (the blue scattered data points in Fig. 4.13). The staircase shape is due to the temporal resolution determined by

$$\Delta t_{resolution} = \frac{\lambda^2}{c \cdot B} \tag{4.10}$$

where B is the FT bandwidth (5 nm in this example). The resolution is calculated to be 0.7 ps. For the data points on the same level of the staircase, the differential $\Delta\tau_{0,2}$ is smaller

than the resolution, and cannot be resolved. The 2nd order polynomial fitting is used to find out the functional relation between $\left|\Delta\tau_{0,2}\right|$ and λ for the ~66 cm length of FMF (the red curve in Fig. 4.13).

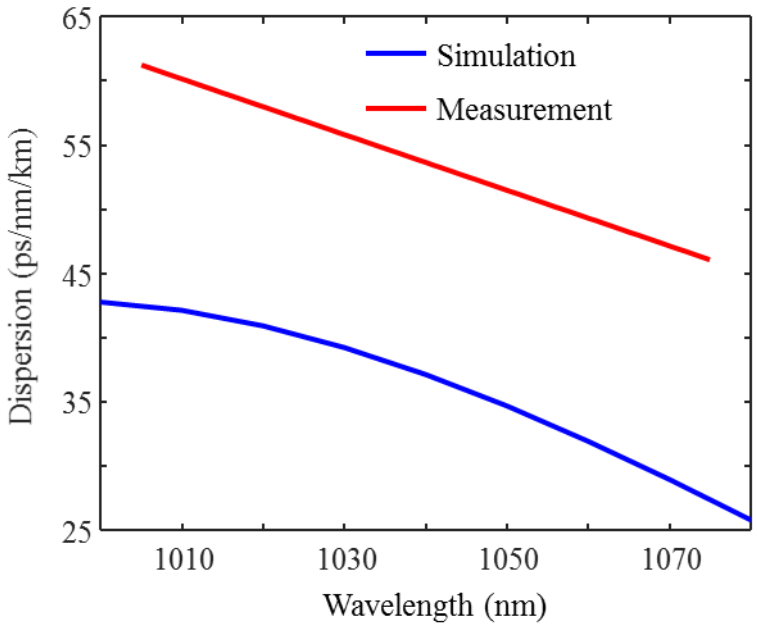

Figure 4.14: Comparison between the simulated and measured $LP_{0,2}$ dispersion.

The FMF is then cut back by ~34.6 cm, and then the same measurement and data analysis procedure is done on this new length. The $LP_{0,2}$ dispersion is then calculated using the expression

$$D = \frac{\frac{d\left|\Delta\tau_{0,2}\right|_2}{d\lambda} - \frac{d\left|\Delta\tau_{0,2}\right|_1}{d\lambda}}{2\cdot L_{cutback}} \tag{4.11}$$

where $\left|\Delta\tau_{0,2}\right|_2$ and $\left|\Delta\tau_{0,2}\right|_1$ correspond to "after cutback" and "before cutback", respectively. Note that the expression is only valid when the transit time of reference arm is larger than that of "FUT $LP_{0,2}$ only" arm, which is satisfied in the experiment. The

comparison between the simulated and measured $LP_{0,2}$ dispersions is shown in Fig. 4.14. The measurement obtains the anomalous dispersion and negative dispersion slope, which agree with the simulation.

The mechanism of this spatial interferometry also applies to highly MMFs. However, the splice needs to be replaced by a mode converter of high efficiency, because it is nearly impossible to mainly excite only the $LP_{0,1}$ and target mode by splicing optimization.

Dispersion can also be directly characterized in time domain using time-of-flight measurement (Lin et al., 1983; Cohen, 1985). In the experiment, a wavelength tunable pulse laser and a sampling oscilloscope are needed. For a given pulse shown in the oscilloscope, the time coordinate τ versus wavelength λ relation can be easily acquired. The dispersion is then calculated by doing the derivative on τ vs. λ curve.

4.4.2 Effective mode area characterization

The measurement of effective mode area A_{eff} is based on its definition Eq. (2.10). The setup for measuring A_{eff} of the $LP_{0,2}$ mode in the same fiber as that in Sec. 4.4.1 is shown in Fig. 4.15(a). The light from a narrow band laser diode (QSSLD-1030-1, Qphotonics, USA) (center wavelength: 1030 nm, bandwidth: < 0.01 nm) is coupled into a SMF which connects to the FMF by an optimized splice (MPI ≤ -34 dB). An LPFG of high conversion efficiency (~20 dB at 1030 nm) is used to excite the $LP_{0,2}$ mode. The fiber output mode image is recorded by the Indium-Gallium-Arsenide (InGaAs) camera. In order to determine the magnification factor of the imaging system, the stage, which holds the fiber sample, is transversely translated by 25 μm, the corresponding change in the position of mode image

is measured to be 4.53 mm, so the magnification factor is 181.2.

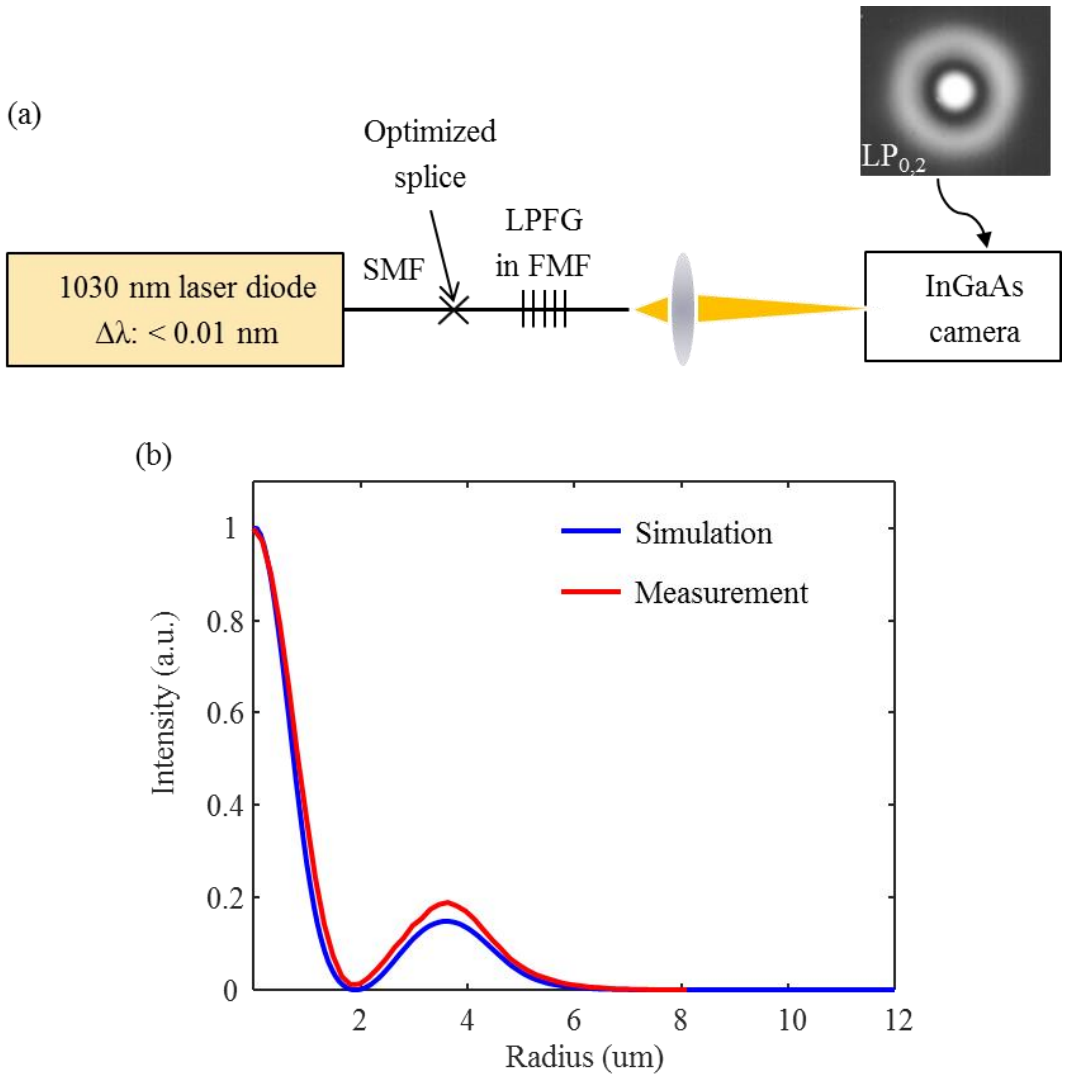

Figure 4.15: (a) Effective mode area characterization setup. (b) Comparison between the simulated and measured $LP_{0,2}$ intensity profiles.

The linecut profile $I(r)$ is obtained by first taking four linecut profiles along different directions (0^o, 90^o, 180^o, and 270^o), and then scaling down the averaged result by the measured magnification factor. The simulated and measured intensity profiles are compared in Fig. 4.15(b). The effective mode area A_{eff} is calculated using the expression

(derived from Eq. (2.10))

$$A_{eff} = \frac{2\pi\left(\int I(r)rdr\right)^2}{\int I^2(r)rdr} \tag{4.12}$$

The result is 53 μm^2, which is close to the simulation (44 μm^2).

4.5 Summary and discussion

This chapter has described different ways to realize mode conversion, and the methods to characterize the mode properties (dispersion and effective mode area). Among the mode conversion techniques, for the purpose of mode properties test, the free-space techniques, i.e. BPP and axicon systems, are better, because they can quickly switch between different modes (the mode switching in the SLM-based BPP setup can be done by just changing a number in a Labview program without the need of any addition alignment), allowing for efficient characterization on different modes and choosing the best one for subsequent experiments within days. In contrast, it takes much longer to just find out the proper recipe for fiber device fabrication. However, in terms of conversion efficiency, MPI and loss, in-fiber devices, at least LPFG, are better. With proper writing parameters, LPFG can achieve > 20 dB depth (> 99% conversion efficiency), corresponding to sum MPI < -20 dB (the magnitude of sum MPI of an LPFG is approximately equal to the depth). The insertion can be < 0.2 dB. In the free-space systems, the conversion efficiency is < 90%, the sum MPI is > -20 dB, and the loss is generally ~1 dB. Besides, in-fiber devices are more compact and easier to integrate with other systems than the free-space components. Therefore, the free-space methods are more proper for research purpose, and in-fiber techniques are better for

making compact devices for specific applications.

Between the two free-space HOM excitation techniques, the advantage of the BPP setup is that it does not require addition alignment when switching to a different mode; and that of the axicon setup is that it achieves lower MPI and loss.

Finally, since all the HOM excitation techniques are reciprocal, it is expected that they can also achieve the conversion from HOMs back to Gaussian beam, with (relatively) low loss and good beam quality in terms of M^2. The use of free-space mode conversion systems for both HOM excitation and re-conversion back to Gaussian will be shown in next two chapters.

Chapter 5

Cascaded Soliton Self-Mode Conversion

As mentioned in chapter 1, based on the recently discovered intermodal interpulse Raman scattering process—soliton self-mode conversion (SSMC), it has been demonstrated that the strong pulses are generated at ~1300 nm, with pulse energies of ~80 nJ and peak powers of ~1.1 MW (Rishoj et al., 2018). In the experiment, this intermodal process occurred only once between two specific modes ($LP_{0,21}$ and $LP_{0,20}$). The question then naturally arises as to whether this process can occur multiple times and involve multiple modes. In this chapter, we extend the study from single time intermodal interpulse interaction to multiple times, and investigate its properties as a function of fiber length (Sec. 5.1) and input pump power (Sec. 5.2). This experiment is in collaboration with Dr. Lars Rishøj. The competition between soliton self-frequency shift (SSFS) (Mitschke and Mollenauer, 1986) and SSMC is briefly discussed in Sec. 5.3.

5.1 Cascaded SSMC as a function of fiber length

The experimental setup for characterizing the nonlinear process is shown in Fig. 5.1. The pump for the experiments is a commercial fiber laser (Y-Fi, KMLabs, USA) which outputs nearly transform-limited pulses at 1045 nm, with pulse durations of ~100 fs. The half-wave plate and polarization beam splitter (PBS) right after the pump laser are used to tune the pump power launched into the fiber sample. The specific higher order mode (HOM) excitation is achieved by using binary phase plate (BPP) method (Demas et al., 2015) (read

Sec. 4.1 for details). On the fiber output side, several instruments are used to do the characterization. The silicon camera is used to check the mode excitation quality at the low power level, i.e. no nonlinear effect occurs. The spectrum is measured with the optical spectrum analyzer (OSA). The soliton is spectrally isolated using the long-pass filter (LPF) and its properties, including pulse duration, pulse energy, and mode content, are characterized using the auto-correlator, Germanium (Ge) power meter, and Indium gallium arsenide (InGaAs) camera.

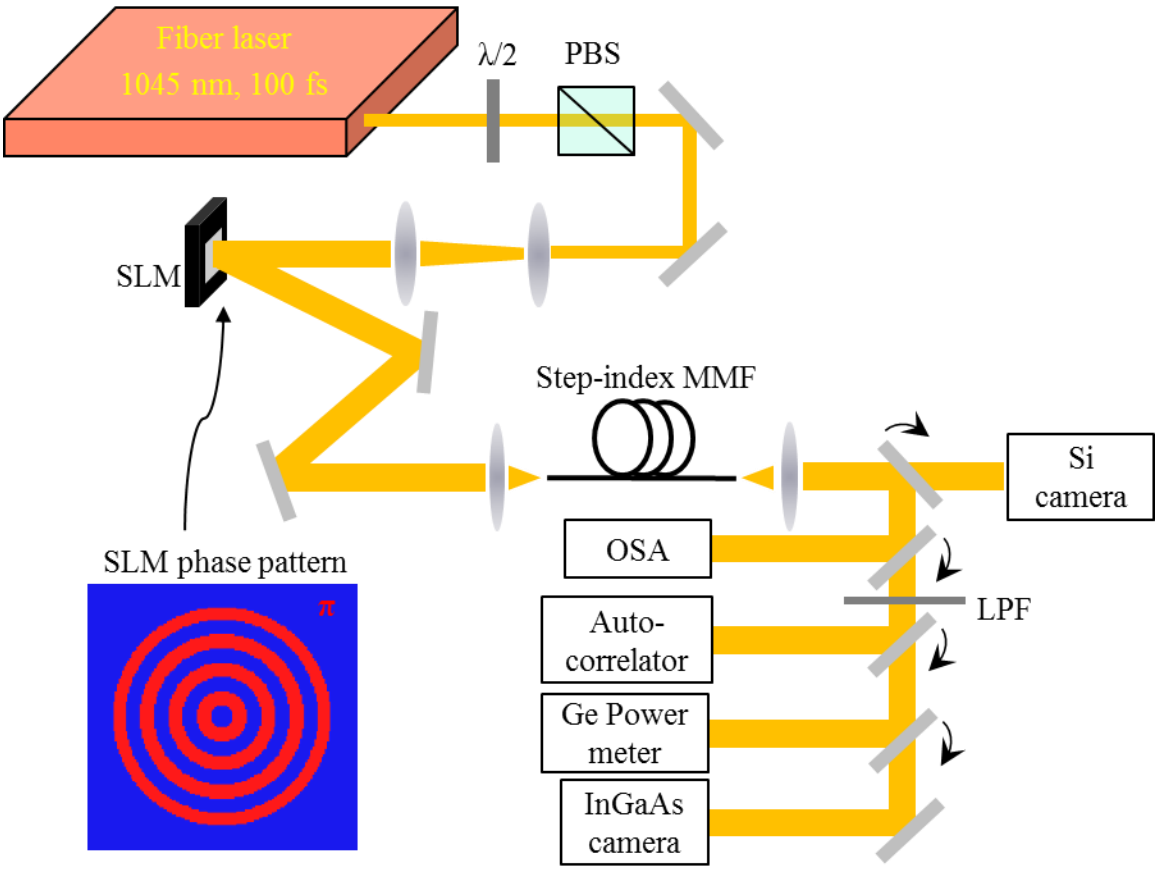

Figure 5.1: Experimental setup for characterizing the nonlinear process.

The step-index multimode fiber (MMF) used in the experiments has a core diameter of 87 μm and numerical aperture (NA) of 0.34 (Fig. 5.2(a)). The target launching HOM is

$LP_{0,19}$, of which the pure excitation is shown in Fig. 5.2(b). The original fiber length is 12 m, and the cutback measurement is used to investigate the dynamics of the nonlinear process at several different input pump powers.

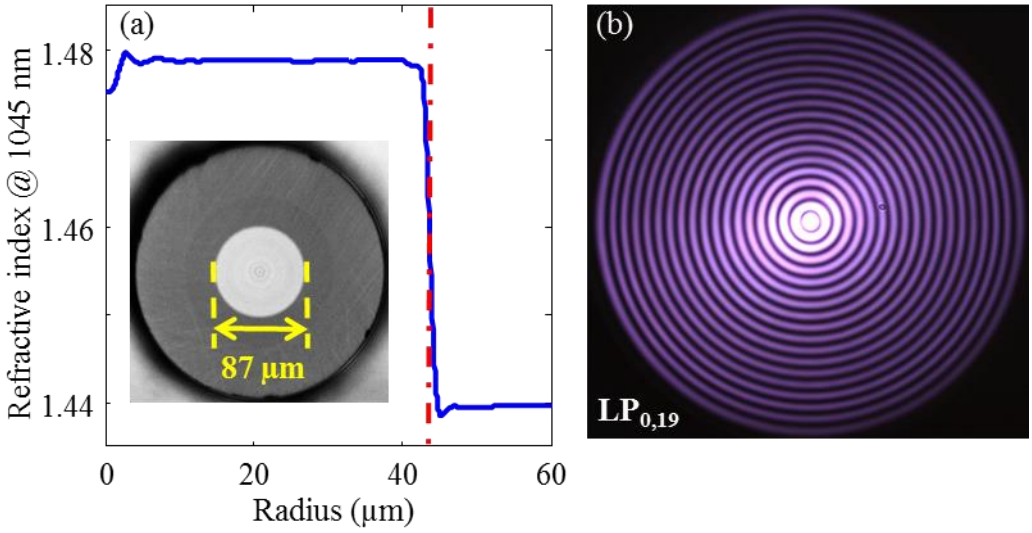

Figure 5.2: (a) The refractive index profile and cross-section of the step-index MMF used in the cutback experiment. Core diameter: 87 µm, NA: 0.34. (b) The recorded purely excited $LP_{0,19}$ mode.

In order to have a clear picture on the spectral evolution with fiber length. Before showing the process involving multiple modes, the interaction between only two modes are described in details. Figure 5.3(b) shows the intermodal interaction between $LP_{0,19}$ and $LP_{0,18}$ modes corresponding to input pump pulse energy of 28.2 nJ. At the beginning, along propagation the $LP_{0,19}$ mode (Fig. 5.3(c)) continuously shifts itself to longer wavelengths, behaving like a Raman soliton. When its wavelength becomes ~1150 nm, the energy starts transferring to a far separated longer wavelength (~1230 nm) spectral content. Afterwards, the wavelength shift of $LP_{0,19}$ mode nearly stops, and meantime the newly generated spectral content obtains more and more energy from it. Eventually, all the energy is

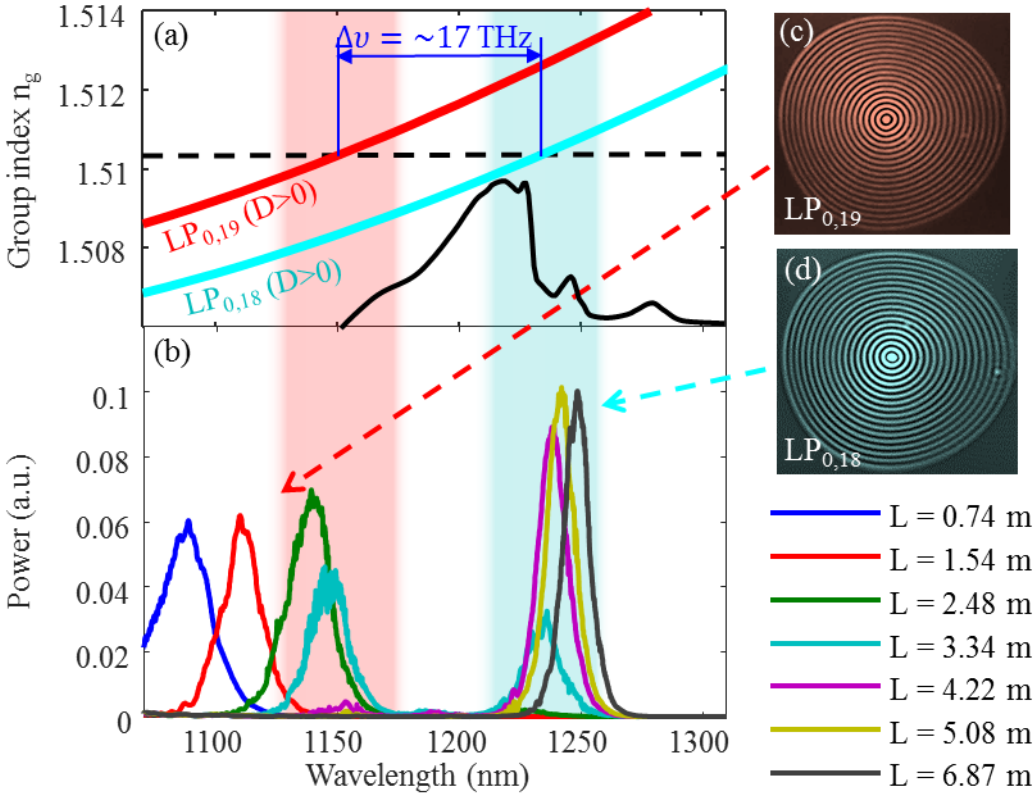

Figure 5.3: (a) The simulated group refractive indices of $LP_{0,19}$ (the red curve) and $LP_{0,18}$ (the cyan curve) modes and the normalized Raman gain (the black curve). (b) The detailed evolution during the $LP_{0,19}$-$LP_{0,18}$ intermodal interaction along the propagation, corresponding to input pump pulse energy of 28.2 nJ. (c) and (d) The recorded $LP_{0,19}$ and $LP_{0,18}$ mode images.

transferred to the new spectral peak, of which the mode is $LP_{0,18}$ (Fig. 5.3(d)). After becoming an independent spectral peak, the $LP_{0,18}$ mode starts shifting itself to long wavelengths, also behaving like a Raman soliton. Figure 5.3(a) gives the simulated group refractive index curves for $LP_{0,19}$ and $LP_{0,18}$ modes, and clearly shows that the group indices of these two modes are matched when the interaction happens. The frequency separation of ~17 THz falls into the relatively high Raman gain range. Therefore, this intermodal interaction behaves like SSMC.

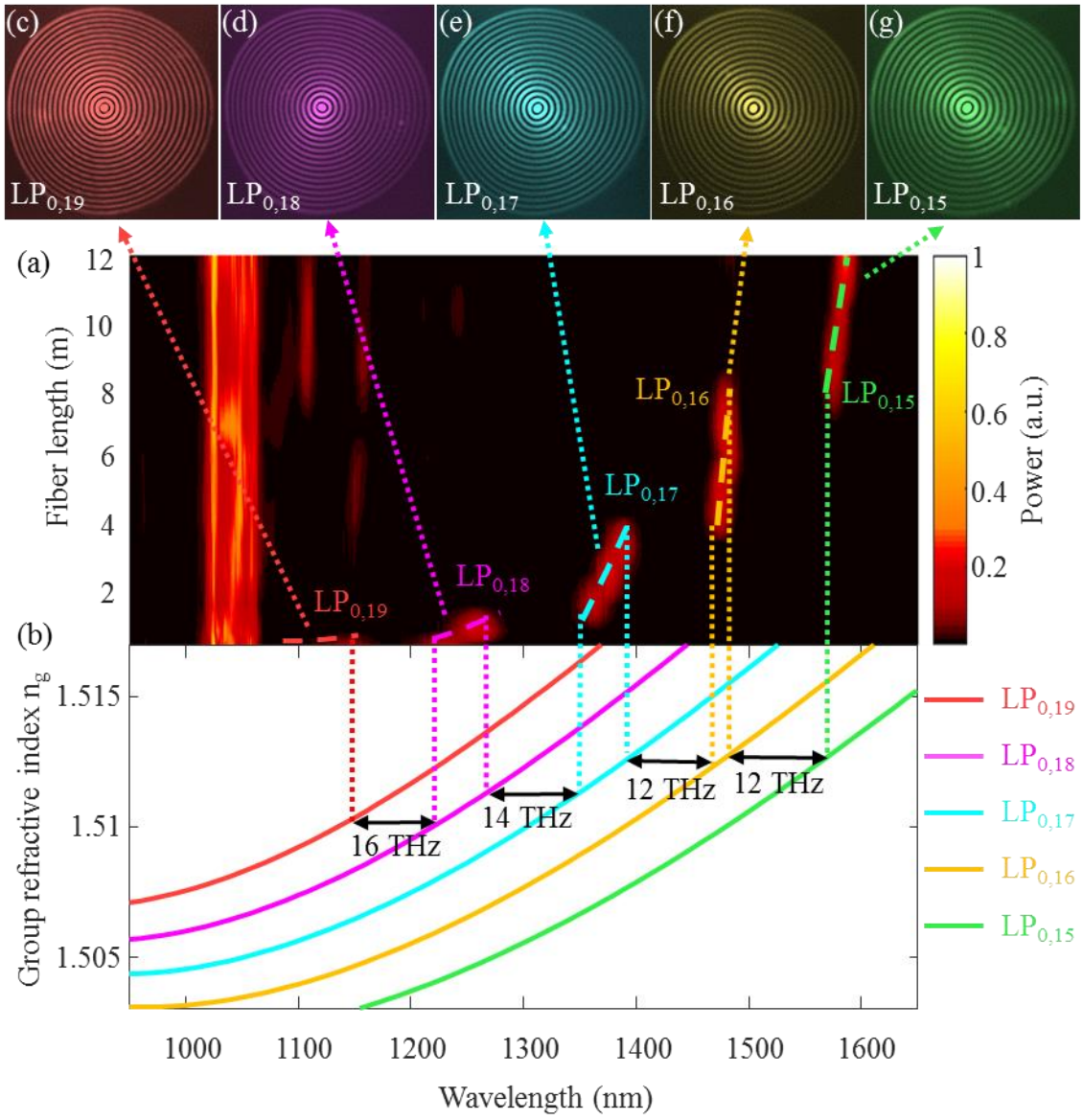

Figure 5.4: (a) The spectral evolution along fiber length when input pump pulse energy is 72.4 nJ. (b) The simulated group refractive indices of the modes involved in the entire wavelength conversion process in (a). (c)-(g) The recorded mode images for the spectral peaks in (a).

The full wavelength translation process involving multiple modes is shown in Fig. 5.4 (a), which corresponds to input pump pulse energy of 72.4 nJ. The spectral evolution consists of alternate occurrences of two features, i.e. continuous and discrete wavelength shifts, and

can be seen as the cascaded processes shown in Fig. 5.3(b). The intermodal interactions keep lowering the mode order, from $LP_{0,19}$ to $LP_{0,15}$ (Fig. 5.4(c)-(g)). For each pair of interacting modes, the group refractive indices are matched during the interaction, with the frequency separation close to 13 THz (Fig. 5.4(b)), i.e. within the high Raman gain region. At the propagation distance of 12 m, i.e. the original fiber length, an independent spectral peak in the $LP_{0,15}$ mode shows up at 1587 nm. Since the intensity overlap integral between two $LP_{0,m}$ modes is non-zero, and all the modes involved in the entire wavelength conversion process have anomalous dispersions, meaning they are able to form solitons, the multiple intermodal energy transfer processes shown in Fig. 5.4(a) are all potentially SSMC processes.

In order to confirm these intermodal interactions are indeed SSMC processes, it needs to be proved that all of the spectral peaks, when being independent, are solitons. This analysis can be done in spectral domain. The bandwidths of independent spectral peaks can be determined by Gaussian fitting the spectra, and the results are given in Fig. 5.5(b) (the solid blue dots). Figure 5.5(a) shows one spectral fitting example.

The pulse energy was measured on two independent spectral peaks (the $LP_{0,16}$ mode at 1479 nm and 6.87 m fiber length, and the $LP_{0,15}$ mode at 1586 nm and 12 m fiber length), and the results are 26.4 nJ and 27.2 nJ, respectively. Normally the energy should decrease with wavelength due to the photon-phonon interaction. In this experiment, the measured slight energy increase (3%) with wavelength should be due to measurement error, but at the same time it also indicates that both intermodal and intramodal energy transfers are very efficient, and thus it is reasonable to assume that during this entire wavelength

translation process, the number of photons is conserved, i.e. the loss only originates from

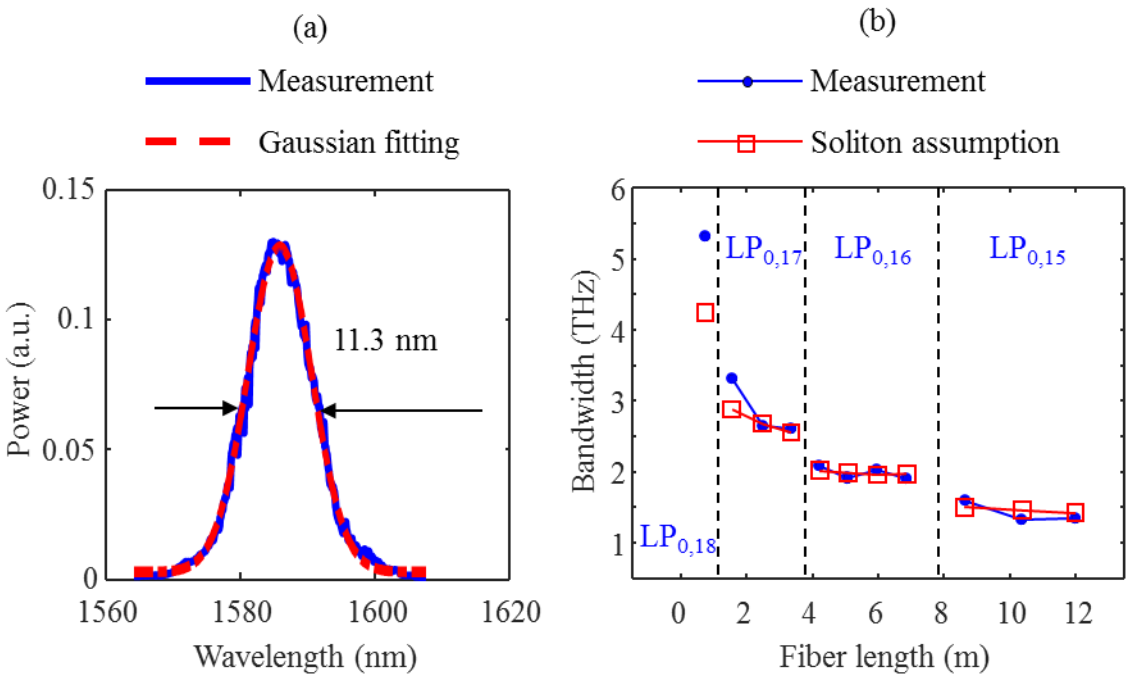

Figure 5.5: (a) The measured spectrum and the corresponding Gaussian fitting on the $LP_{0,15}$ mode at 1587 nm and 12 m fiber length. (b) The bandwidths of the independent spectral peaks. Solid dots: based on Gaussian fitting the measured spectra. Open squares: calculation based on the soliton assumption.

photon-phonon interaction. Based on this point, the pulse energy of all the independent spectral peaks can be calculated by using that of $LP_{0,15}$ mode at 12 m fiber length. Assuming that all the independent spectral peaks are indeed solitons, i.e. the soliton number is one and the time-bandwidth product is 0.315, then their spectral bandwidths $\triangle\upsilon$ can be calculated using the expression

$$\triangle\upsilon = 1.54\times10^{-14}\frac{\pi^2 n_2 c}{DA_{eff}\lambda^4} \tag{5.1}$$

where n_2 is the nonlinear-index coefficient, c is the speed of light in vacuum, λ is the

wavelength of an independent spectral peak, D and A_{eff} are the dispersion and effective mode area, respectively, corresponding to the mode and wavelength where the independent spectral peak stays. The derivation of Eq. (5.1) is based on Eqs. (2.9)-(2.10), (3.6)-(3.8), (3.10) and the relation $L_D = L_{NL}$. The calculated bandwidths are shown in Fig. 5.5(b) (the open red squares). The measured and calculated bandwidth results are close to each other, indicating the assumption that the independent spectral peaks are solitons is valid. From Fig. 5.5(b), it can be also seen the bandwidth decreases with fiber length. For Raman solitons, a smaller bandwidth means a slower wavelength shift, which is indeed observed in Fig. 5.4(a), again indicating the independent spectral peaks are solitons.

The confirmation of the independent spectral peaks being solitons can also be done in temporal domain. In the cutback experiment, the pulse duration on the $LP_{0,15}$ mode at 12 m fiber length was measured using auto-correlation (Fig. 5.6(a)). This data point is shown in Fig. 5.6(b) (the blue dot). Assuming the independent spectral peaks are solitons, i.e. the time-bandwidth product is 0.315, then their pulse durations can be calculated based on the spectral bandwidths obtained by Gaussian fitting. The calculation results are shown in Fig. 5.6(b) (the open red squares). The theoretically calculated result based on the soliton assumption agrees well with the measurement, which indicates the soliton assumption is valid.

Through the analyses above in both spectral and temporal domains, it is believed the independent spectral peaks are indeed solitons. Therefore, the intramodal and intermodal wavelength conversion processes involved in Fig. 5.4(a) are SSFS and SSMC, respectively. This entire process results from the cascaded SSMC effect.

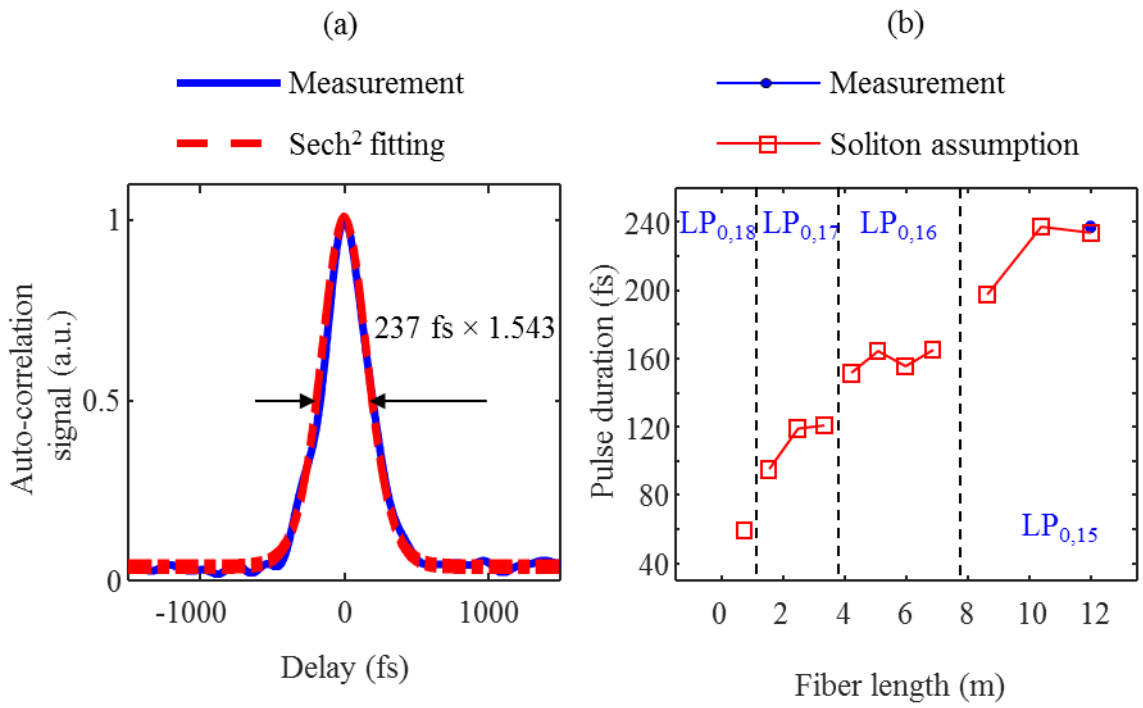

Figure 5.6: (a) The measured auto-correlation trace and the corresponding sech^2 fitting on the $LP_{0,15}$ mode at 1587 nm and 12 m fiber length. (b) The pulse durations of the independent spectral peaks. Solid dots: auto-correlation measurement. Open squares: calculation based on the soliton assumption.

The soliton pulse energies calculated based on the conservation of photon number, and the pump-to-soliton energy conversion efficiencies of different modes at different wavelengths and fiber lengths are shown in Fig. 5.7. During this entire wavelength conversion process, the conversion efficiency monotonically decreases with fiber length due to the loss to the material, with the efficiency of ~38% corresponding to the largest fiber length (12 m), indicating the entire wavelength conversion process is efficient.

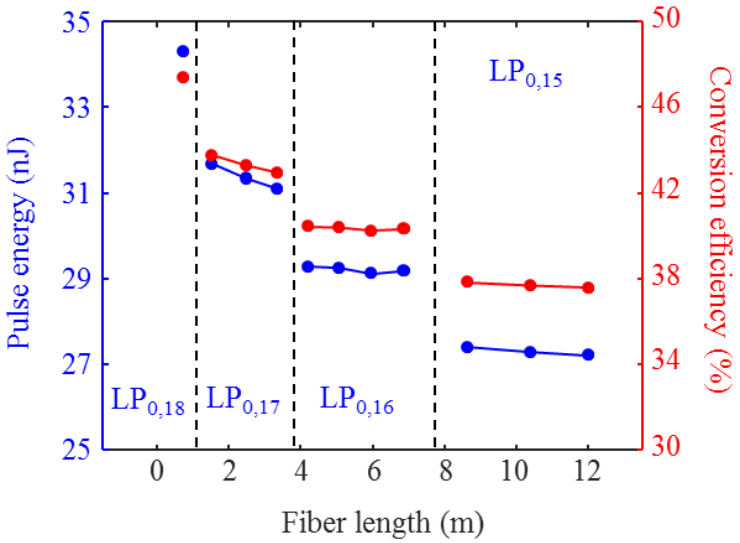

Figure 5.7: The soliton pulse energies and pump-to-soliton energy conversion efficiencies of different modes at different wavelengths and fiber lengths.

Figure 5.8 shows the soliton peak powers at different fiber lengths. The peak power monotonically decreases along fiber length, but at least stays at sub-MW level, which is much higher than that out of step-index single mode fibers (SMFs), indicating the effectiveness of using MMFs to generate strong pulses.

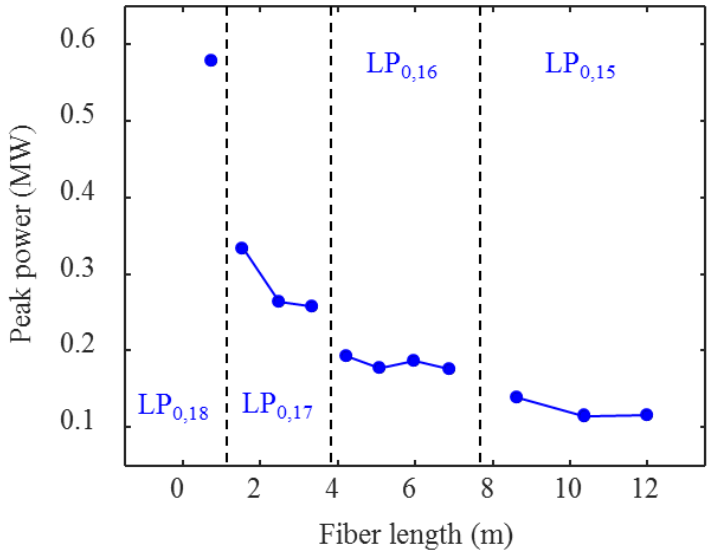

Figure 5.8: The soliton peak powers of different modes at different wavelengths and fiber lengths.

5.2 Cascaded SSMC as a function of input pump power

The experimental setup is the same as that shown in Fig. 5.1. In the experiment, the fiber length is fixed to 12 m, but the input pump power is tuned. The reasons for this experiment are that (1) it needs to be tested if the cascaded SSMC effect also occurs for a given fiber length but different input pump powers. (2) For any application which needs to tune the wavelength, pulse energy and peak power out of a fiber, it is a more practical way to adjust the input pump power than fiber length. The recorded spectral evolution with input pump power is shown in Fig. 5.9(a), which is similar to the cutback experimental result (Fig. 5.4(a)). The cascaded intermodal interactions keep lowering the mode order, from $LP_{0,19}$ to $LP_{0,14}$ (Fig. 5.9(c)). Note that the identification of $LP_{0,14}$ mode is from the speculation based on group refractive index matching (Fig. 5.9(b)) rather than the imaging measurement. Based on the group index matching during the intermodal interactions, with the frequency separation coinciding with high Raman gain region (Fig. 5.9(b)), and all involved modes possessing anomalous dispersion, the intermodal interactions showing up in the input pump power tuning experiment are speculated to be SSMC.

Unlike the intermodal interactions in the cutback experiment, where only $LP_{0,m}$ modes are involved, the intermodal interactions shown in Fig. 5.9 include $LP_{1,18}$. An explanation based on SSMC suppression is given here. In the cutback experiment, the input pump energy is fixed to a high level (72.4 nJ), forming a strong soliton in the $LP_{0,19}$ mode (>34 nJ). As will be briefly described in Sec. 5.3, a strong soliton suppresses the occurrence of SSMC. Before $LP_{0,19}$—$LP_{1,18}$ interaction happens, another stronger intermodal interaction, i.e. $LP_{0,19}$—$LP_{0,18}$ pair, wins over the $LP_{0,19}$—$LP_{1,18}$ interaction because of having a larger

intensity overlap, and takes place. In contrast, in the pump power tuning experiment, the pump energy starts with a low level, and the formed $LP_{0,19}$ soliton is weak (7.3 nJ), so the intermodal interaction between $LP_{0,19}$ and $LP_{1,18}$ can happen. However, due to the relatively low intensity overlap resulting from the different beam profile symmetries for the two modes, the energy transfer is slow. Before $LP_{1,18}$ obtains all the energy from $LP_{0,19}$ and becomes an independent spectral content, the interaction between it and $LP_{0,18}$ already occurs.

For each independent spectral peak, the bandwidth is acquired based on Gaussian fitting, and the pulse duration is measured using auto-correlation. Fig. 5.10 gives the calculated time-bandwidth product corresponding to those peaks v.s. their mode order (the blue dots). All the products are larger than but close to 0.315, i.e. the theoretical value for an ideal soliton pulse. This discrepancy might be because the pulses are broadened by the optical components before they are sent into the auto-correlator.

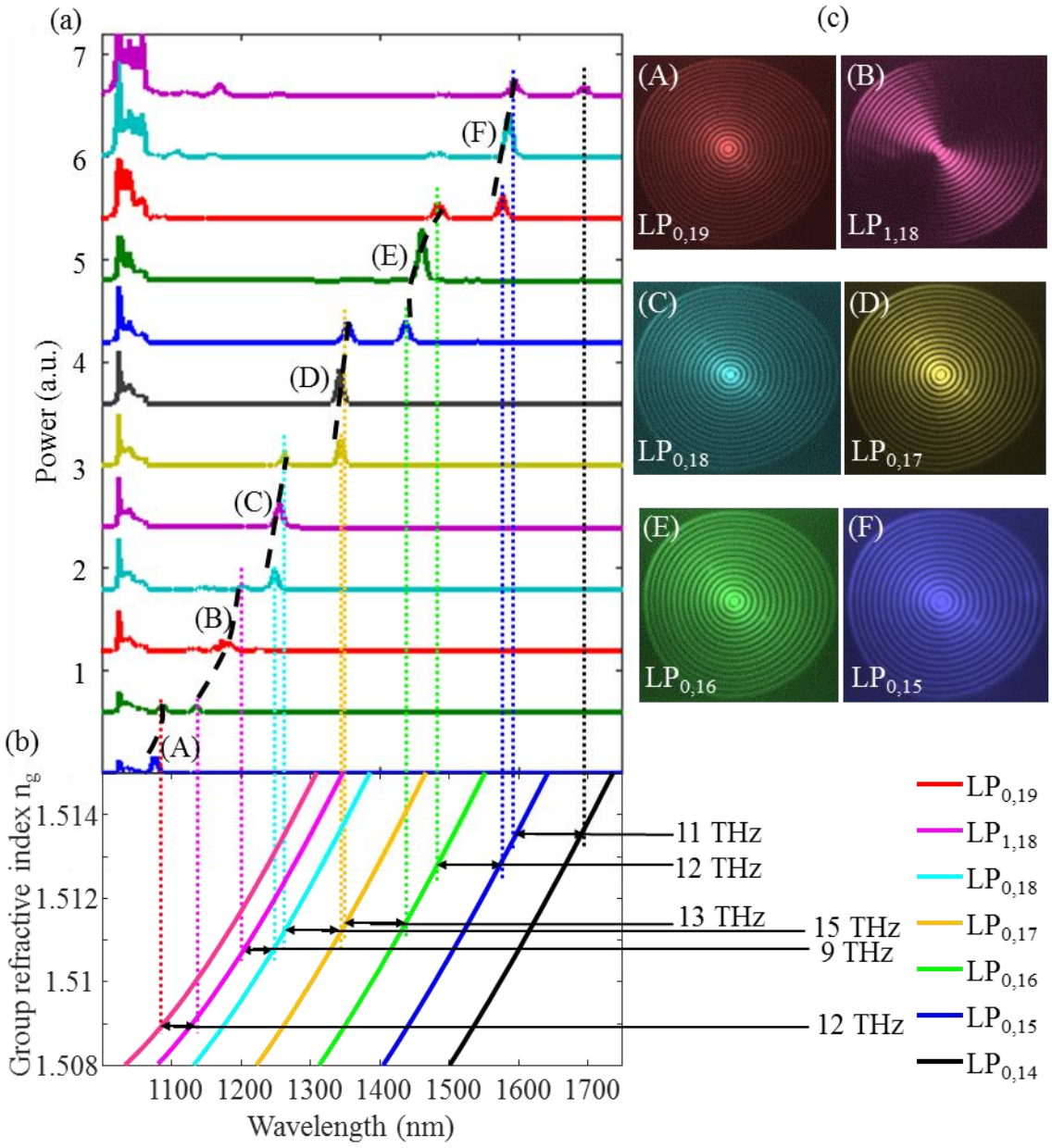

Figure 5.9: (a) The spectral evolution with input pump power. The corresponding input pump pulse energies from low to high are: 11 nJ, 12.9 nJ, 19.5 nJ, 22.4 nJ, 25.1 nJ, 26.3 nJ, 28.2 nJ, 32.4 nJ, 38.9 nJ, 52.5 nJ, 72.4 nJ, and 79.4 nJ. (b) The simulated group refractive indices of the modes involved in the entire wavelength conversion process in (a). (c) The recorded mode images for the labelled spectral peaks in (a).

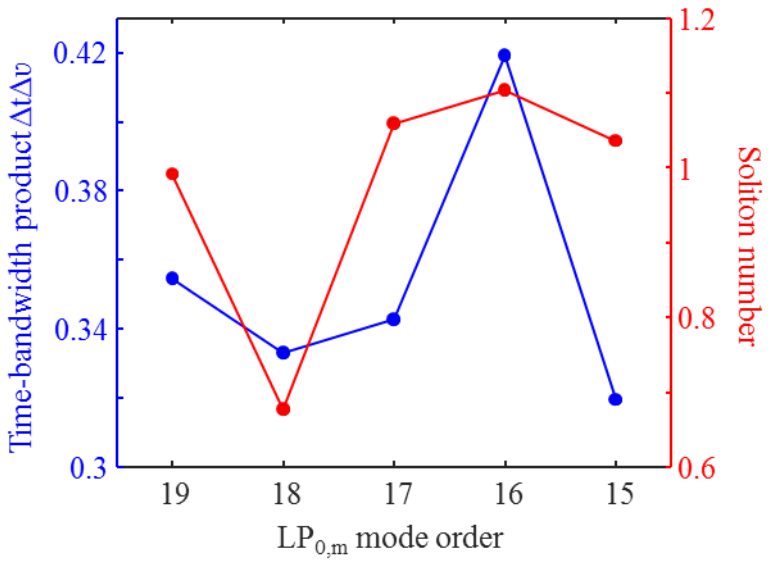

Figure 5.10: Blue dots: the time-bandwidth product, calculated based on measured spectral bandwidth and pulse duration, vs. mode order. Red dots: The calculated soliton number, based on measured pulse energy and duration, vs. mode order.

The soliton numbers for the independent spectral peaks are calculated using Eq. (3.14). The results are shown in Fig. 5.10 (the red dots). All the modes, except the $LP_{0,18}$, have the soliton number close to 1. It has not been figured out why the soliton number of pulses in the $LP_{0,18}$ mode is only 0.7. According to both time-bandwidth product and soliton number results, it is confirmed that all the independent spectral peaks are solitons except the one in $LP_{0,18}$ mode. Therefore, the entire wavelength conversion process shown in Fig. 5.9(a) mainly consists of SSFS and SSMC, based on which the wavelength shift as much as ~62% of the carrier wavelength (1045-1696 nm) is achieved. The further shift is currently limited by the pump power available in the lab, and ultimately limited by the self-action/dielectric breakdown effect that causes either beam profile perturbation or fiber damage. The details will be given in chapter 7.

Figure 5.11(a) shows the evolution of measured soliton pulse energy (the blue dots) and pump-to-soliton energy conversion efficiency (the red dots) with mode order, including the $LP_{0,18}$ mode. The soliton energy basically monotonically increases with decreasing mode order, which should be because more pump power needs to be launched into the fiber to shift the soliton wavelength farther either by SSFS or SSMC, and at the same time more energy is transferred into the solitons. This is the same as that in a pure SSFS process. Except the $LP_{0,18}$ mode, the pump-to-soliton energy conversion efficiency basically decreases with decreasing mode order, with the efficiency of ~38% for the lowest soliton mode order. This trend is partially due to (1) the higher input pump power, which corresponds to the lower mode order, forms a soliton of higher order at the fiber input end, resulting in lower conversion efficiency to the first constituent fundamental soliton, as seen from Eq. (3.10), (3.12)-(3.13); and (2) the lower mode order has a longer wavelength, and experiences a larger loss to the material during the photon-phonon interaction. The trend should be also related to the conversion efficiency from the pump to the higher order soliton at the beginning, but a good understanding on this aspect has not been obtained. The lowest conversion efficiency of ~30% unexpectedly happens to the $LP_{0,18}$ mode, the reason has not been figured out. For the entire spectral evolution with the input pump power tuning, the $\geq$ ~30% energy conversion efficiency indicates the process is efficient.

The peak powers on different mode orders, calculated based on the measured pulse energies and pulse durations, are shown in Fig. 5.11(b), which basically monotonically increase with mode order, and are higher than that out of step-index SMFs, again indicating the capability of MMFs to generate strong pulses.

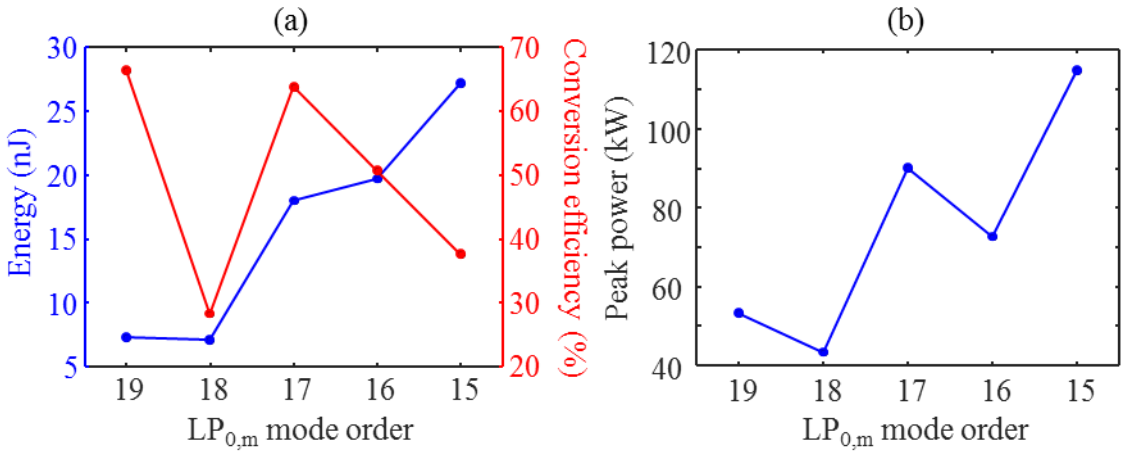

Figure 5.11: (a) The measured soliton pulse energy and pump-to-soliton conversion efficiency vs. mode order. (b) The soliton peak power, calculated based on the measured energy and pulse duration, vs. mode order.

5.3 Competition between SSFS and SSMC

SSMC is a process which starts with the spontaneous emission, competing against SSFS and eventually winning over it. The dynamics inside SSMC and the final states of SSMC product (the properties, such as wavelength and pulse energy, of the new spectral/modal content when the intermodal energy transfer is finished) are determined by the relative strength between SSFS and SSMC processes. This section describes simulation and experimental results showing the tuning of both competition and final SSMC product states.

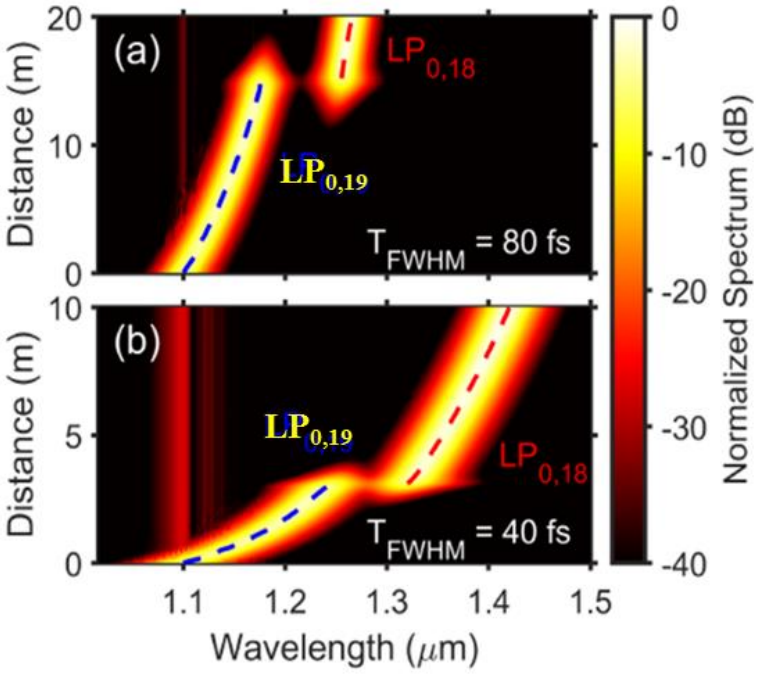

Figure 5.12: The SSMC simulation between $LP_{0,19}$ and $LP_{0,18}$ under two different input Raman soliton pulse durations (80 fs and 40 fs). The fiber used in the simulation is the same as that used in the cascaded SSMC experiments (Sec. 5.1 & 5.2). (Data courtesy of Aku Antikainen and Professor Govind P. Agrawal)

The change in the competition between SSFS and SSMC can be characterized by the change in Raman soliton wavelength at the onset of SSMC. When SSFS becomes more competitive, i.e. the Raman soliton has a shorter pulse duration (or larger bandwidth) to shift its wavelength faster per unit fiber length (Gordon, 1986), it tends to suppress SSMC, and ends up having a longer Raman soliton wavelength at the onset of SSMC. Figure 5.12 shows the simulated SSMC processes between $LP_{0,19}$ and $LP_{0,18}$ modes under two different input Raman soliton pulse durations. The fiber used in the simulation is the same as that used in the cascaded SSMC experiments (Sec. 5.1 & 5.2). The simulation is based on the multimode generalized nonlinear Schrödinger equation (GNLSE) (Poletti and Horak, 2008), and implemented by Aku Antikainen from Professor Govind P. Agrawal's group at

University of Rochester. The simulation clearly shows that when the input $LP_{0,19}$ Raman soliton pulse duration becomes shorter (from 80 fs to 40 fs), i.e. more competitive, the occurrence of SSMC is suppressed, and the Raman soliton wavelength becomes larger at the onset of SSMC (from ~1180 nm to ~1240 nm).

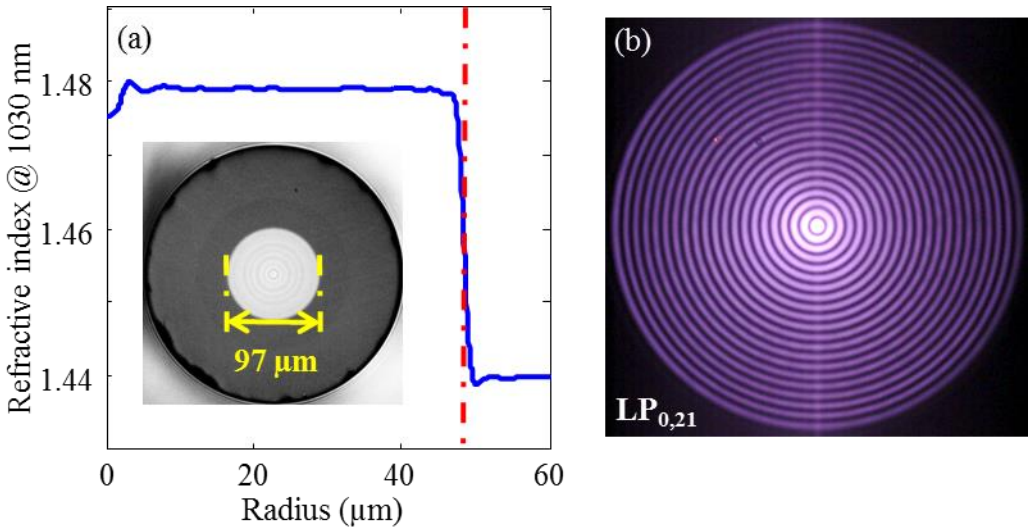

Figure 5.13: (a) The refractive index profile and cross-section of the step-index MMF used in the competition experiment. Core diameter: 97 µm, NA: 0.34. (b) The recorded purely excited $LP_{0,21}$ mode.

The tuning of competition between SSFS and SSMC can be observed in experiments. When SSMC just starts at the fiber output, the nonlinear process inside the fiber is governed nearly only by SSFS. Therefore, the competitiveness or the pulse duration of a Raman soliton can be influenced by simply changing the fiber length. A cutback experiment is implemented to observe the tuned competitiveness of SSFS against SSMC. The experimental setup is the same as that shown in Fig. 5.1, except that a different pump laser is used in this experiment, of which the center wavelength and pulse duration are ~1030 nm and ~370 fs, respectively. The step-index MMF for this measurement has a core dimeter

of 97 μm and NA of 0.34 (Fig. 5.13(a)), the launching mode is $LP_{0,21}$ (Fig. 5.13(b)), and the SSMC happens between $LP_{0,21}$ and $LP_{0,20}$. The original fiber length is 5 m.

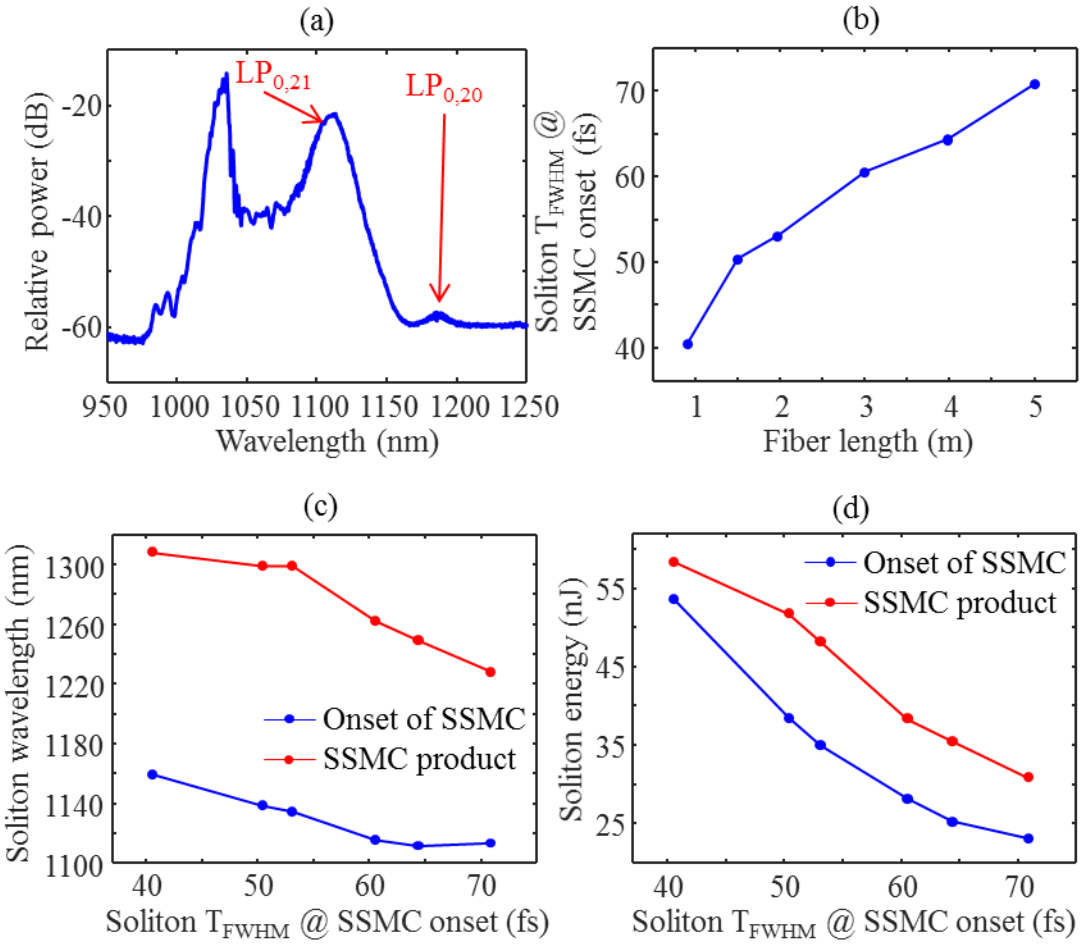

Figure 5.14: (a) The spectrum at the onset of SSMC for the 5 m fiber length. (b) The $LP_{0,21}$ Raman soliton pulse duration at the onset of SSMC versus fiber length. (c) The $LP_{0,21}$ Raman soliton wavelength at the onset of SSMC and the final SSMC product wavelength versus $LP_{0,21}$ Raman soliton pulse duration at the onset of SSMC. (d) The $LP_{0,21}$ Raman soliton pulse energy at the onset of SSMC and the final SSMC product pulse energy versus $LP_{0,21}$ Raman soliton pulse duration at the onset of SSMC.

The SSFS spectrum at the onset of SSMC for the 5 m fiber length is shown in Fig. 5.14(a). The small spectral bump is in the $LP_{0,20}$ mode, which is ~40 dB lower than the $LP_{0,21}$ Raman soliton. The pulse duration of the Raman soliton ($LP_{0,21}$) at the onset of SSMC is calculated

based on the measured pulse energy, wavelength and the relation $L_D = L_{NL}$. Figure 5.14(b) shows the pulse duration with fiber length. When the fiber length becomes longer, the pulse duration becomes larger, indicating the SSFS becomes less competitive. At the onset of SSMC, the evolutions of $LP_{0,21}$ Raman soliton wavelength and pulse energy with the Raman soliton pulse duration are given in Fig. 5.14(c) and (d) (blue traces). The wavelength and the corresponding energy clearly decrease with the pulse duration, showing the weakened competitiveness of SSFS against SSMC. The final wavelength and energy of SSMC product are also given in Fig. 5.14(c) and (d) (the red traces). The change in both of them shows the tuning of SSMC product properties.

5.4 Summary

This chapter has mainly described the cascaded SSMC process, and briefly presented the competition between SSFS and SSMC. The salient results are listed below.

(1) Both long fiber lengths and higher input pump powers can facilitate the occurrence of cascaded SSMC.

(2) In the cascaded SSMC process, for each pair interacting modes, when the energy transfer happens, the group refractive index matching, frequency separation of ~13 THz, i.e. coinciding with the high Raman gain region, and the relatively high intensity overlap integral are necessary factors for the intermodal energy transfer to happen efficiently. These requirements are generally satisfied in the interaction between two $LP_{0,m}$ modes. However, for the $LP_{0,m}$—$LP_{1,n}$ interaction, due to the different beam profile symmetries, the intensity overlap integral is relatively low, resulting in inefficient energy transfer.

(3) The wavelength shift as much as ~62% of the carrier wavelength (1045-1696 nm) has been achieved, which is currently limited by the pump power available in our lab. Ultimately the limit originates from self-action/dielectric breakdown effect that causes either beam profile perturbation or fiber damage.

(4) In the SSFS and SSMC processes described in this chapter (Sec. 5.1 & 5.2), the number of photons are (nearly) conserved, meaning the two processes are efficient.

(5) The pump-to-soliton energy conversion efficiency is fundamentally limited by the loss to the material through photon-phonon interaction, and the fact that the higher order soliton formed at the fiber input end only gives partial energy to the first constituent fundamental soliton, and the higher the soliton order, the lower the conversion efficiency. The energy conversion efficiency is also related to the conversion efficiency from pump to the higher order soliton at the fiber input end, of which the process has not been understood well. In the wavelength conversion experiments described in this chapter (Sec. 5.1 & 5.2), the minimum pump-to-soliton energy conversion efficiency is ~30%, corresponding to the $LP_{0,18}$ mode in the pump power tuning experiment. Although the behavior on this mode has not been fully understood, e.g. the soliton number is only ~0.7, the $\geq$ ~30% efficiency indicates the wavelength conversion process based on cascaded SSMC is efficient.

(6) The temporally aligned, but spectrally separated pulses generated by SSMC can be useful for the applications which need the synchronized sources. The wideband wavelength conversion can satisfy the needs of multiple microscopy applications.

(7) The competition between SSFS and SSMC has been shown in both simulation and experiments. It has been shown that the SSMC product can be tuned by changing the fiber length.

Chapter 6

Compact Source for CARS/SRS

Coherent anti-Stokes Raman scattering (CARS) (Duncan et al., 1982; Zumbusch et al., 1999; Zhang and Cheng, 2018) and stimulated Raman scattering (SRS) (Ploetz et al., 2007; Freudiger et al., 2008; Zhang and Cheng, 2018) microscopy techniques allow the identification of chemical content in biological samples. Dual color femtosecond (fs) sources are important for implementing hyperspectral CARS/SRS. Nowadays, one main source is the commercial solid-state optical parametric oscillator (OPO) (Insight X3, Spectra Physics, USA), in which one output beam is at 1045 nm with peak power of > ~0.2 MW, and the other beam is tunable between 680 nm and 1300 nm, with peak power of > ~0.2 MW. As mentioned in chapter 1, in contrast to solid-state sources, fiber-based sources are lightweight, alignment-free, cost-effective, and able to deliver high quality beams (either perfect Gaussian or a pure higher order mode (HOM)). In our lab it has been demonstrated that using HOMs soliton self-frequency shift (SSFS) and soliton self-mode conversion (SSMC) can be used to generate strong pulses with peak powers of sub-MW or even 1.1 MW at ~1300 nm (Rishoj et al., 2018). This nonlinear output, and the remaining light from the pump laser—a commercial, alignment-free fiber laser, can act as the Stokes and pump arms respectively to form a dual color fs source, with peak powers of at least sub-MW from both arms, which is comparable to or higher than the commercial source, thus improving the detection sensitivity. In addition, the repetition rate of the pump laser in our lab is at most 10 MHz, which is ~10 times lower than that of Insight X3, which

allows the use of high peak power illumination without damaging the bio-samples. This chapter describes the buildup of a compact dual color source for CARS/SRS, which uses commercially available physical axicons to achieve mode conversion on both input and output sides of the fiber in the Stokes arm. This project is in the collaboration with Professor Ji-Xin Cheng, aiming to image the C−D and C≡C bonds, which have the Raman response peaks within the ~2100-2300 cm^{-1} range (Wei et al., 2017). Since the center wavelength of the pump arm (from the commercial fiber laser) is ~1045 nm, the wavelength range of the Stokes arm is 1339-1376 nm. The organization of this chapter is as follows. The nonlinear characterization, using the spatial light modulator (SLM) setup to excite HOMs, to confirm the selected fiber and mode can generate strong pulses across the required wavelength range, is described first. In the 2^{nd} section, the mode conversion with the commercially available physical axicons is presented, where the optimization processes for both HOM excitation and HOM-to-Gaussian conversion are shown. Finally, the dual color source characterization results are given.

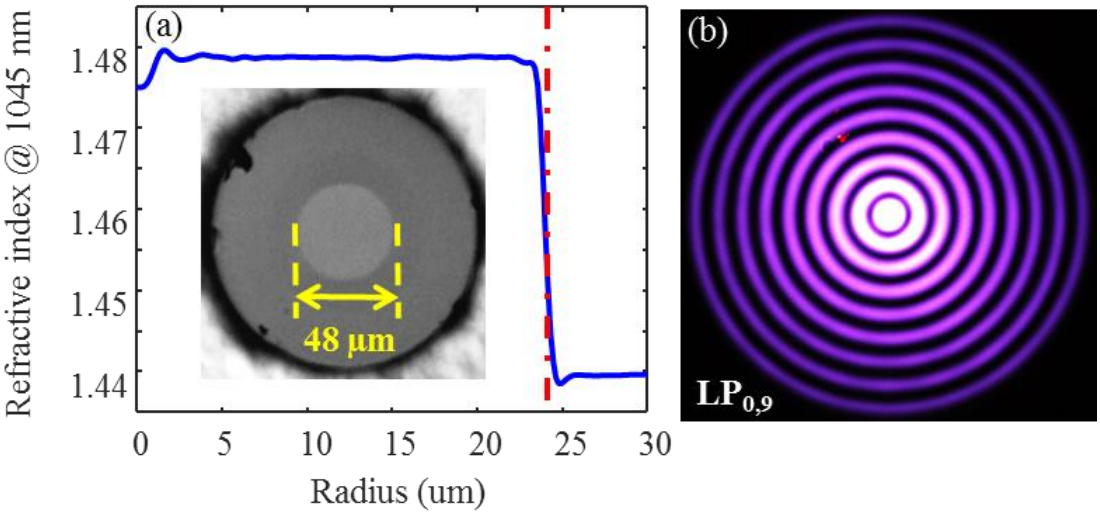

Figure 6.1: (a) The refractive index profile at pump wavelength (1045 nm), and cross-section of the step-index MMF. Core diameter: 48 μm, NA: 0.34. (b) The recorded pure excitation of $LP_{0,9}$ mode.

6.1 SSFS characterization using SLM setup

The fiber used to build up the compact source has a core diameter of 48 μm and numerical aperture (NA) of 0.34 (Fig. 6.1(a)). The target launching mode is $LP_{0,9}$ of which the pure excitation of using the SLM setup is shown in Fig. 6.1(b).

The nonlinear effect used to build up the source is SSFS. The experimental setup is the same as that shown in Fig. 5.1. Figure 6.2(a) gives three typical spectra, showing that with increasing input pump pulse energy, the Raman soliton scans through the required wavelength range, i.e. 1339-1376 nm. Figure 6.2(b) gives the pulse energy and peak power corresponding to the three Raman solitons in Fig. 6.2(a). Across the wavelength window of interest, the pulse energy is ~20 nJ, and the peak power is ~0.32 MW, which are comparable to those of the wavelength-tunable arm from the commercial OPO.

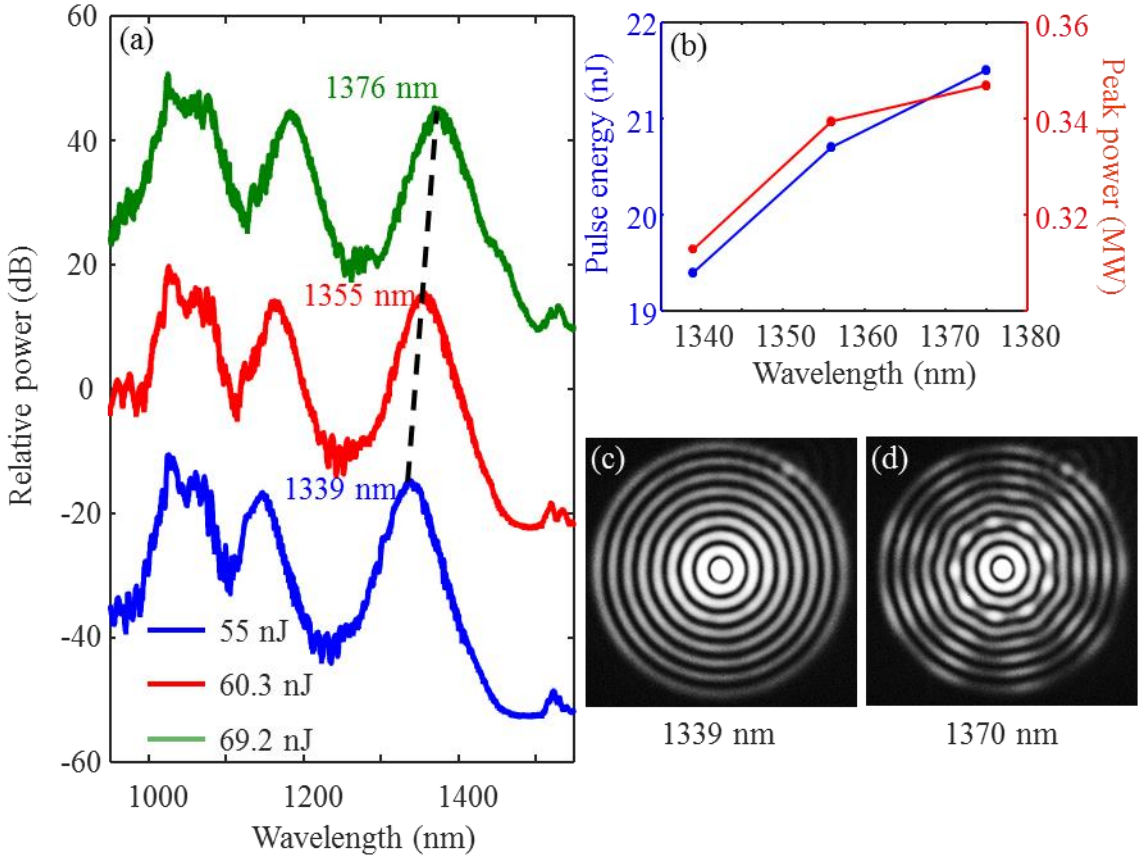

Figure 6.2: (a) Typical SSFS spectra showing the $LP_{0,9}$ soliton can cover the required wavelength range (1339-1376 nm). The input pump pulse energies corresponding to the three spectra are 55 nJ, 60.3 nJ, and 69.2 nJ, respectively. (b) The pulse energy and peak power corresponding to the Raman soliton in (a). (c) The mode images corresponding to Raman soliton at two different wavelengths, i.e. 1339 nm and 1370 nm. The azimuthal pattern clearly shows up.

However, there is a problem with the $LP_{0,9}$ mode. Around 1370 nm, its effective refractive index crosses with those of higher azimuthal order modes, resulting in the intermodal coupling and impure output mode image. The mode images corresponding to the Raman soliton at 1339 nm and 1370 nm are shown in Fig. 6.2(c) and (d) for comparison. The strong azimuthal pattern in the 1370 nm soliton image clearly shows up. This impure output mode might affect HOM-to-Gaussian conversion efficiency. More importantly, it might be

converted into a non-Gaussian-shaped beam, degrading the focus quality in the subsequent CARS/SRS microscopy experiment. Whether this impure mode is a problem or how serious this problem is will be discussed later based on the HOM-to-Gaussian conversion results.

6.2 Axicon-based mode conversion

6.2.1 Mode excitation

The mode excitation based on SLM setup is relatively easy, because one can basically add arbitrary phase profiles on the SLM to correct the phase distortion to some extent to improve the mode purity. For example, in our experiment a lens phase profile is generally needed to purely excite a specific HOM. The speculation on this need is that the mode excitation setup introduces aberration, which needs to be compensated by the lens phase profile. It is learned from chapter 4 that to excite a specific mode, essentially one just needs to image a spatially phase modulated beam onto the input fiber facet, and then the target mode can be selectively excited based on the field similarity. Therefore, in the SLM-based HOM excitation setup, the imaging system can be built without caring too much about the aberrations, which can be eventually corrected using the SLM. The experience tells us that without doing real-time, accurate mode purity measurements, a specific HOM can be purely excited using the SLM setup, with mode excitation quality close to the theoretical simulation, including both multipath interference (MPI) and loss.

The mode excitation with the physical axicon is harder than SLM, because the phase profile is fixed, i.e. no tunable phase can be used to easily correct aberrations in the system.

In the experiments, different lenses and the different distances between the lenses and axicon have to be tried to get a pure mode excitation. During this process, a real-time monitoring on the mode purity is necessary for judging if the mode purity becomes better or worse, i.e. if the optimization is toward correct or incorrect direction, and speeding up the optimization process.

Sub-second mode content measurement has been demonstrated (Demas and Ramachandran, 2014). However, this technique needs to use a wavelength tunable narrowband source, so it cannot be applied to the wideband, femtosecond source. Instead, the SSFS output properties can be directly used as the feedback to reflect the mode purity. For example, the Raman soliton wavelength is related to how much power is launched into the target mode, so it can be used to estimate MPI. The detailed procedure on this MPI measurement method is given below.

(1) It is known that the SLM setup can achieve the HOM excitation quality close to the simulation even without the assistance of real-time mode purity measurement. Also, in the SLM-based $LP_{0,9}$ SSFS characterization experiment, the coupling loss of mode excitation is measured to be 1.7 dB, which is only 0.2 dB higher than the simulation (1.5 dB loss in simulation). This additional loss should be from the input and output lenses (the lenses right before and after the fiber in Fig. 5.1). Therefore, it is believed the mode purity in the experiment is the same as or very close to the simulation, i.e. -12.7 dB.

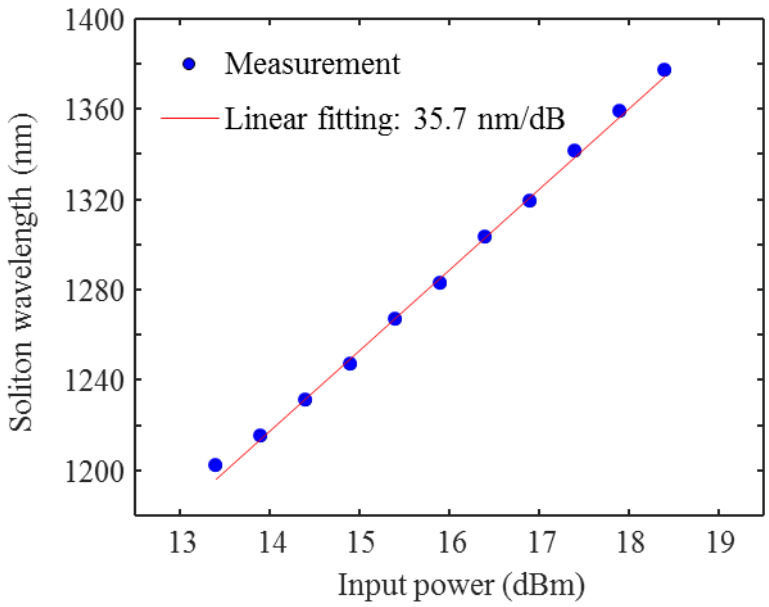

Figure 6.3: The measured Raman soliton wavelength versus input power (the blue dots), and the linear fitting (the red line).

(2) In the SLM setup the Raman soliton wavelengths at different input pump powers are measured (the blue dots in Fig. 6.3). The soliton wavelength basically changes linearly with the input power. The functional relation between them can be found by doing the linear fitting (the red line in Fig. 6.3). The slope of the fitting is 35.7 nm/dB.

(3) When characterizing the $LP_{0,9}$ SSFS using the SLM setup, the input power of 17.1 dBm generates the Raman soliton at 1330 nm. This input power and soliton wavelength are used as the reference for axicon-based HOM excitation optimization.

(4) When using the physical axicon to do HOM excitation, the reference input power, i.e. 17.1 dBm, is launched into the fiber, and then the soliton wavelength is measured. The difference between the measured wavelength and reference wavelength (i.e. 1330 nm) reflects the mode purity. Simply speaking, if the measured wavelength is larger the reference, it means the mode purity in the axicon setup is better than SLM setup, i.e. the

MPI is lower than -12.7 dB. If the measured wavelength is smaller than the reference, the MPI in the axicon setup is then higher than -12.7 dB. The exact MPI can be calculated using the expression

$$\text{sum MPI} = 10 \cdot \log_{10} \frac{1 - 10^{\left(\frac{\lambda_{meas} - \lambda_{ref}}{10 \cdot slope}\right)} + 10^{\left(\frac{MPI_{SLM}}{10}\right)}}{10^{\left(\frac{\lambda_{meas} - \lambda_{ref}}{10 \cdot slope}\right)}} \tag{6.1}$$

where λ_{meas} is the measured wavelength, λ_{ref} is the reference wavelength. Therefore, the MPI in the axicon HOM excitation setup can be quickly obtained by just measuring the soliton wavelength. According to Sec. 4.2, in the axicon setup the MPI can keep becoming smaller at the expense of conversion efficiency, so the target MPI in the axicon-based HOM excitation optimization is set to be equal to the minimal MPI in the SLM setup, i.e. -12.7 dB. The corresponding simulated coupling loss is 0.4 dB.

The axicon-based SSFS setup is shown in Fig. 6.4. On the fiber input side, four lenses (L_1—L_4) and one axicon with a base angle of 2° (AX252-C, Thorlabs, USA) are used to excite the target mode. Lens L_1 and L_2 are in cage I, and the axicon, lens L_3 and L_4 are in cage II. Different lenses are tried for L_1 and L_2, and the axial positions of the lenses and axicon are tuned to optimize the mode purity and coupling loss. Based on the data collected on different lenses L_1 and L_2, there are seemingly two general rules which are shown below. Note that the results below are the data corresponding to $f_{L_1} = 150\,\text{mm}$, and $f_{L_2} = 60\,\text{mm}$ (f is focal length).

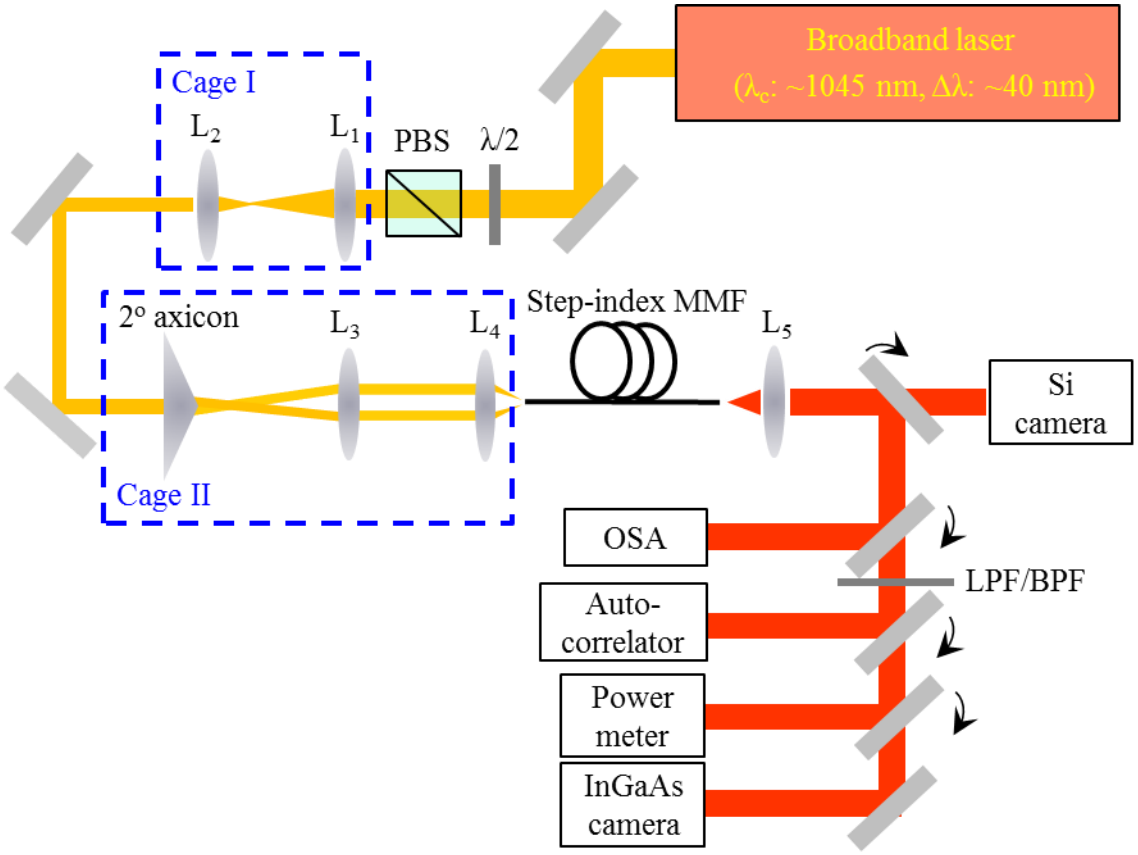

Figure 6.4: The axicon-based SSFS setup.

(1) Influence of lens L_2 position on MPI and loss

In this measurement, for each lens L_2 position, the positions of lens L_3 and the axicon are adjusted to get the minimal MPI, and then the coupling loss is measured. The influence of L_2 position on MPI and loss is shown in Fig. 6.5. In the figure, L_2 position is represented by the distance between lens L_1 and L_2. As seen from the figure, when L_2 gets farther away from L_1, sum MPI increases but loss decreases. It has not been figured out why the system behaves like this.

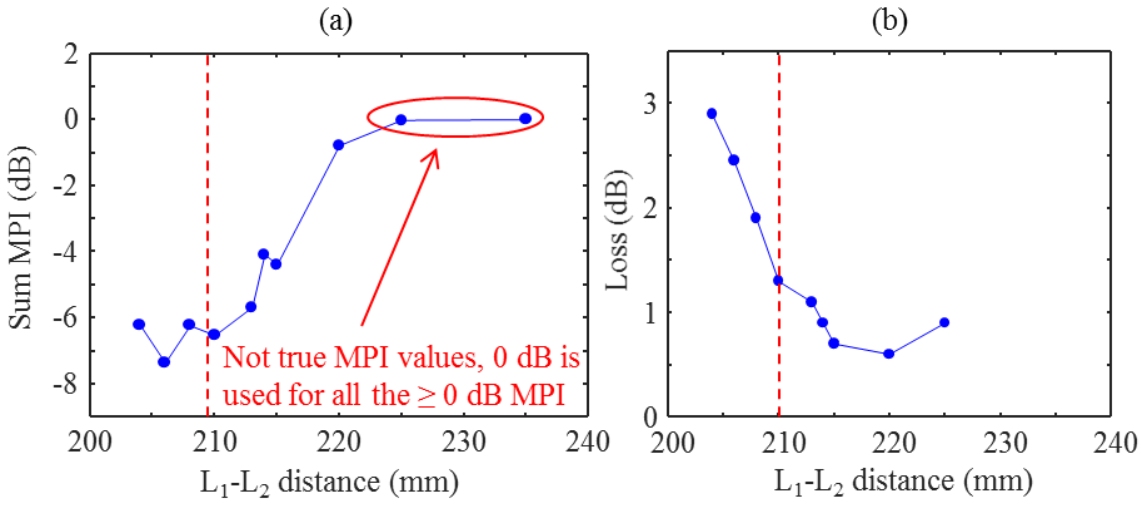

Figure 6.5: The influence of lens L_2 position on (a) sum MPI and (b) coupling loss. The red dashed line corresponds to the situation where the L_1-L_2 distance is equal the sum of their focal lengths, i.e. they form a telescope.

(2) Influence of (L_1, L_2) telescope position on MPI and loss

In this measurement, the distance between lens L_1 and L_2 is fixed to the sum of their focal lengths, i.e. 210 mm, to form a telescope, and only the (L_1, L_2) telescope position is changed. The influence of telescope position on MPI and loss is given in Fig. 6.6. The position is represented by the distance between lens L_2 and the axicon. The figures clearly show that the telescope position nearly does not change the MPI and loss, even when the telescope is moved by more than 10 cm. The calculation shows that during this measurement, the axicon always stays in the Rayleigh range of the (L_1, L_2) telescope output beam, so the conclusion is that the changes in both beam size and phase curvature, within the Rayleigh range of the beam hitting on the axicon, barely affect the MPI and loss in axicon-based HOM excitation.

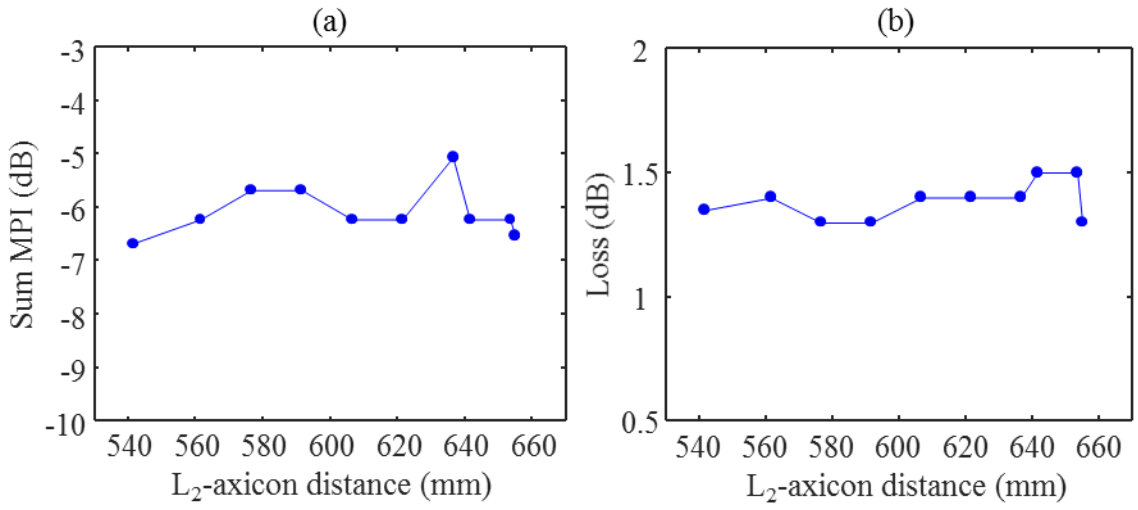

Figure 6.6: The influence of telescope (L_1, L_2) position on (a) sum MPI and (b) coupling loss.

The $LP_{0,9}$ mode image corresponding to the ultimately optimized mode excitation is shown in Fig. 6.7(a). The corresponding SSFS spectrum with the reference input power (17.1 dBm) is given in Fig. 6.7(b) (the blue trace), and compared with the reference spectrum (the red trace). The loss is only 0.8 dB, which is slightly higher than the target (0.4 dB), but the mode purity is not as good as that in the SML setup. The Raman soliton wavelength is only 1303 nm, smaller than the reference (1330 nm). The calculated MPI is only -6 dB. The reason might be that the lenses used in the setup cannot sufficiently correct the aberration.

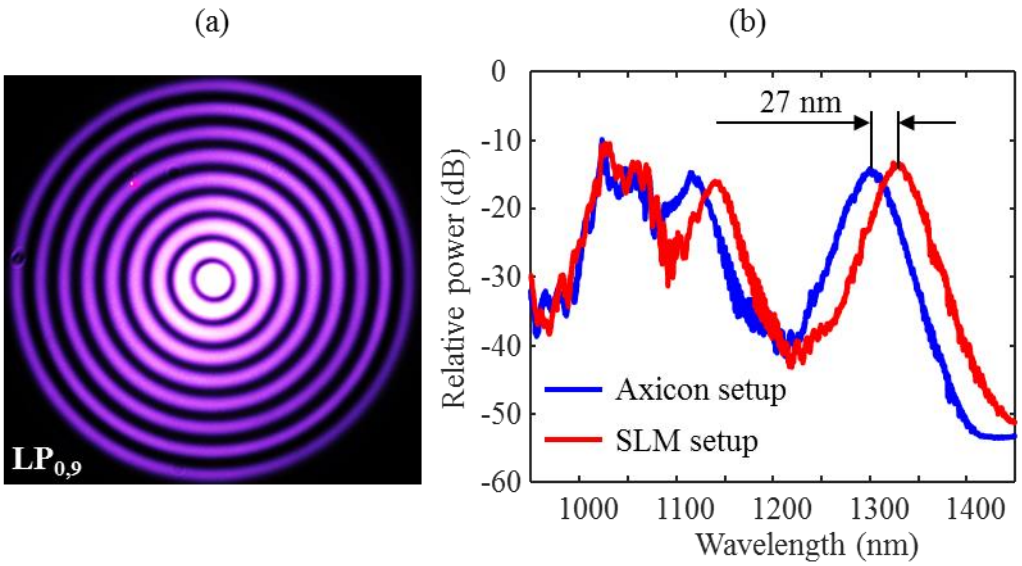

Figure 6.7: The performance of the ultimately optimized axicon-based mode excitation. (a) The excited $LP_{0,9}$ mode image recorded at the low power. (b) The comparison of SSFS spectra, with the reference input power, i.e. 17.1 dBm, in the axicon setup (the blue trace) and SLM setup (the red trace).

The information on the instruments/components in the ultimately optimized axicon HOM excitation setup are summarized in the table below.

Table 6.1: Summary of the instruments/components in the ultimately optimized axicon HOM excitation setup.

Instrument /Component	Focal length/Base angle	Coating	Distance	
Y-Fi			74cm	
L_1	150mm	B		19cm
L_2	40mm	C	52cm	
Axicon	2°	C		15.5cm
L_3	100mm	B	8cm	
L_4	8mm	B		

The impact of this relatively high MPI is lowering the pump-to-soliton energy conversion efficiency. If the coupling losses in the two HOM excitation setups, i.e. SLM and axicon

setups, are the same, the ratio of conversion efficiency in the axicon setup (η_{ax}) to that in the SLM setup (η_{SLM}) can be expressed as

$$\frac{\eta_{ax}}{\eta_{SLM}} = \frac{1+10^{\frac{MPI_{SLM}}{10}}}{1+10^{\frac{MPI_{ax}}{10}}} \tag{6.2}$$

where MPI_{SLM} and MPI_{SLM} are the sum MPIs. The η_{ax} can then be either theoretically predicted using η_{SLM} and Eq. (6.2), or directly measured. The results based on these two methods are compared in Fig. 6.8. The measured efficiency is close to the theoretical prediction, indicating the axicon setup just redistribute the power ratio between the target mode and parasitic modes, with additional loss barely introduced.

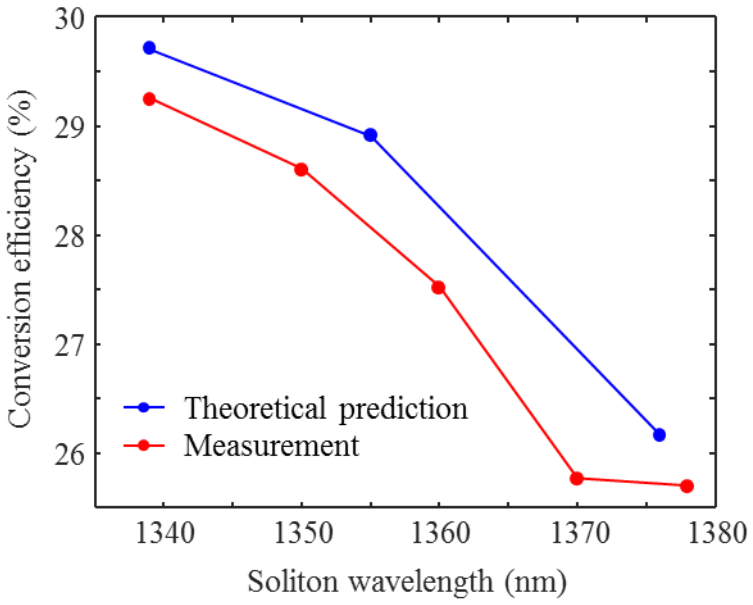

Figure 6.8: The comparison between theoretically predicted and measured pump-to-soliton conversion efficiencies in the axicon HOM excitation setup.

6.2.2 HOM-to-Gaussian conversion

It is described in Sec. 4.2 that axicons can convert a Gaussian beam into a Bessel-Gaussian beam in the focal plane. Since axicons are reciprocal devices, they should be also able to convert a Bessel-Gaussian in the focal plane back to a Gaussian beam. For the $LP_{0,m}$ modes in optical fibers, most of the power is contained in the core, where the electric field follows the zeroth order Bessel functions of the first kind, so they are more like Bessel beams instead of Bessel-Gaussian beams. Therefore, the axicon cannot purely convert an $LP_{0,m}$ mode to a Gaussian beam. Instead, in the far field of the axicon, a beam, which consists of a strong central Gaussian-like spot surrounded by weak rings, is form.

The HOM-to-Gaussian conversion setup is shown in Fig. 6.9(a), which basically uses the axicon mode excitation setup in the opposite way. The axicon, lenses L_6 and L_7 are in cage III. The base angle of the axicon is 1° (AX251-C, Thorlabs, USA). The output $LP_{0,9}$ Raman soliton from the fiber is spectrally isolated by the long-pass filter (LPF), and then imaged in the focal plane of the axicon. The lens L_6 is the Fourier transform lens, which is used to obtain the far field of the axicon output. The lenses L_7 magnifies this far field so that it can be resolved by the Indium gallium Arsenide (InGaAs) camera. The pinhole after lens L_7 is used to isolate the central Gaussian-like spot. The beams before and after the pinhole are shown in Fig. 6.9(a) for comparison. Before the pinhole, the first ring surrounding the central spot can be clearly seen.

The key factor to achieve low loss HOM-to-Gaussian conversion is matching the spatial frequency of the $LP_{0,9}$ mode image in the axicon focal plane to that of the axicon. For a physical axicon, the spatial frequency is determined by the operation wavelength, refractive

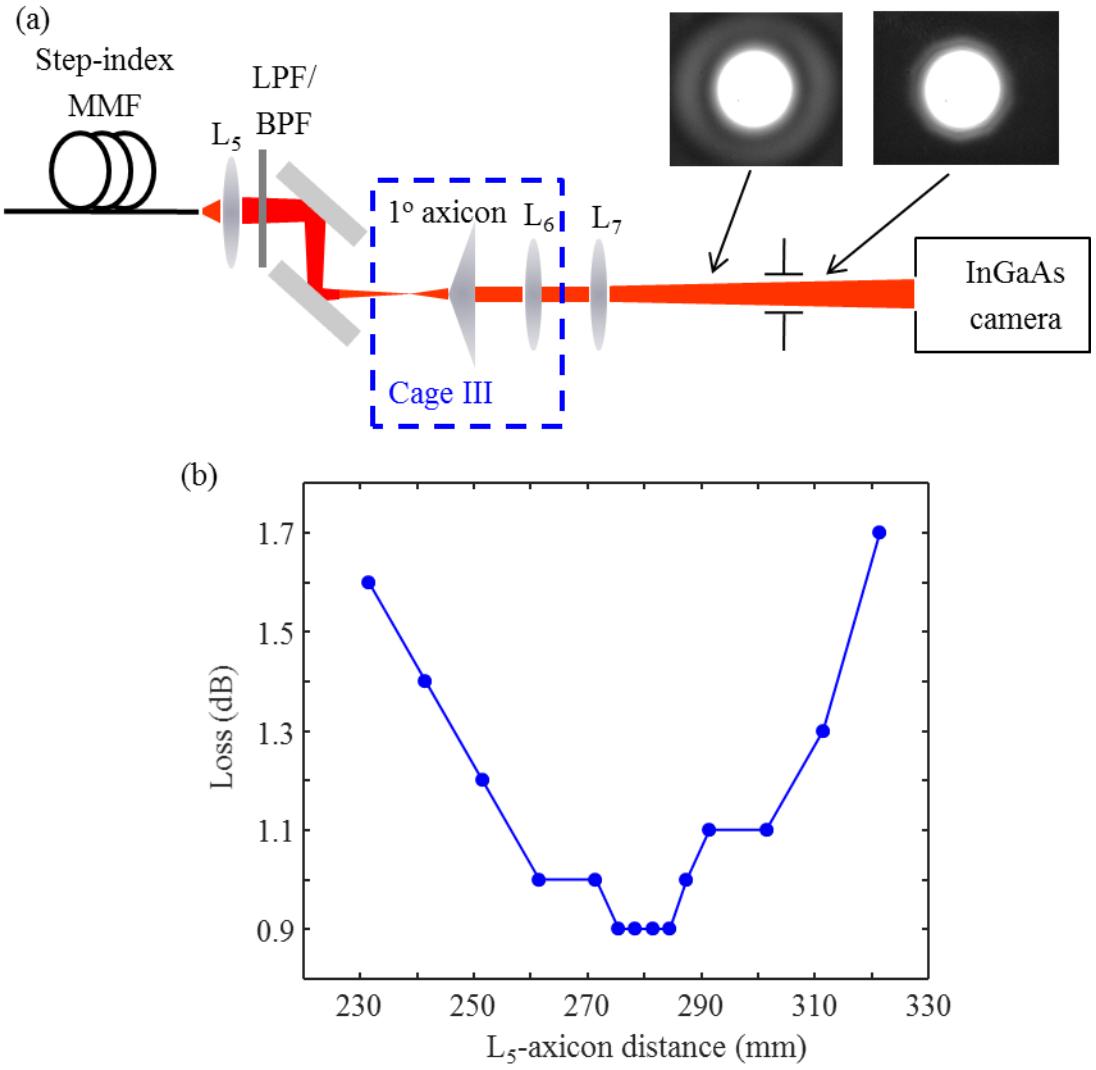

Figure 6.9: (a) The HOM-to-Gaussian setup. (b) The local minimal loss vs. L_5-axicon distance for the 1339 nm Raman soliton. The global minimal loss is 0.9 dB.

index of the material and base angle $\kappa = k_0(n-1)\alpha$. For the $LP_{0,9}$ mode image, the spatial frequency is determined by its image size, which can be adjusted by tuning the distance between the output fiber facet and the lens L_5 to change the magnification factor of the imaging system. Since the beam size in the axicon focal plane is linked to the axicon focal length, or the axicon position, the optimization of loss boils down to searching a proper

axicon position. In the optimization process, different axicon positions are tested. For each axicon position, the $LP_{0,9}$ image size, the positons of lenses L_6 and L_7 need to be adjusted to find out the minimal loss for this specific axicon position (local minimum). The local minima corresponding to different axicon positions are recorded and shown in Fig. 6.9(b), where the axicon positon is represented by the distance between lens L_5 and the axicon. The optimal HOM-to-Gaussian conversion corresponds to the global minimal loss, which, according to the figure, is 0.9 dB when L_5-axicon distance is ~280 mm. Note that the conversion setup is optimized using the 1339 nm Raman soliton. The information on the components in the HOM-to-Gaussian conversion setup are summarized in Table 6.2.

Table 6.2: Summary of the components in the HOM-to-Gaussian conversion setup.

Component	Focal length/Base angle	Coating	Distance	
L_5	8mm	C	28cm	
Axicon	1°	C		12.5cm
L_6	100mm	C	14cm	
L_7	4.51mm	C		

It has been shown that the mode image of $LP_{0,9}$ Raman soliton at ~1370 nm has strong azimuthal modulation pattern due to the effective refractive index crossing between it and higher azimuthal order modes. In order to know if this impure output mode affects the HOM-to-Gaussian conversion or not and how strong the influence is, if any, the conversion for the Raman solitons at both 1339 nm and 1370 nm are compared. It should be mentioned that a new 1° axicon has been used since this comparison experiment, and the optimized loss for the 1339 nm Raman soliton is 1 dB. Using the setup optimized at 1339 nm, the conversion loss for the 1370 nm soliton is 1.3 dB, which is just slightly higher than that for the 1339 nm one. The additional 0.3 dB loss might be because the system is not optimized

at 1370 nm, and/or the impure $LP_{0,9}$ mode indeed affects the conversion efficiency.

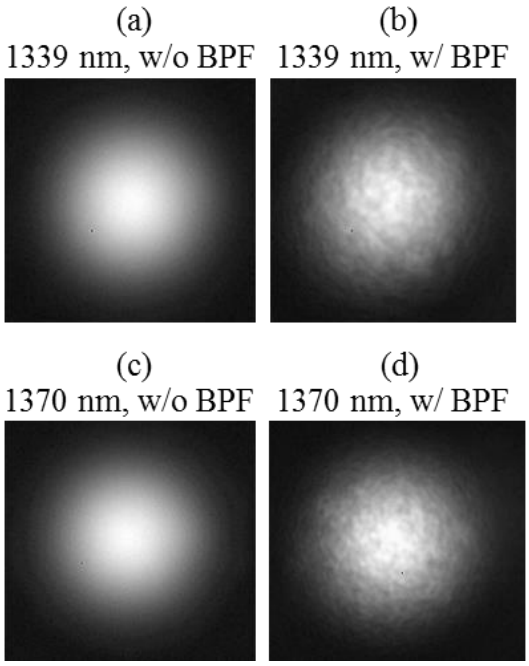

Figure 6.10: The converted Gaussian beam for the 1339 nm and 1370 nm Raman solitons. (a) Conversion at 1339 nm w/o BPF. (b) Conversion at 1339 nm w/ BPF. (c) Conversion at 1370 nm w/o BPF. (d) Conversion at 1370 nm w/ BPF.

The converted Gaussian beams for the 1339 nm and 1370 nm Raman solitons are shown in Fig. 6.10 for comparison. Figure 6.10(a) and (c) show the Gaussian beams when the entire soliton bandwidths are converted, both of them show a good Gaussian profile. In order to enhance the coherence to more easily judge the existence of non-Gaussian profiles, the band-pass filter (BPF) with designed center wavelength of 1400 nm and a bandwidth of 10 nm are used to pick up part of the soliton bandwidth for conversion (the BPF needs to be rotated to shorten its center wavelength down to the soliton wavelengths). The results are given in Fig. 6.10 (b) and (d). The rough feature shown in both beams is because the BPF is dirty (even after cleaning, the rough feature still exists). Both converted beams basically show Gaussian profiles, indicating the impure $LP_{0,9}$ mode at ~1370 nm (Fig.

6.2(d)) probably does not matter to the converted beam profile. Therefore, the azimuthal modulation pattern on top of the $LP_{0,9}$ mode either does not matter to or just slightly degrades (0.3 dB more loss) the HOM-to-Gaussian conversion performance.

It should be mentioned that although the HOM-to-Gaussian conversion setup is optimized at 1339 nm, the performance does not have strong wavelength dependence. When the wavelength increases from 1339 nm to 1370 nm, the loss just changes from 1 dB to 1.3 dB. When the wavelength increases to 1376 nm, the converted beam is not a good-looking Gaussian any more. The lens L_7 needs to be moved toward the InGaAs camera by ~1 mm to get a Gaussian-like beam with 1.2 dB loss.

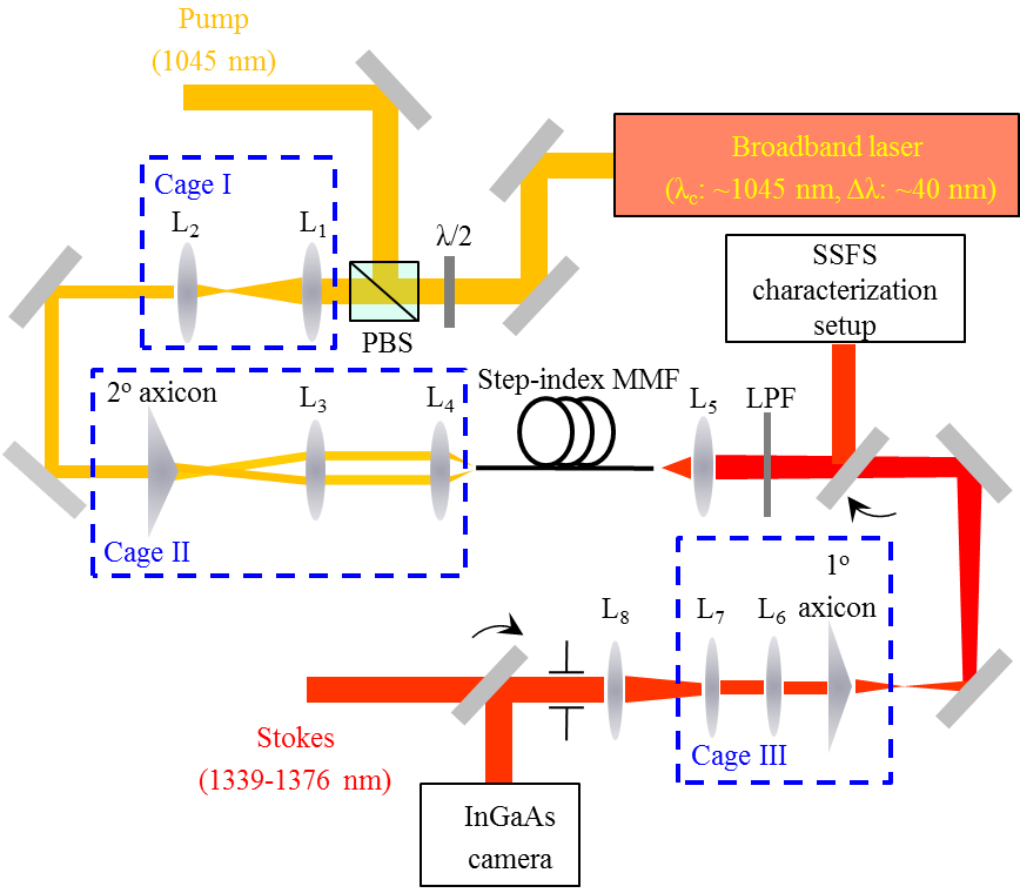

Figure 6.11: The configuration of the dual color source.

6.3 Source characterization

Figure 6.11 shows the entire configuration of the dual color source. Note that the lens L_8 ($f = 200$ mm) is used to collimate the output from the HOM-to-Gaussian conversion setup. It introduces 0.2 dB loss.

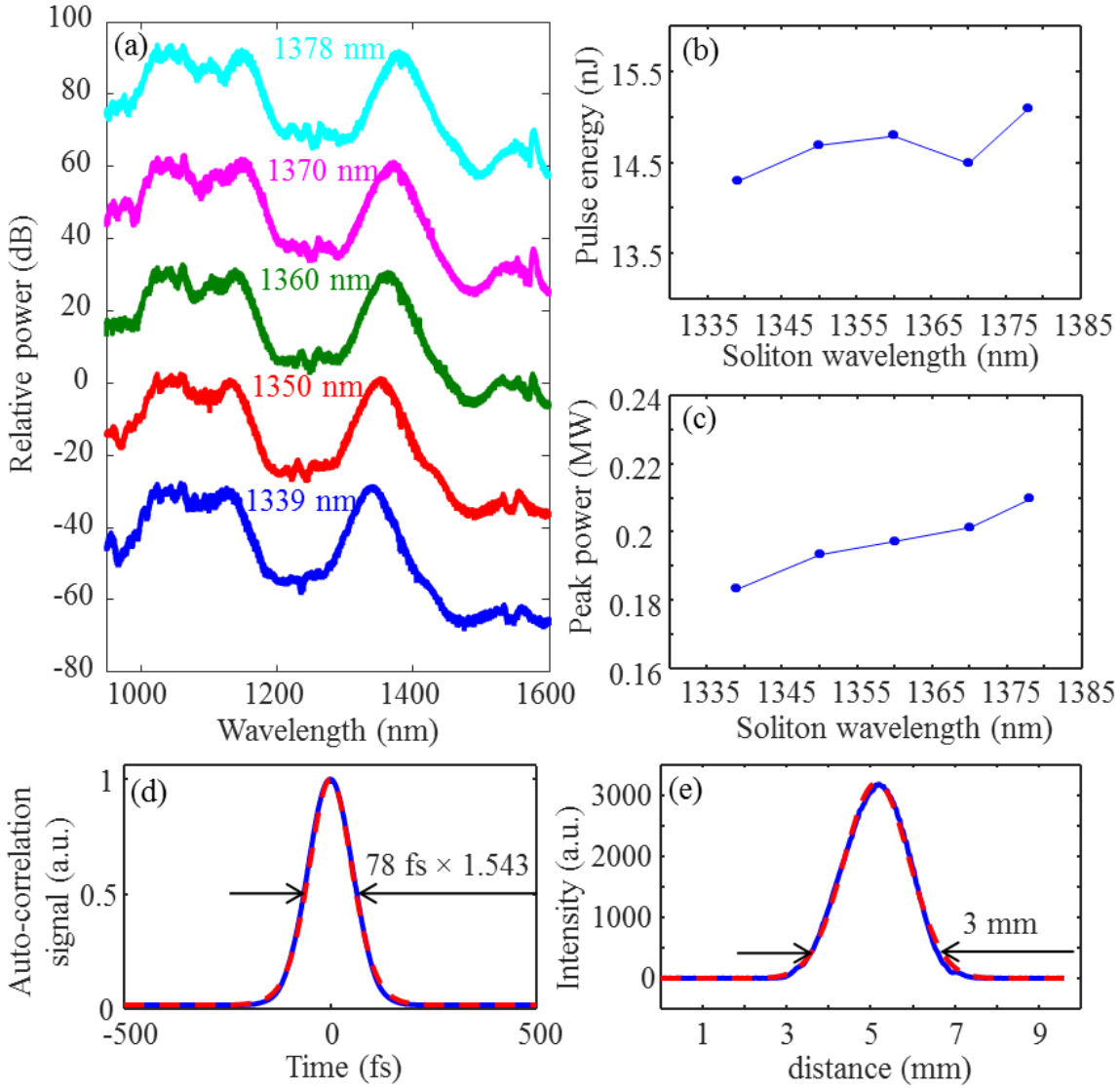

Figure 6.12: Characterization results of the Stokes arm. (a) Typical spectra covering the 1339-1376 nm range. (b) Pulse energies and (c) peak powers for the solitons shown in (a). (d) The pulse duration and (e) beam size measurement for the 1339 nm soliton.

Figure 6.12 shows the characterization of the Stokes arm. The typical spectra covering the 1339-1376 nm range are shown in Fig. 6.12(a). The pulse energies and peak powers corresponding to the Raman solitons are shown in Fig. 6.12(b) and (c). Across the required wavelength range, the pulse energy is ~14.5 nJ, and the peak power is ~0.2 MW. The pulse duration for the Raman solitons at different wavelengths are all ~75 fs. The auto-correlation trace (solid blue curve) and the $sech^2$ fitting (red dashed curve) for the 1339 nm soliton are given in Fig. 6.12(d). The collimated Gaussian beam size ($1/e^2$ diameter) at different wavelengths are all ~3 mm. The horizontal linecut profile of converted Gaussian (solid blue curve) and the Gaussian fitting for the 1339 nm soliton are shown in Fig. 6.12(e).

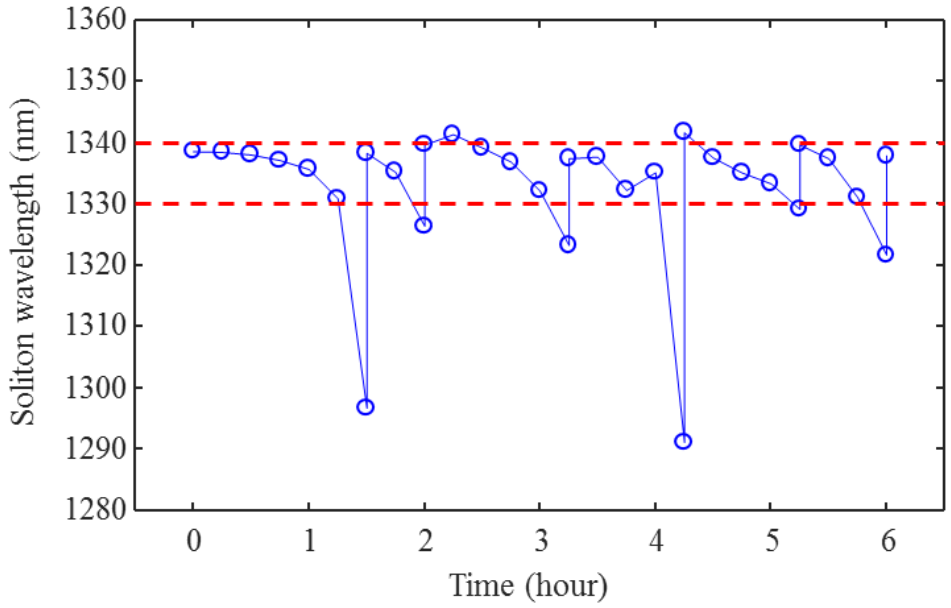

Figure 6.13: Wavelength stability test of the Stokes arm. The wavelength changes by ~10 nm over ~45 minutes.

The wavelength stability of the Stokes arm is also characterized (Fig. 6.13). Clearly, the wavelength is unstable. It changes by ~10 nm over ~45 minutes, corresponding to ~0.3 dB change in the input power. The fiber input is mounted on a 3-dimensional (3D) translation

stage. It is found that for most time in order to get the wavelength back to the original value, only the knob controlling the height of the 3D stage needs to be adjusted, which indicates the wavelength instability is probably mainly due to the mechanical drifting of the stage.

The performance of this dual color source is summarized in Table 6.3.

Table 6.3: Performance summary of the dual color source.

Wavelength (nm)	Energy (nJ)	Pulse duration (fs)	Peak power (MW)	Beam diameter ($1/e^2$) (mm)
Pump				
1045	> 400	< 100	> 4	2.7
Stokes (covering 1339-1376 nm range, the performance at some typical wavelengths are listed below)				
1339	14.4	78	0.18	3
1350	14.7	76	0.19	2.9
1360	14.7	75	0.20	2.9
1370	14.5	72	0.20	2.8
1378	15.2	72	0.21	2.9

The recent characterization has indicated there is a strong relative timing jitter (RTJ) between the pump and Stokes (i.e. the soliton) arms (Fig. 6.14). Figure 6.14(a)-(d) show the measurements on the second harmonic generation (SHG) signals produced by the pump and soliton pulses, the small amplitude fluctuations of the signal peak values (3.8% relative standard deviation (RSD) for the pump, and 3.3% RSD for the soliton; RSD is defined as the ratio of standard deviation to average) indicate that the powers of both pump laser and soliton are stable. However, the sum frequency generation (SFG) signal, produced by mixing the two pulses (Fig. 6.14(e)), has a very strong fluctuation (41.9% RSD, Fig. 6.14(f)), which means the existence of a strong RTJ between them. This issue

can degrade CARS/SRS measurement seriously.

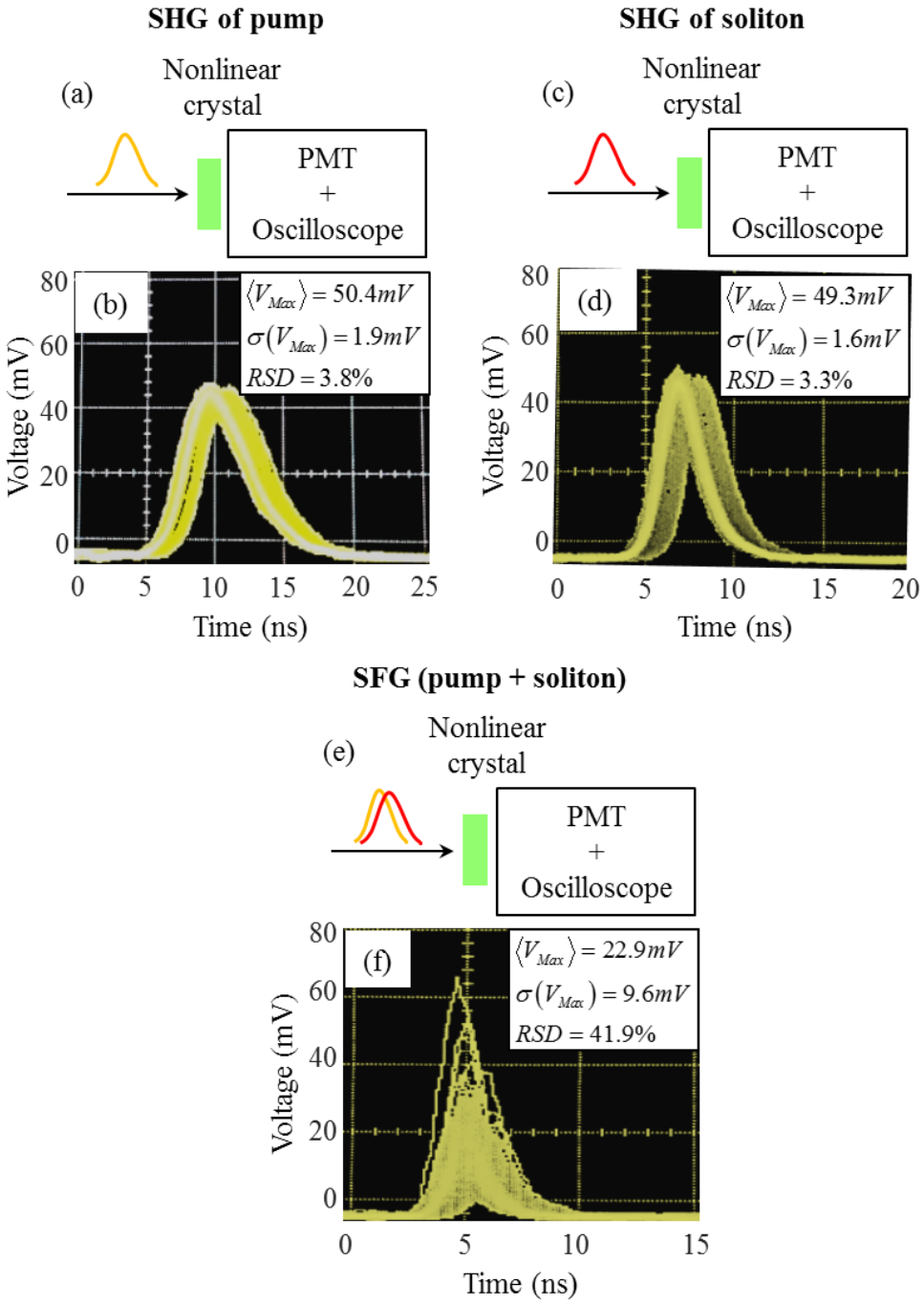

Figure 6.14: (a) SHG generation using the pump and (b) the corresponding oscilloscope traces. (c) SHG generation using the soliton and (d) the corresponding oscilloscope traces. (e) SFG generation by mixing the pump and soliton and (f) the corresponding oscilloscope traces. (Data courtesy of Dr. Fengyuan Deng and Professor Ji-Xin Cheng)

The RTJ between the pump and soliton pulses can be estimated by simulating the SFG generation. The SFG signal can be expressed as

$$P_{SFG}(t) \propto P_{pump}(t) \cdot P_{soliton}(t-\tau) \tag{6.3}$$

where τ is the relative time delay between the two pulses. Through the auto-correlation measurements, it is known that the pump is about a transform-limited Gaussian pulse with FWHM of 100 fs, and the soliton is a transform-limited sech^2 pulse with FWHM of 77 fs. In the simulation, two transform-limited pulses are created to represent the pump and soliton, respectively, which are given by

$$P_{pump}(t) = e^{-\frac{t^2}{t_{0,pump}^2}} \tag{6.4}$$

$$P_{soliton}(t) = \text{sech}^2\left(\frac{t-\tau}{t_{0,soliton}}\right) \tag{6.5}$$

where $t_{0,pump} = 100/1.665$ fs, and $t_{0,soliton} = 77/1.763$ fs. The SFG signal can then be calculated using Eq. (6.3), and the relation between the peak of the signal and the relative time delay τ can be found, which is shown in Fig. 6.15, where the maximal peak value is normalized to 1. When the normalized SFG signal peak value decreases to the minimum, i.e. 40.9% (roughly obtained from the experimental data: (22.9-9.6)/(22.9+9.6) = 40.9%), the corresponding two relative time delay points span 142 fs, meaning the soliton pulse moves back and forth between -71 fs and 71 fs relative to the pump pulse. Since both pump and soliton pulses are (almost) symmetric in the temporal domain, the SFG signal peak value is symmetric about the relative time delay τ. Therefore, the RTJ considered here

(also throughout the entire thesis) only takes the positive (or negative) side of relative time delay τ, which is 71 fs in this measurement.

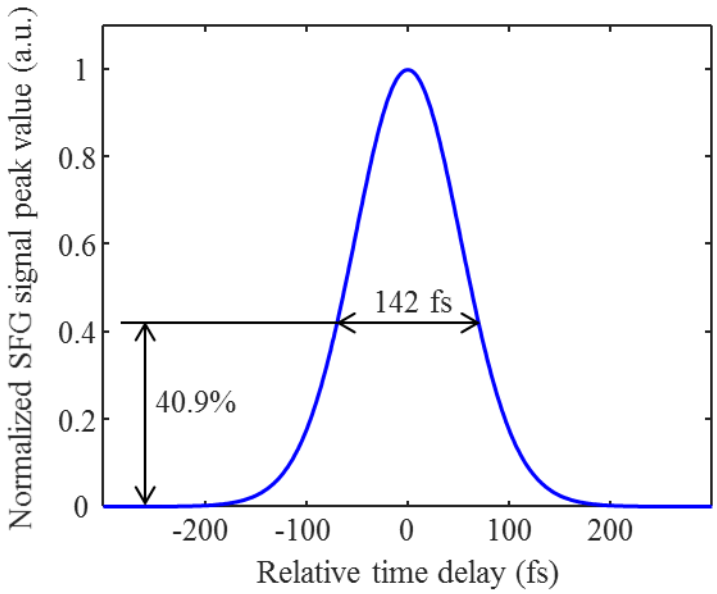

Figure 6.15: The normalized SFG signal peak value v.s. relative time delay between the pump and soliton pulses.

One way to get rid of/mitigate the influence of RTJ on CARS measurement is taking part of power from both pump and soliton pulses to obtain the SFG signal, which is then used to calibrate the CARS signal. The CARS signal can be expressed as

$$P_{CARS}(t) \propto P_{pump}^{2}(t) \cdot P_{soliton}(t-\tau) \tag{6.6}$$

The relation between the peak of CARS signal and relative time delay τ can also be simulated, which is shown in Fig. 6.16 (the red trace) and compared with the SFG curve (i.e. the curve in Fig. 6.15). The relative time delay τ can be acquired by measuring the SFG signal, and the influence of this delay on the CARS signal can then be estimated using the red trace in Fig. 6.16, based on which the CARS measurement can be calibrated.

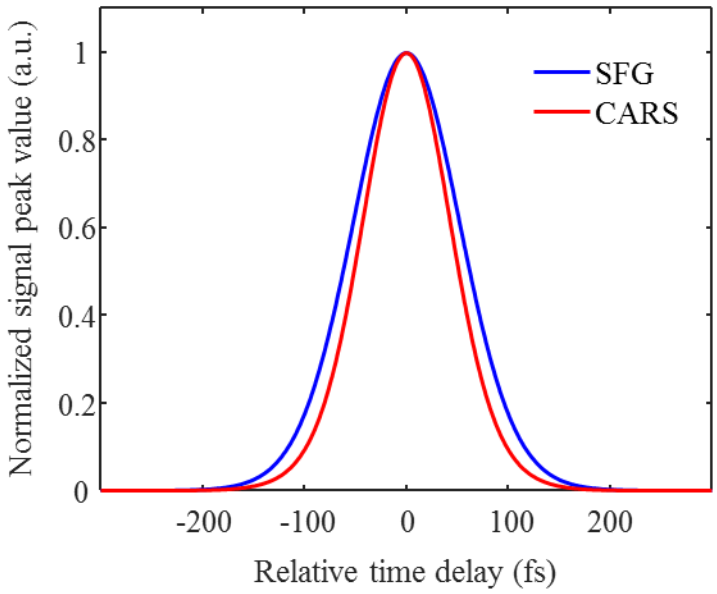

Figure 6.16: The normalized signal peak value v.s. relative time delay between the pump and soliton pulses.

A more fundamental way to solve the RTJ problem is generating two temporally synchronized pulses from the fiber. Figure 6.17(a) shows the use of one pair of SSMC modes to produce SFG when they interact with each other and have equal amount of power. Due to the group refractive index matching, i.e. the two pulses propagating with the same speed, the relative timing jitter issue disappears, and the stable SFG signal (with only 5.1% RSD) is obtained (Fig. 6.17(b)). The results shown in Fig. 6.17 are just initial results obtained recently, the further work on this SSMC mode pair solution does not belong to the scope of this thesis.

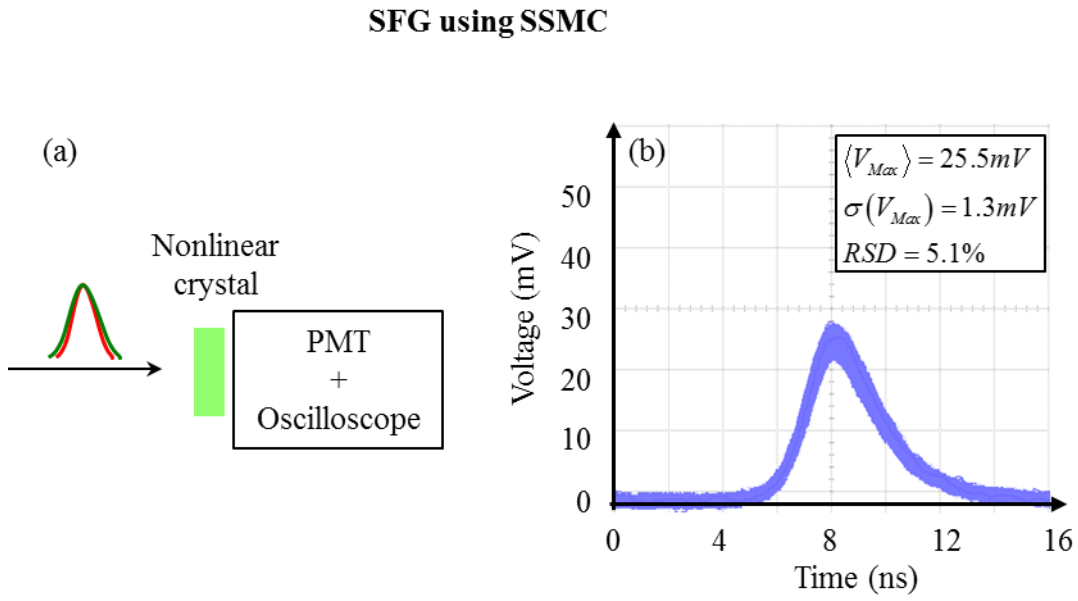

Figure 6.17: (a) SFG generation by mixing a pair of SSMC modes. (b) The oscilloscope traces showing the small signal fluctuation of the SFG generated from setup (a). (Data courtesy of Dr. Lars Rishøj)

6.4 Summary

This chapter has described the buildup of a compact dual color source for CARS/SRS. In the Stokes arm, both HOM excitation and HOM-to-Gaussian conversion are achieved using the commercially available axicons. For HOM excitation, the MPI measurement method based on Raman soliton wavelength is introduced. The ultimate optimization gives -6 dB MPI, and 0.8 dB coupling loss. The HOM-to-Gaussian conversion is optimized at 1339 nm, and the loss is minimized to 1 dB. The dual color source outputs > 4 MW peak power at 1045 nm, and ~0.2 MW across the range of 1339-1376 nm (the detailed performance can be found in Table. 6.3). This source may be useful for CARS/SRS microscopy to image C−D and C≡C bonds.

Several problems exist in the system. (1) The wavelength of the Stokes arm changes by ~10 nm over ~45 minutes, which is probably due to the mechanical drifting the 3D stage holding the fiber input. This problem may be solved by using a more stable stage, such as a 6D stage, to mount the fiber. (2) There is a strong relative timing jitter between the pump and Stokes arms, which can strongly degrade the CARS/SRS measurement. The use of a pair of temporally synchronized SSMC modes may provide a solution to this problem.

Chapter 7

Soliton Power Scaling and Wavelength Extension

In chapter 2 and 3, both theoretical simulation and experimental data have shown that the soliton energy at a given wavelength can be increased by enhancing the product of dispersion and effective mode area (DA product) at pump wavelength. Previous work has also shown the soliton peak power at a given wavelength can be increased using the same method (Rishoj et al., 2016; Rishoj et al., 2018). Therefore, DA scaling at the pump wavelength is an effective way to scale the soliton power at a target wavelength, including both average power, which is proportional to the pulse energy, and peak power. Another way to improve the soliton power at a given wavelength is increasing the input pump power while shortening the fiber length, i.e. pump power scaling. Based on these two methods, the strong soliton pulse with a pulse energy of ~80 nJ and peak power of ~1.1 MW has been demonstrated (Rishoj et al., 2018). However, both power scaling strategies have limitations. In section 7.1, these limitations are described, based on which the further soliton power scaling is predicted by simulating the fibers with core diameters and numerical apertures (NA's) larger than what have been shown so far in this thesis. In section 7.2, the extension of soliton self-frequency shift (SSFS) and soliton self-mode conversion (SSMC) to the mid infrared (MIR) wavelength window is discussed. The summary is given in section 7.3.

7.1 Soliton power scaling

7.1.1 NA limitation

Since the soliton power scaling can be achieved by DA scaling at the pump wavelength, and it has been shown the DA product a fiber provides increases with mode order, core diameter and NA, the power scaling boils down to using a fiber with as large core diameter and as high NA as possible, and a mode of as high order as possible. However, this power scaling strategy hits the NA limitation.

In chapter 2, it has been presented that larger core diameter decreases the neff splitting Δn_{eff} between $LP_{0,m}$ and $LP_{1,m}$; in contrast, higher NA increases the splitting. Therefore, when scaling the DA product, larger core diameters need to be accompanied by higher NA's in order to ensure there are modes being able to stably propagate at the pump wavelength. With the current silica fiber fabrication techniques, the core diameter can be on the order of millimeter. In contrast, the high NA is harder to achieve. The core and cladding need to be highly doped with germanium (Ge) and fluorine (F) respectively, which can cause internal stress and/or cracking around the core-cladding interface during the manufacture. Nowadays, the highest NA is only ~0.34. Therefore, the DA scaling method is limited by the highest NA optical fibers can offer. Besides the existence of stable propagation modes, there is another requirement—formation of the first Raman soliton, which is related to cutoff wavelength. The cutoff wavelength of the launching mode used to start SSFS and SSMC cannot be too close to the pump wavelength, otherwise the generation of the first Raman soliton in the launching mode is prevented by energy

coupling to the Cherenkov radiation. For a given fiber core diameter, the cutoff wavelength of a mode is determined by NA. The higher the NA, the larger the cutoff wavelength, so in terms of cutoff wavelength the limitation is also from NA, which needs to be large enough so that some of stable propagation modes at the pump wavelength can form a Raman soliton.

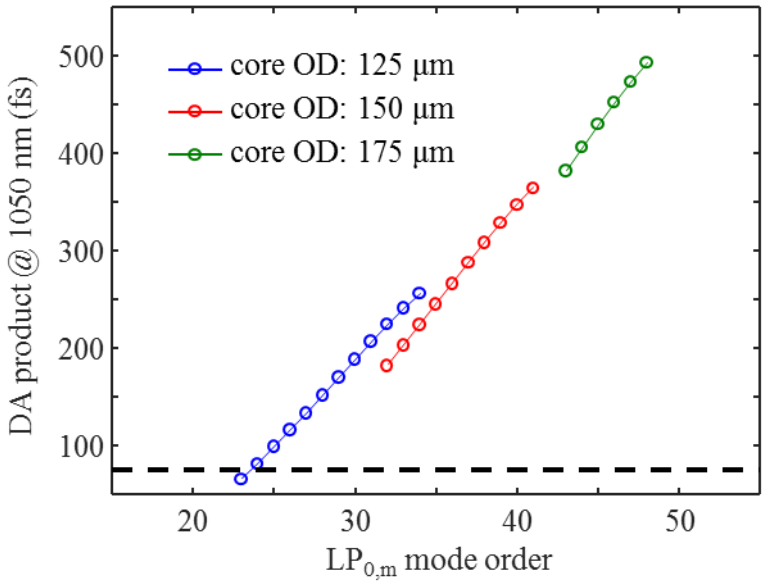

Figure 7.1: DA product at 1050 nm for fibers with the same NA (0.34) but different core diameters. The simulated modes are anomalously dispersive and have $\Delta n_{eff} \geq 5\times10^{-4}$ at 1050 nm, and have cutoff wavelength ≥ 1250 nm. The black dashed line represents the DA product value of $LP_{0,21}$ mode that was used to generate the strong soliton with ~1.1 MW peak power at ~1300 nm.

The fibers used in the experiments shown in chapter 5 and 6 are highly doped silica fibers with NA of 0.34. Thus, the DA scaling is simplified to just increasing the core diameter of these fibers, and then choosing the highest mode order satisfying both stable propagation and formation of the first Raman soliton requirements. Based on our experimental experience, the stable modes at ~1050 nm (our pump wavelength) should have

$\Delta n_{eff} \geq 5\times10^{-4}$. Both theoretical simulation and experimental results show that the first Raman soliton can be formed at ~1150 nm, and the corresponding cutoff wavelength needs to be ≥ 1250 nm. Under these two criteria, the DA products of anomalously dispersive modes at the pump wavelength (1050 nm) are simulated in fibers with the same NA of 0.34 but different core diameters (Fig. 7.1). It can be clearly seen that the number of remaining modes does become less with core size due to the NA limitation. When the core diameter is 175 μm, there are only 6 modes left. When the core dimeter is ≥ 200 μm, no mode can simultaneously meet neff splitting and cutoff wavelength criteria. As seen from Fig. 7.1, in the 175 μm core diameter fiber, the DA product at pump wavelength is scaled up to ~500 fs (the $LP_{0,48}$ mode), which is much higher than that of the mode generating ~80 nJ, ~1.1 MW pulses at ~1300 nm (~75 fs, represented by the black dashed line in Fig. 7.1), indicating the pulse energy generated from the 175 μm core diameter fiber can be much higher.

7.1.2 Self-action/dielectric breakdown limitation

It is known there are two different fiber damage mechanisms, i.e. self-focusing and dielectric breakdown. For Gaussian or approximately Gaussian beams, self-focusing is a nonlinear effect that only depends on peak power (Chiao et al., 1964). The threshold power (also called critical power), at which the beam neither converges nor diverges, can be expressed as (Fibich and Gaeta, 2000)

$$P_{th} = \frac{1.8962}{4\pi} \cdot \frac{\lambda^2}{n \cdot n_2} \tag{7.1}$$

where λ is the wavelength, n is the refractive index of the pulse propagation medium, and n_2 is the nonlinear-index coefficient. In silica fibers, at ~1050 nm the threshold power is ~4.4 MW. For higher order modes (HOMs), the theoretical simulations have shown that (1) over a short propagation distance, the threshold power increases significantly with mode order for Laguerre-Gaussian beams (Haus, 1966; Ramachandran et al., 2008); and (2) over a long propagation distance, when the peak power is significantly higher than that given by Eq. (7.1), the intensity profiles of $LP_{0,m}$ modes get distorted due to spatial modulation instability (Hadley, 2008; Ramachandran et al., 2008). Therefore, HOMs may not damage fibers base on self-focusing, but their beam profiles could be distorted by Kerr effect. Furthermore, the threshold power for HOMs to suffer from the distortion may be comparable to that of self-focusing for Gaussian beams. More experimental work is required to understand the peak power limitation on HOMs better. Both self-focusing and the beam profile distortion can be classified into self-action effect. Dielectric breakdown is a nonlinear effect that depends on intensity and results in local bond breaking. The factors, such as material composition and manufacture procedure of optical fibers, matter to the threshold intensity at which dielectric breakdown just occurs (Stuart et al., 1995; Ramachandran et al., 2008). The average of reported threshold intensities can be expressed as (Ramachandran et al., 2008)

$$I_{th} = \frac{300}{\sqrt{\tau(ns)}} GW/cm^2 \tag{7.2}$$

where τ is the pulse duration.

In our experiments, the fiber damage has been observed based on the change in soliton properties. If the soliton wavelength and/or energy are significantly reduced (by > 10 nm, and > 10 nJ) under the same experimental conditions, the fiber sample is thought to be damaged. Figure 7.2 shows the soliton spectra and energies of a sample before and after damage. The threshold damage situation corresponds to the lowest pump power at which the fiber damage happens. The data corresponding to the threshold situation have been collected on three fiber samples, of which the core diameters, NA's and launching modes are (1) 52 μm, 0.24, $LP_{0,9}$, (2) 48 μm, 0.34, $LP_{0,11}$, and (3) 87 μm, 0.34, $LP_{0,19}$, respectively.

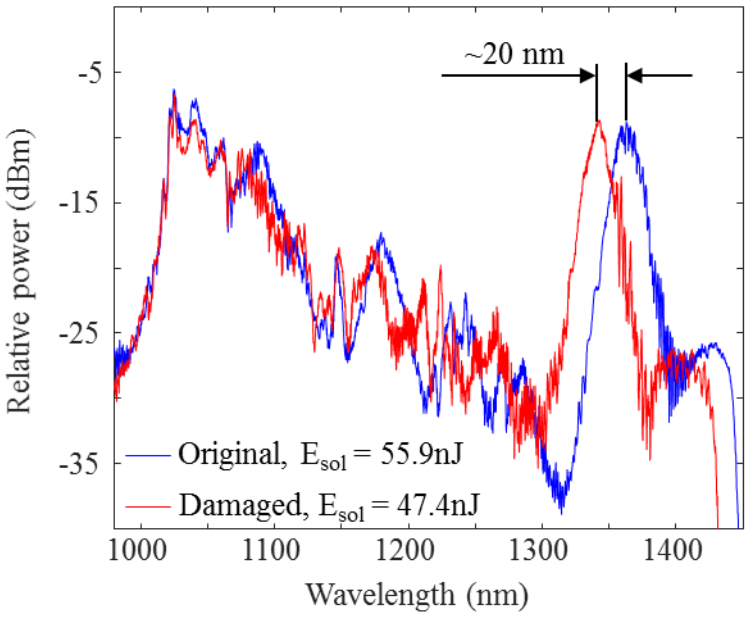

Figure 7.2: Soliton spectra and energies of a sample before and after damage.

The pump laser emits pulses at ~1045 nm with pulse durations of ~100 fs. In order to determine which mechanism causes the fiber damage in our experiments, the threshold damaging peak power and peak intensity of the launching mode need to be compared among the three samples. The expectation is that if the threshold damaging peak powers

are close to each other, self-action is the damaging mechanism; if the threshold damaging peak intensities are close to each other, dielectric breakdown is the mechanism. The comparison is shown in Fig. 7.3.

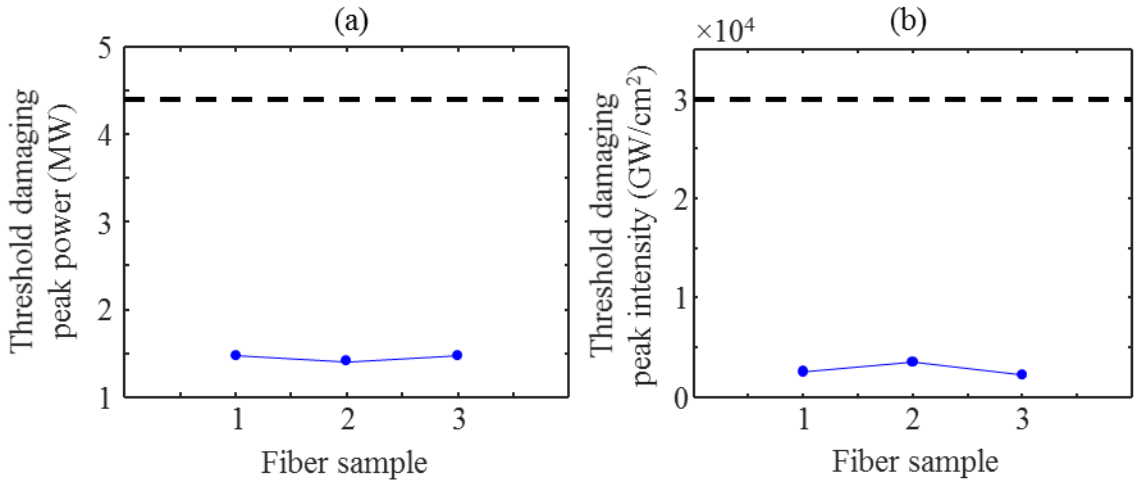

Figure 7.3: (a) The comparison of threshold damaging peak powers among different fiber samples. The black dashed line represents the theoretical calculation result based on Eq. (7.1). (b) The comparison of threshold damaging peak intensities among different fiber samples. The black dashed line represents the theoretical calculation result based on Eq. (7.2). The pump source emits pulses at ~1045nm, with pulse durations of ~100 fs. The core diameters, NA's and modes corresponding to the samples are: (1) 52 μm, 0.24, $LP_{0,9}$, (2) 48 μm, 0.34, $LP_{0,11}$, and (3) 87 μm, 0.34, $LP_{0,19}$.

Cleary, for the three samples, both threshold damaging peak powers and peak intensities are close to each other. The averages are 1.46 MW and 2.87×10^3 GW/cm^2, respectively. Therefore, both self-action and dielectric breakdown could be the damage mechanism in our experiments, limiting the input pump power scaling strategy to scale soliton power. In addition, as shown in Fig. 7.3, the measured threshold values are lower than the theoretical predictions. For the self-action effect (Fig. 7.3(a)), this discrepancy might be due to that the theory has been developed only for Gaussian shaped beams (Chiao et al., 1964; Fibich and Gaeta, 2000). For the dielectric breakdown effect (Fig. 7.3(b)), this discrepancy can be

related to the concentration of dopants, manufacture procedure of fibers, test conditions, and damaging judgement criterion. For example, in the previous study the change in material surface structure was used to determine the damage (Stuart et al., 1995); however, in our measurement the change in soliton spectrum is the criterion.

7.1.3 Soliton power scaling

Since it cannot be determined which is the damage mechanism between self-action and dielectric breakdown, the following soliton power scaling simulation, using the generalized nonlinear Schrödinger equation (GNLSE) (Dudley and Taylor, 2010) presented in chapter 3, is implemented for both cases.

The three fibers shown in Fig. 7.1 (core OD: 125 μm, 150 μm, 175 μm; NA: 0.34) are simulated. For each of them among the modes surviving both neff splitting and cutoff wavelength criteria, the one of the highest order is used for the pulse propagation simulation, because it has the largest DA product, and generates the highest soliton energy. Because our GNLSE model is only able to deal with SSFS, it is assumed the launching mode keeps shifting itself to ~1150 nm (1145-1155 nm) by way of SSFS, and the exact soliton wavelength, pulse energy, pulse duration, and peak power can be obtained through the simulation. Since 1300 nm is the desired wavelength for excitation sources in nonlinear microscopy (NM), the pule energy at this wavelength needs to be calculated. The wavelength conversion from ~1150 nm to 1300 nm involves both SSFS and SSMC, but it has been shown that both processes conserve the number of photons, i.e. the loss is only from photon-phonon interaction, based on which the pulse energy at 1300 nm can be

calculated. However, the pulse duration and peak power are unknown at this wavelength due to the lack of knowledge on mode order. In order to make the simulation close to the real experiments, the input pump pulse is created by first implementing Fourier transform (FT) on the measured pump spectrum to get a transform-limited pulse, and then using the third order dispersion to slightly chirp the pulse until the pulse duration reaches the measured value, i.e. FWHM of 102 fs (assuming the pulse is in a Gaussian shape). The validity of our model has been confirmed in chapter 3 by comparing the simulated and measured soliton energies for both SSFS (Fig. 3.4) and SSMC (Fig. 3.7) processes. To get the highest obtainable soliton power, the input pump pulse energy is set to a value such that under self-action constraint the input peak power is just 1 dB (or 20.6%) lower than the average threshold damaging peak power, i.e. 1.16 MW; and under dielectric breakdown constraint the input peak intensity is just 1 dB lower than the average threshold damaging peak intensity, i.e. 2.28×10^3 GW/cm^2. This 1 dB buffer used to prevent the fiber sample being damaged is also what is done in our experiments.

The simulation results with self-action constraint are shown in Fig. 7.4. The soliton pulse energy increases with fiber core diameter at both ~1150 nm and 1300 nm, but the improvement is quite small. When the core diameter increases from 125 μm to 175 μm, the energy increases by less than 5 nJ. This is because self-action limitation slows down the energy scaling to a large extent, which further leads to the decrease of soliton peak power at ~1150 nm with fiber core size (the red trace in Fig. 7.4(a)). Although the peak power at 1300 nm cannot be simulated, it is reasonable to expect that it also decreases with fiber core diameter due to the slow energy scaling. In addition to the fibers shown in Fig. 7.1,

the simulation is also done on $LP_{0,19}$ mode in the fiber with a core diameter of 87 μm and NA of 0.34, and compared with the experiment, where the 1dB power buffer is also used and the soliton wavelength is 1363 nm. The simulated pulse energy is close to the measurement (the red cross in Fig. 7.4(b)), indicating our model is indeed able to predict the soliton power scaling under the self-action limitation.

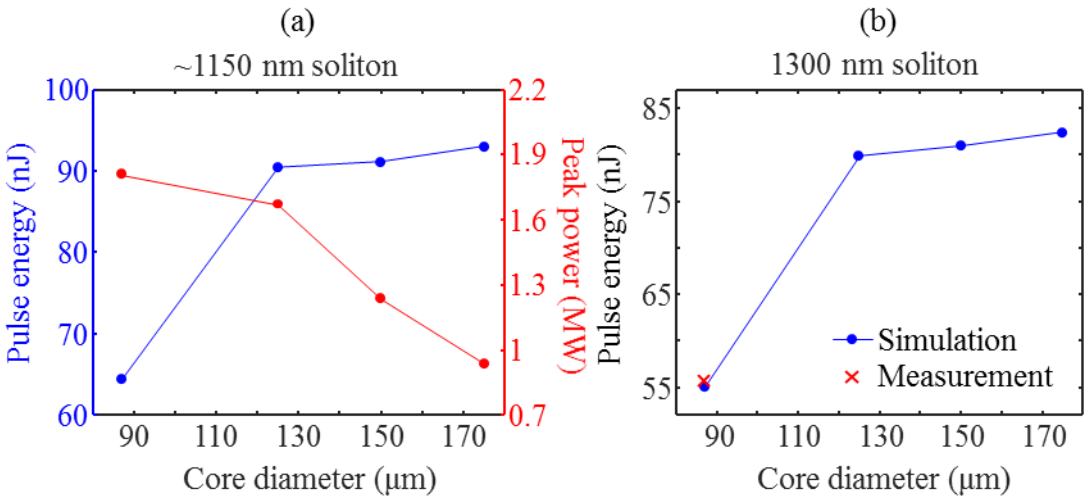

Figure 7.4: (a) The pulse energy and peak power of the ~1150 nm soliton vs. fiber core diameter. (b) The pulse energy of the 1300 nm soliton vs. fiber core diameter. The limitation is self-action.

The simulation results with dielectric breakdown constraint are shown in Fig. 7.5. Figure 7.5(a) gives the evolution of input pump pulse energy with fiber core size. Unlike the self-action case, the input pump power increases with fiber core size, explaining why the pulse energies of solitons at both ~1150 nm and 1300 nm scale much more quickly than the self-action case (the blue trace in Fig. 7.5(b) and (c)), leading to the increase of soliton peak power at ~1150 nm with fiber core diameter (the red trace in Fig. 7.5(b)). The increase of peak power at 1300 nm with core size is also expected. The comparison between simulation and experiment is also done on $LP_{0,19}$ mode in the fiber with a core diameter of 87 μm and

NA of 0.34, and the similar pulse energies indicate the validity of our model to predict the soliton power scaling under the dielectric breakdown limitation.

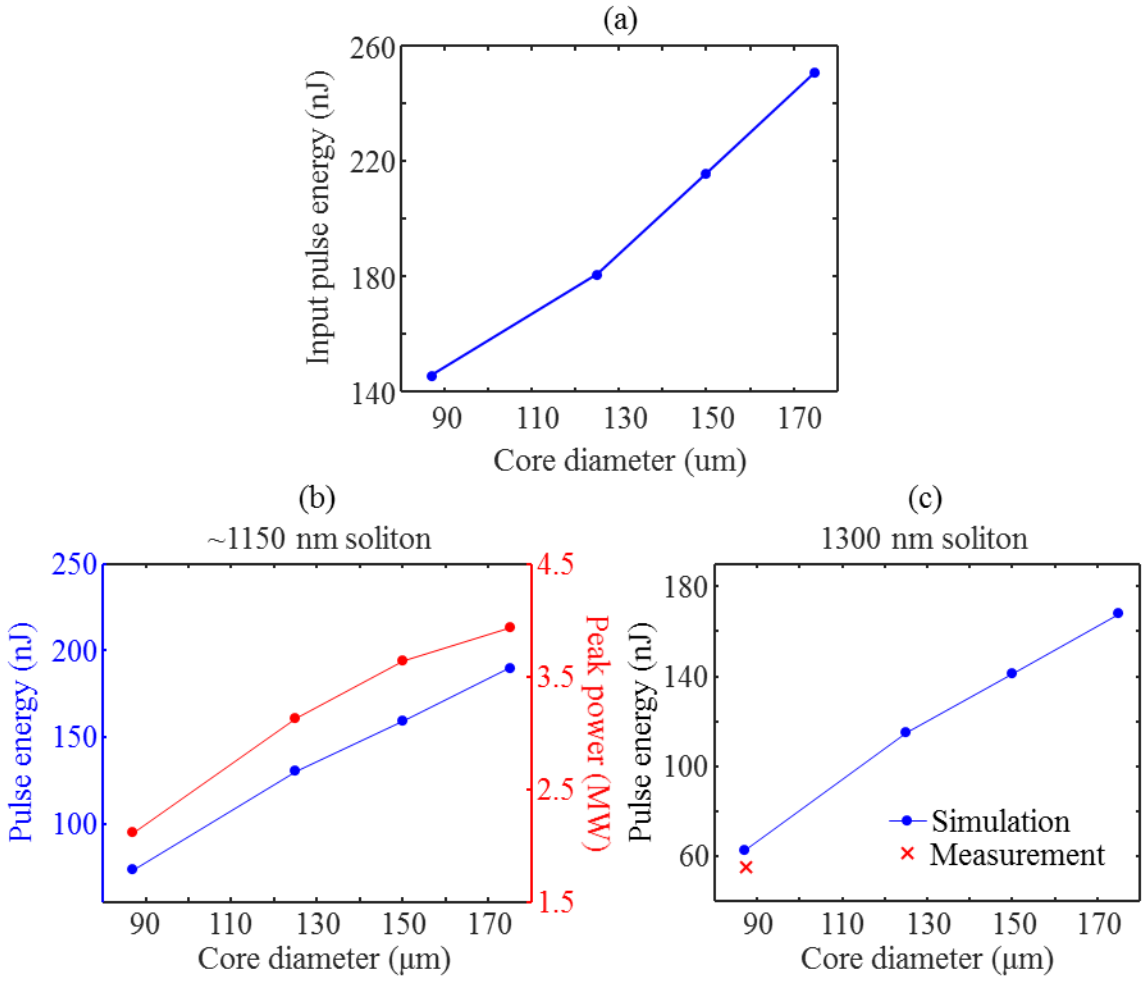

Figure 7.5: (a) The input pulse energy v.s. fiber core diameter. (b) The pulse energy and peak power of the ~1150 nm soliton v.s. fiber core diameter. (c) The pulse energy of the 1300 nm soliton v.s. fiber core diameter. The limitation is dielectric breakdown.

To sum up, it has been shown that under fiber NA and fiber damage/beam profile distortion limitations (including both self-action and dielectric breakdown), the soliton pulse energy (also average power) can be scaled up at a given wavelength, e.g. 1300 nm, with DA product at the pump wavelength. If the fiber damage mechanism is self-action,

the energy scaling is slow, and the peak power decreases (when only SSFS occurs), or is expected to decrease (when both SSFS and SSMC occur) with DA product. If the damage mechanism is dielectric breakdown, the energy scaling is much quicker, and the peak power increases (when only SSFS occurs), or is expected to increase (when both SSFS and SSMC occur) with DA product. Under the self-action constraint, the limit (corresponding to the 175 μm core diameter result) of soliton pulse energy at ~1300 nm is ~83 nJ. Under the dielectric breakdown constraint, that is ~168 nJ.

7.2 Wavelength extension

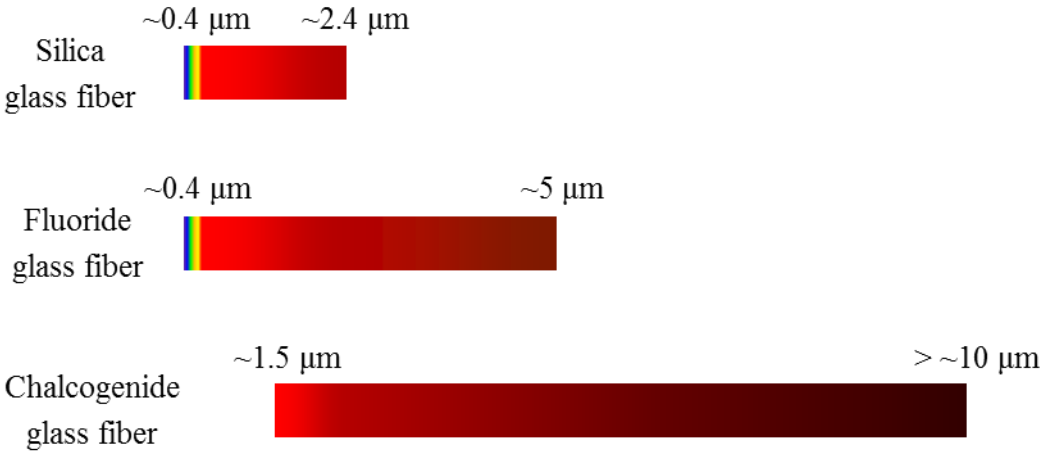

Figure 7.6: The comparison of transmission windows between silica fiber and MIR fibers, including fluoride glass and chalcogenide glass fibers.

So far, all the SSFS and SSMC processes described in the thesis are implemented in the silica fibers which prevent the wavelength translation beyond ~2.2 μm due to the high absorption loss of silica. However, these two processes are not fundamentally restricted by wavelength, and they can be applied in fluoride glass and chalcogenide glass fibers to

achieve the wavelength conversion in MIR window. The comparison of transmission window between silica and MIR fibers is shown in Fig. 7.6. Clearly, the wavelength shift up to ~10 µm can be realized in MIR fibers (Kim et al., 2016).

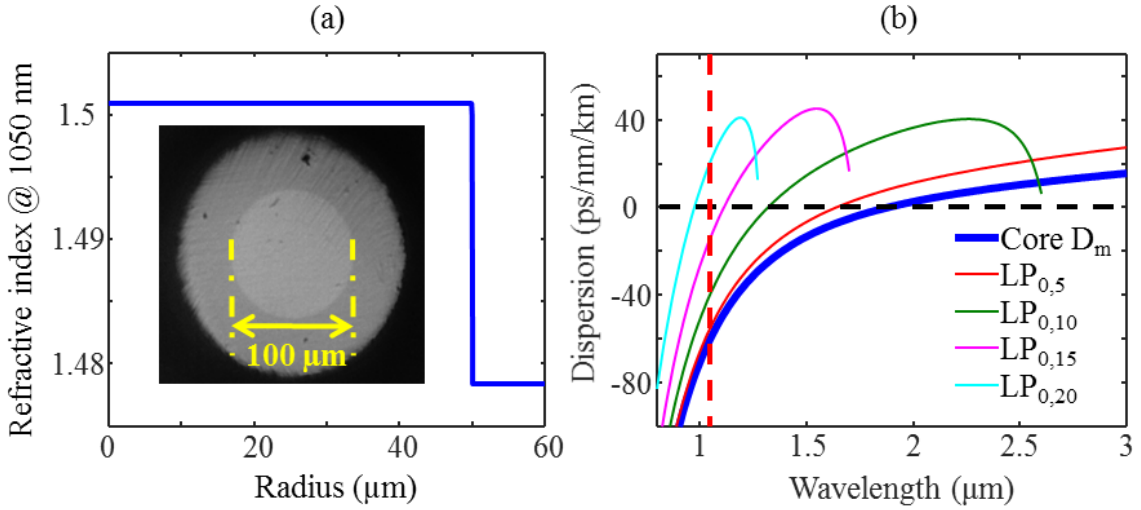

Figure 7.7: (a) The refractive index profile and cross-section of a commercial InF_3 fiber. (b) The core material dispersion and modal dispersion of some $LP_{0,m}$ modes.

Figure 7.7(a) shows the refractive index profile and cross-section of a commercial InF_3 fiber with a core diameter of 100 µm and NA of 0.26. Figure 7.7(b) shows the dispersion of some $LP_{0,m}$ modes, and the material dispersion of fiber core. Unlike silica fibers, the zero material dispersion wavelength in InF_3 fibers is ~1.9 µm. Thus, if the lower order modes are used to implement SSFS and SSMC, the pump wavelength should be ≥ ~1.9 µm, e.g. thulium (Tm) fiber laser. If the HOMs are used, such as the $LP_{0,20}$ mode, the anomalous dispersion can be obtained even at wavelengths < 1050 nm (marked by the red dashed line), and the wavelength conversion can sweep from the near infrared (NIR) to MIR window by using only one pump source, e.g. ytterbium (Yb) fiber laser.

The soliton power scaling can also be explored in the MIR fibers. The self-action and dielectric breakdown effects are both dependent on laser wavelength. This dependence is explicitly expressed in Eq. (7.1) for the self-action effect, but not included in Eq. (7.2) for the dielectric breakdown effect. According to the previous work (Michalska et al., 2016), the threshold peak intensity to damage the InF_3 fiber (corresponding to the dielectric breakdown) is ~200 GW/cm^2 when using a laser emitting ~70 ps pulses at 2 μm. Therefore, according to Eq. (7.2), the threshold peak intensity for a 2 μm, 100 fs (FWHM) transform-limited laser (the source used in the GNLSE simulation below) is ~5.29×10^3 GW/cm^2. In order to compare the power scaling performance between self-action limitation and dielectric breakdown limitation cases, the threshold peak power to damage the InF_3 fiber (corresponding to the self-action) is calculated at 2 μm, and the result is 12.6 MW. Note that the nonlinear index coefficient n_2 takes the value of 3.2×10^{-20} m^2/W (Basaldua et al., 2018).

Under the $\Delta n_{eff} \geq 5\times10^{-4}$ and cutoff wavelength ≥ 2450 nm criteria, the DA products at pump wavelength (2 μm), for the InF_3 fiber given in Fig. 7.7(a) and its geometrically scaled versions, are simulated (Fig. 7.8). The largest fiber core dimeter can be 250 μm.

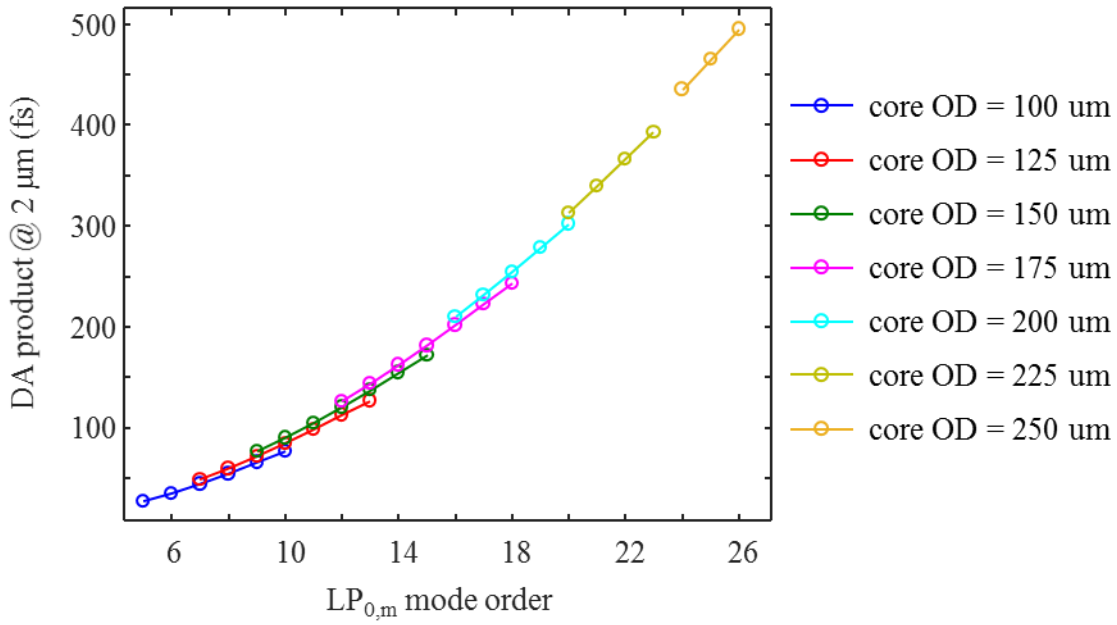

Figure 7.8: DA at 2 μm (the pump wavelength) versus mode order for different sizes of InF_3 fibers.

In the pulse propagation simulation based on GNLSE, the pump is a $sech^2$ pulse with the pulse duration of 100 fs (FWHM) at 2 μm. The input pump power is kept 1 dB lower than the damaging threshold. For each fiber, among the modes given in Fig. 7.8, the one of the highest order or the second to the highest order is used to generate a Raman soliton at ~2.35 μm, which is about the shortest wavelength where a Raman soliton can be formed. The second to the highest mode order is used only when the highest mode order cannot form a Raman soliton at ~2.35 μm without a strong energy transfer to the Cherenkov radiation. Since the transmission window of InF_3 fiber is up to ~5 μm, the soliton energy at 5 μm is then calculated based on the conservation of the number of photons. Figure 7.9 shows the soliton power scaling results under the self-action limitation. Like in silica fibers, the pulse energies at both ~2.35 μm and 5 μm increase with fiber core diameter, but due to that the

self-action limitation puts the same upper bound on the input pump power for any fiber and any mode, the soliton energy scaling with fiber core diameter slows down, manifesting as the decrease in the peak power of the ~2.35 μm soliton.

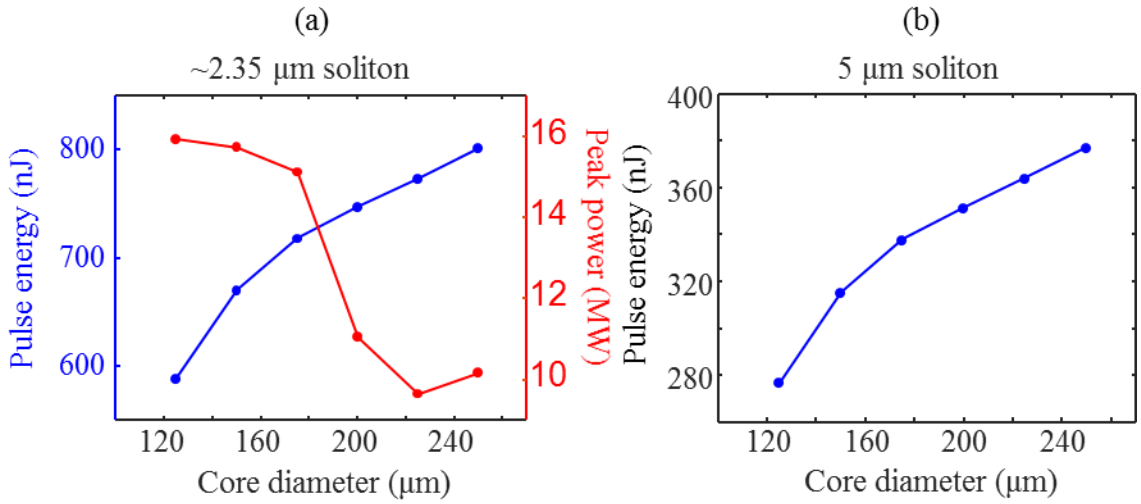

Figure 7.9: (a) The pulse energy and peak power of the ~2.35 μm soliton vs. fiber core diameter. (b) The pulse energy of the ~5 μm soliton vs. fiber core diameter. The limitation is self-action.

All the soliton power values, including both pulse energy and peak power at both ~2.35 μm and 5 μm, are much higher than those in silica fibers given in Sec. 7.1.3. This is because the threshold peak power used in the InF_3 fiber simulation is much higher than that for the silica fiber (12.6 MW vs. 1.46 MW). Currently, the threshold for InF_3 fiber is just a theoretical calculation based on Eq. (7.1). In particle occasions, the real threshold peak power needs to be measured, like in the silica fiber case.

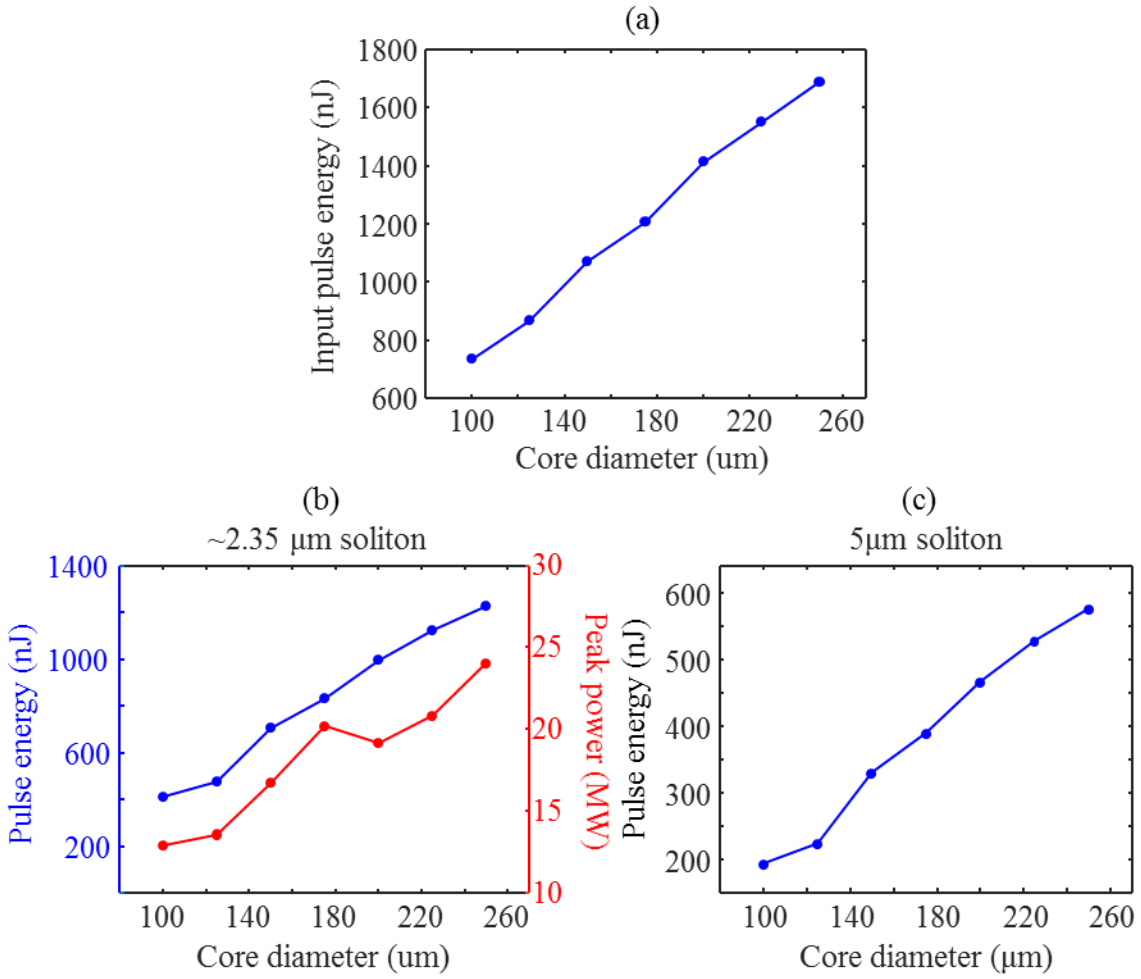

Figure 7.10: The input pulse energy vs. fiber core diameter. (b) The pulse energy and peak power of the ~2.35 μm soliton vs. fiber core diameter. (c) The pulse energy of the 5 μm soliton vs. fiber core diameter. The limitation is dielectric breakdown.

The soliton power scaling simulation under the dielectric breakdown limitation is shown in Fig. 7.10. The allowed pump power increases with fiber core diameter (Fig. 7.10(a)), facilitating a quicker soliton energy scaling than the self-action limitation case. As a result, both pulse energies at ~2.35 μm and 5 μm, and peak power at ~2.35 μm increase with core diameter.

Like in the self-action limitation case, under the dielectric breakdown limitation, all the

soliton powers are much higher than those in silica fibers shown in Sec. 7.1.3. This is partially because the threshold peak intensity for the InF_3 fiber (~5.29×10^3 GW/cm^2) is about twice larger than that for the silica fiber (2.87×10^3 GW/cm^2). The other reason is that the modes used in the InF_3 fiber have much lower order, allowing the use of much higher pump power before damaging the fiber (Fig. 7.10(a)), resulting in much higher soliton pulse energy and peak power than the silica fiber case.

7.3 Summary

This chapter has further explored the soliton power scaling using the DA and pump power scaling strategies in fibers with larger core diameters and/or NA's than what had been shown before, and investigated the limitations on these strategies. The soliton power, including both average power represented by pulse energy and peak power, has been predicted using the pulse propagation simulation and conservation of the number of photons. In addition, the wavelength extension has been discussed. The main conclusions in this chapter are listed below.

1. The DA scaling strategy is limited by fiber NA. Given the highest NA provided by the current silica fiber fabrication techniques, i.e. 0.34, the largest core dimeter is ~175 μm.

2. The pump power scaling strategy is limited by the fiber damage/beam profile distortion. Both self-action and dielectric breakdown could be the underlying mechanism. Under the self-action constraint, the limit of soliton pulse energy at ~1300 nm is ~83 nJ. Under the dielectric breakdown constraint, that is ~168 nJ.

3. By using the MIR fibers, such as fluoride glass and chalcogenide glass fibers, SSFS and

SSMC can be used to achieve wavelength conversion in MIR window. Moreover, with HOMs the conversion process can sweep from NIR to MIR window.

Chapter 8

Summary and Outlook

This chapter summarizes the experimental results described in this thesis, and points out the possible future directions for further research.

8.1 Summary

In this thesis, we have investigated Raman nonlinear effect in multimode fibers (MMFs), and its application in the development of fiber sources for nonlinear microscopy (NM). The behavior of Raman based wavelength conversion in a simple step-index but highly multimoded fiber has been studied, where the recently discovered interpulse intermodal Raman scattering process, i.e. soliton self-mode conversion (SSMC), occurs multiple times during pulse propagation to achieve the wideband wavelength translation. A compact dual color ultrafast fiber source has been developed using the higher order mode (HOM) soliton self-frequency shift (SSFS) process, which may be useful for NM, e.g. CARS/SRS microscopy. In addition, the soliton power scaling and wavelength extension have been discussed. The detailed results are given below.

In the Raman based wavelength translation experiment, a highly multimoded fiber with a core dimeter of 87 μm and numerical aperture (NA) of 0.34 was used. The pump light was launched in the fiber to excite $LP_{0,19}$ mode purely by way of spatial light modulator (SLM) based binary phase plate (BPP). The wavelength translation based on repeatedly alternate SSFS and SSMC processes has been demonstrated. The main results obtained in this

experiment include: (1) both higher input powers and longer fiber lengths keep lowering the mode order, and at the same time red-shifting the soliton wavelength, without loss of spatial coherence; (2) group refractive index matching plays a key role in the intermodal interaction, i.e. SSMC; (3) pump-to-soliton energy conversion efficiencies are ≥ ~30%, and inter-soliton conversion results in the transfer of ~100% of the photons; and (4) the repeatedly alternate SSFS and SSMC processes enable the wavelength translation as much as ~62% of the carrier wavelength (1045-1696 nm), with further translation currently limited by the pump power available in the lab, and ultimately by the self-action/dielectric breakdown effect in the fiber.

Based on the HOM SSFS, a compact dual color femtosecond source has been built, which can be used for CARS/SRS microscopy. The SSFS process is utilized in the Stokes arm, where the energy is converted from the pump wavelength (~1045 nm) to target window (tunable from 1339 nm to 1376 nm). Both input HOM excitation and output HOM reconversion to Gaussian are achieved using commercially available axicons. The output of Stokes arm has pulse energies of ~14.5 nJ and peak powers of ~0.2 MW. The output of pump arm is at ~1045 nm, with pulse energies of ~400 nJ and peak powers of ~4 MW. Compared with the commercially available ultrafast source commonly used for CARS/SRS (Insight X3, Spectra Physics, USA. Pump: 1045 nm, pulse energy: > 44 nJ, peak power: > ~0.2 MW; Stokes: 680-1300 nm, pulse energy: > 19 nJ, peak power: > ~0.2 MW), our source has a comparable peak power in the Stokes arm, and much higher peak power in the pump arm, indicating the improvement of detection sensitivity.

Finally, we studied the soliton power scaling and wavelength extension. The soliton

power can be scaled by dispersion-area (DA) product scaling at the pump wavelength and input pump power scaling. The DA product scaling strategy is limited by fiber NA, given the highest NA obtainable nowadays, i.e. 0.34, the largest core dimeter is ~175 μm. The pump power scaling strategy is limited by fiber damage/beam profile distortion. Both self-action and dielectric breakdown could be the reason. Under self-action constraint, the limit of soliton pulse energy at ~1300 nm is ~83 nJ. Under dielectric breakdown constraint, the limit is ~168 nJ. The SSFS and SSMC processes can be extended to the mid infrared (MIR) window using fluoride glass and chalcogenide glass fibers. The wavelength conversion can sweep from the near infrared (NIR) to MIR window using HOMs in MIR fibers.

Our study indicates SSFS and SSMC in step-index MMFs efficiently generate energetic, ultrafast pulses, covering both NIR and MIR windows. This source can be applied in NM, endoscopy, spectroscopy, chemical sensing, and potentially offer an attractive alternative to bulky solid-state sources, i.e. optical parametric oscillators (OPOs) and optical parametric amplifiers (OPAs).

8.2 Outlook

8.2.1 Further optimization of the compact source

There are several issues in the compact source used for CARS/SRS, consisting of relatively low HOM excitation purity, wavelength instability of the Stokes arm, and the strong relative timing jittering between the pump and Stokes arms. Further efforts are needed to solve or mitigate these issues. For the excitation impurity problem, more lenses should be tested in order to excite the target mode more purely. The ray tracing software, such as

Zemax, is helpful for aberration analysis, choosing the correct lenses, and optimizing the distances between them. As mentioned in chapter 6, the wavelength instability is probably due to the mechanical drifting of input three-dimensional (3D) stage, so a better stage with less drifting can mitigate this problem. One more effective way is to replace the free-space HOM excitation setup with an in-fiber mode conversion device, which is also helpful for pure mode excitation. More details of the use of in-fiber mode converter will be described in section 8.2.2. Regarding the timing jitter issue, as described in chapter 6, the use of a pair of temporally synchronized SSMC modes may provide a fundamental solution to this problem.

8.2.2 Integration of the compact source

The Stokes arm of the fiber source presented in chapter 6 replaces the commonly used SLM-based HOM excitation setup with one commercially available axicon, making the entire source relatively compact, but free-space components, such as mirrors, lenses and 3D stages, are still needed for both HOM excitation and HOM-to-Gaussian conversion, which adds the mechanical drifting induced instability to the source. The wavelength instability over time shown in chapter 6 (Fig. 6.13) is one typical example. Therefore, one main direction to improve the source is to integrate the functions of HOM excitation, wavelength conversion and HOM-to-Gaussian conversion in one all-fiber module, mitigating the complexity of alignment and mechanical drifting. Hence, the in-fiber mode conversion techniques are needed. Several types of in-fiber mode converters have been described in chapter 4, among which only the long period fiber grating (LPFG) has been

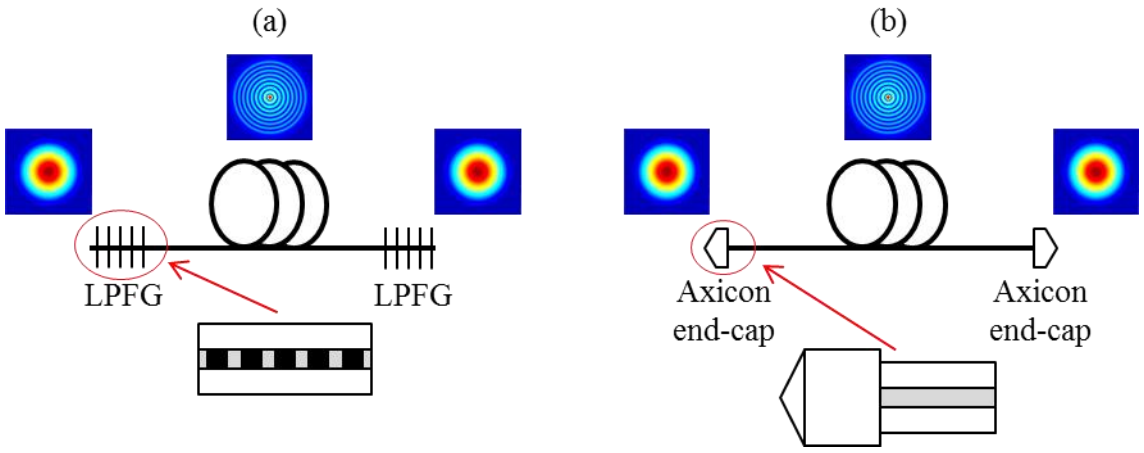

Figure 8.1: (a) Schematic of LPG based integrated module. (b) Schematic of axicon based integrated module.

demonstrated in high power systems (Peng et al., 2013). Figure 8.1(a) shows the schematic of LPFG based module. The fabrication of microaxicon was demonstrated in the past (Eah et al., 2003; Grosjean et al., 2007; Tan et al., 2009). Moreover, the use of axicon fiber endcap has been recently proposed and experimentally demonstrated to realize HOM-to-Gaussian conversion in the HOM amplifier (Nicholson et al., 2015). Compared with LPFGs, the axicon endcaps can handle higher power, because no propagation of small area fundamental mode is involved, and less nonlinear distortion is accumulated in both temporal and spectral domains. Although the demonstrated M^2 of output Gaussian is only ~4, the improvement in manufacture can potentially achieve M^2 of < 1.25 with 80% conversion efficiency. Furthermore, the fiber-tip axicon device has been commercialized (WT&T, Canada). The quality of the product is unknown, but it indicates the fiber based axicon is a promising way of beam shaping, e.g. mode conversion. Figure 8.1(b) shows the schematic of axicon endcap based module. With the all-fiber configuration, endoscopy can be implemented, enabling freely moving animal microscopy.

8.2.3 Further soliton power scaling in silica fibers

The soliton power scaling was discussed in chapter 7. It has been pointed out that the mechanism limiting the pump power scaling strategy cannot be determined based on the data we have, and the pulse energy limit at ~1300 nm has been estimated for both self-action (~83 nJ) and dielectric breakdown (~168 nJ) constraints. Thus, further study is needed to find out the limitation mechanism. If it is determined to be dielectric breakdown, the pulse energy limit can be increased by attaching endcaps to the fiber facets. With endcaps, the original fiber facets become the inside of pulse propagation medium, and are able to handle higher intensity than before. On the new facets, i.e. the facets of endcaps, the effective mode area is larger than that on the original MMF facets, reducing the peak intensity and allowing for higher input pump peak power without damaging fiber. The ultimate pump power limit may be from self-action.

References

Abraham, J. L. and Etz, E. S. (1979). Molecular Microanalysis of Pathological Specimens in Situ with a Laser-Raman Microprobe. *Science* 206(4419): 716-718.

Abramowitz, M. and Stegun, I. A. (1965). *Handbook of Mathematical Functions With Formulas, Graphs, and Mathematical Tables*. Dover.

Agrawal, G. P. (2007). *Nonlinear Fiber Optics (Fourth Edition)*. Academic Press.

Antikainen, A., Tai, B., Rishoj, L., Ramachandran, S. and Agrawal, G. P. (2018). Intermodal Raman Scattering of Ultrashort Pulses in Multimode Fibers. *Conference on Lasers and Electro-Optics (CLEO)*, FTh4E.3.

Avenhaus, M., Eckstein, A., Mosley, P. J. and Silberhorn, C. (2009). Fiber-assisted single-photon spectrograph. *Optics Letters* 34(18): 2873-2875.

Bacskai, B. J., Kajdasz, S. T., Christie, R. H., Carter, C., Games, D., Seubert, P., Schenk, D. and Hyman, B. T. (2001). Imaging of amyloid-beta deposits in brains of living mice permits direct observation of clearance of plaques with immunotherapy. *Nature Medicine* 7(3): 369-372.

Balu, M., Baldacchini, T., Carter, J., Krasieva, T. B., Zadoyan, R. and Tromberg, B. J. (2009). Effect of excitation wavelength on penetration depth in nonlinear optical microscopy of turbid media. *Journal of Biomedical Optics* 14(1).

Barad, Y., Eisenberg, H., Horowitz, M. and Silberberg, Y. (1997). Nonlinear scanning laser microscopy by third harmonic generation. *Applied Physics Letters* 70(8): 922-924.

Basaldua, I., Kuis, R., Burkins, P., Jiang, Z. and Johnson, A. M. (2018). Measurements of the Nonlinear Refractive Index (n2) for Indium Fluoride (InF3) Bulk Glass and Fiber. *Frontiers in Optics /Laser Science*, JTu3A.38.

Baumgartl, M., Lecaplain, C., Hideur, A., Limpert, J. and Tunnermann, A. (2012). 66 W average power from a microjoule-class sub-100 fs fiber oscillator. *Optics Letters* 37(10): 1640-1642.

Beaud, P., Hodel, W., Zysset, B. and Weber, H. P. (1987). Ultrashort Pulse-Propagation, Pulse Breakup, and Fundamental Soliton Formation in a Single-Mode Optical Fiber. *IEEE Journal of Quantum Electronics* 23(11): 1938-1946.

Bozinovic, N., Golowich, S., Kristensen, P. and Ramachandran, S. (2012). Control of orbital angular momentum of light with optical fibers. *Optics Letters* 37(13): 2451-2453.

Bozinovic, N., Yue, Y., Ren, Y. X., Tur, M., Kristensen, P., Huang, H., Willner, A. E. and Ramachandran, S. (2013). Terabit-Scale Orbital Angular Momentum Mode Division Multiplexing in Fibers. *Science* 340(6140): 1545-1548.

Campagnola, P. J. and Loew, L. M. (2003). Second-harmonic imaging microscopy for visualizing biomolecular arrays in cells, tissues and organisms. *Nature Biotechnology* 21(11): 1356-1360.

Chalfie, M., Tu, Y., Euskirchen, G., Ward, W. W. and Prasher, D. C. (1994). Green Fluorescent Protein as a Marker for Gene-Expression. *Science* 263(5148): 802-805.

Chiao, R. Y., Garmire, E. and Townes, C. H. (1964). Self-Trapping of Optical Beams. *Physics Review Letters* 13(15): 479-482.

Chong, A., Buckley, J., Renninger, W. and Wise, F. (2006). All-normal-dispersion femtosecond fiber laser. *Optics Express* 14(21): 10095-10100.

Chung, H. Y., Liu, W., Cao, Q., Song, L. W., Kartner, F. X. and Chang, G. Q. (2018). Megawatt peak power tunable femtosecond source based on self-phase modulation enabled spectral selection. *Optics Express* 26(3): 3684-3695.

Cohen, L. G. (1985). Comparison of Single-Mode Fiber Dispersion Measurement Techniques. *Journal of Lightwave Technology* 3(5): 958-966.

Combs, C. A. and Shroff, H. (2017). Fluorescence Microscopy: A Concise Guide to Current Imaging Methods. *Current Protocols in Neuroscience* 79: 2.1.1-2.1.25.

Cormack, I. G., Reid, D. T., Wadsworth, W. J., Knight, J. C. and Russell, P. S. J. (2002). Observation of soliton self-frequency shift in photonic crystal fibre. *Electronics Letters* 38(4): 167-169.

Davis, D. D., Gaylord, T. K., Glytsis, E. N., Kosinski, S. G., Mettler, S. C. and Vengsarkar, A. M. (1998). Long-period fibre grating fabrication with focused CO2 laser pulses. *Electronics Letters* 34(3): 302-303.

Demas, J., Prabhakar, G., He, T. and Ramachandran, S. (2017). Wavelength-agile high-power sources via four-wave mixing in higher-order fiber modes. *Optics Express* 25(7): 7455-7464.

Demas, J. and Ramachandran, S. (2014). Sub-second mode measurement of fibers using C-2 imaging. *Optics Express* 22(19): 23043-23056.

Demas, J., Rishoj, L., Liu, X., Prabhakar, G. and Ramachandran, S. (2018). Intermodal group velocity engineering for broadband nonlinear optics. *arXiv*: 1806.02902.

Demas, J., Rishoj, L. and Ramachandran, S. (2015). Free-space beam shaping for precise control and conversion of modes in optical fiber. *Optics Express* 23(22): 28531-28545.

Denk, W., Strickler, J. H. and Webb, W. W. (1990). Two-Photon Laser Scanning Fluorescence Microscopy. *Science* 248(4951): 73-76.

Dudley, J. M., Genty, G. and Coen, S. (2006). Supercontinuum generation in photonic crystal fiber. *Reviews of Modern Physics* 78(4): 1135-1184.

Dudley, J. M. and Taylor, J. R. (2010). *Supercontinuum Generation in Optical Fibers*. Cambridge University Press.

Duncan, M. D., Reintjes, J. and Manuccia, T. J. (1982). Scanning Coherent Anti-Stokes Raman Microscope. *Optics Letters* 7(8): 350-352.

Eah, S. K., Jhe, W. and Arakawa, Y. (2003). Nearly diffraction-limited focusing of a fiber axicon microlens. *Review of Scientific Instruments* 74(11): 4969-4971.

Erdogan, T. (1997). Fiber grating spectra. *Journal of Lightwave Technology* 15(8): 1277-1294.

Fibich, G. and Gaeta, A. L. (2000). Critical power for self-focusing in bulk media and in hollow waveguides. *Optics Letters* 25(5): 335-337.

Fini, J. M. and Ramachandran, S. (2007). Natural bend-distortion immunity of higher-order-mode large-mode-area fibers. *Optics Letters* 32(7): 748-750.

Fludger, C. R. S. and Mears, R. J. (2001). Electrical measurements of multipath interference in distributed Raman amplifiers. *Journal of Lightwave Technology* 19(4): 536-545.

Freudiger, C. W., Min, W., Saar, B. G., Lu, S., Holtom, G. R., He, C. W., Tsai, J. C., Kang, J. X. and Xie, X. S. (2008). Label-Free Biomedical Imaging with High Sensitivity by Stimulated Raman Scattering Microscopy. *Science* 322(5909): 1857-1861.

Freund, I. and Deutsch, M. (1986). 2nd-Harmonic Microscopy of Biological Tissue. *Optics Letters* 11(2): 94-96.

Ghatak, A. and Thyagarajan, K. (1998). *Introduction to Fiber Optics*. Cambridge University Press.

Gobel, W., Nimmerjahn, A. and Helmchen, F. (2004). Distortion-free delivery of nanojoule femtosecond pulses from a Ti : sapphire laser through a hollow-core photonic crystal fiber. *Optics Letters* 29(11): 1285-1287.

Gordon, J. P. (1986). Theory of the Soliton Self-Frequency Shift. *Optics Letters* 11(10): 662-664.

Gottschall, T., Meyer, T., Schmitt, M., Popp, J., Limpert, J. and Tunnermann, A. (2015). Four-wave-mixing-based optical parametric oscillator delivering energetic, tunable, chirped femtosecond pulses for non-linear biomedical applications. *Optics Express* 23(18): 23968-23977.

Gregg, P., Kristensen, P. and Ramachandran, S. (2016). 13.4km OAM state propagation by recirculating fiber loop. *Optics Express* 24(17): 18938-18947.

Grosjean, T., Saleh, S. S., Suarez, M. A., Ibrahim, I. A., Piquerey, V., Charraut, D. and Sandoz, P. (2007). Fiber microaxicons fabricated by a polishing technique for the generation of Bessel-like beams. *Applied Optics* 46(33): 8061-8067.

Gryczynski, I., Szmacinski, H. and Lakowicz, J. R. (1995). On the possibility of calcium imaging using Indo-1 with three-photon excitation. *Photochemistry and Photobiology* 62(4): 804-808.

Hadley, G. R. (2008). High-power pulse propagation in optical fibers. *2008 Conference on Optical Fiber Communication/National Fiber Optic Engineers Conference, Vols 1-8*: 2176-2178.

Haus, H. A. (1966). Higher Order Trapped Light Beam Solutions - (Analog Computer Solution T). *Applied Physics Letters* 8(5): 128-129.

Heim, R., Cubitt, A. B. and Tsien, R. Y. (1995). Improved Green Fluorescence. *Nature* 373(6516): 663-664.

Helmchen, F. and Denk, W. (2005). Deep tissue two-photon microscopy. *Nature Methods* 2(12): 932-940.

Helmchen, F., Denk, W. and Kerr, J. N. (2013). Miniaturization of two-photon microscopy for imaging in freely moving animals. *Cold Spring Harbor Protocols* 2013(10): 904-913.

Hill, K. O., Fujii, Y., Johnson, D. C. and Kawasaki, B. S. (1978). Photosensitivity in Optical Fiber Waveguides: Application to Reflection Filter Fabrication. *Applied Physics Letters* 32(10): 647-649.

Horton, N. G., Wang, K., Kobat, D., Clark, C. G., Wise, F. W., Schaffer, C. B. and Xu, C. (2013). In vivo three-photon microscopy of subcortical structures within an intact mouse brain. *Nature Photonics* 7(3): 205-209.

Hwang, I. K., Yun, S. H. and Kim, B. Y. (1999). Long-period fiber gratings based on periodic microbends. *Optics Letters* 24(18): 1263-1265.

Ippen, E. P., Shank, C. V. and Gustafso.Tk (1974). Self-Phase Modulation of Picosecond Pulses in Optical Fibers. *Applied Physics Letters* 24(4): 190-192.

Kashyap, R. (1999). *Fiber Bragg Gratings*. Academic Press.

Kieu, K., Renninger, W. H., Chong, A. and Wise, F. W. (2009). Sub-100 fs pulses at watt-level powers from a dissipative-soliton fiber laser. *Optics Letters* 34(5): 593-595.

Kim, H. S., Yun, S. H., Kwang, I. K. and Kim, B. Y. (1997). All-fiber acousto-optic tunable notch filter with electronically controllable spectral profile. *Optics Letters* 22(19): 1476-1478.

Kim, W. H., Nguyen, V. Q., Shaw, L. B., Busse, L. E., Florea, C., Gibson, D. J., Gattass, R. R., Bayya, S. S., Kung, F. H., Chin, G. D., Miklos, R. E., Aggarwal, I. D. and Sanghera, J. S. (2016). Recent progress in chalcogenide fiber technology at NRL. *Journal of Non-Crystalline Solids* 431: 8-15.

Kobat, D., Durst, M. E., Nishimura, N., Wong, A. W., Schaffer, C. B. and Xu, C. (2009). Deep tissue multiphoton microscopy using longer wavelength excitation. *Optics Express* 17(16): 13354-13364.

Kobat, D., Horton, N. G. and Xu, C. (2011). In vivo two-photon microscopy to 1.6-mm depth in mouse cortex. *Journal of Biomedical Optics* 16(10).

Krupa, K., Tonello, A., Shalaby, B. M., Fabert, M., Barthelemy, A., Millot, G., Wabnitz, S. and Couderc, V. (2017). Spatial beam self-cleaning in multimode fibres. *Nature Photonics* 11(4): 237-U299.

Lai, K., Leon-Saval, S. G., Witkowska, A., Wadsworth, W. J. and Birks, T. A. (2007). Wavelength-independent all-fiber mode converters. *Optics Letters* 32(4): 328-330.

Lee, J. H., van Howe, J., Xu, C. and Liu, X. (2008). Soliton self-frequency shift: Experimental demonstrations and applications. *IEEE Journal of Selected Topics in Quantum Electronics* 14(3): 713-723.

Lefrancois, S., Kieu, K., Deng, Y. J., Kafka, J. D. and Wise, F. W. (2010). Scaling of dissipative soliton fiber lasers to megawatt peak powers by use of large-area photonic crystal fiber. *Optics Letters* 35(10): 1569-1571.

Lichtman, J. W. and Conchello, J. A. (2005). Fluorescence microscopy. *Nature Methods* 2(12): 910-919.

Lim, H., Buckley, J., Chong, A. and Wise, F. W. (2004). Fibre-based source of femtosecond pulses tunable from 1.0 to 1.3 mu m. *Electronics Letters* 40(24): 1523-1525.

Lin, C., Tynes, A. R., Tomita, A., Liu, P. L. and Philen, D. L. (1983). Chromatic Dispersion Measurements in Single-Mode Fibers Using Picosecond InGaAsP Injection Lasers in the 1.2- to 1.5-μm Spectral Region. *Bell Labs Technical Journal* 62(2): 457-462.

Liu, G. J., Kieu, K., Wise, F. W. and Chen, Z. P. (2011). Multiphoton microscopy system with a compact fiber-based femtosecond-pulse laser and handheld probe. *Journal of Biophotonics* 4(1-2): 34-39.

Liu, W., Chia, S. H., Chung, H. Y., Greinert, R., Kartner, F. X. and Chang, G. Q. (2017). Energetic ultrafast fiber laser sources tunable in 1030-1215 nm for deep tissue multi-photon microscopy. *Optics Express* 25(6): 6822-6831.

Liu, W., Li, C., Zhang, Z. G., Kartner, F. X. and Chang, G. Q. (2016). Self-phase modulation enabled, wavelength-tunable ultrafast fiber laser sources: an energy scalable approach. *Optics Express* 24(14): 15328-15340.

Liu, X., Xu, C., Knox, W. H., Chandalia, J. K., Eggleton, B. J., Kosinski, S. G. and Windeler, R. S. (2001). Soliton self-frequency shift in a short tapered air-silica microstructure fiber. *Optics Letters* 26(6): 358-360.

Lu, R. W., Sun, W. Z., Liang, Y. J., Kerlin, A., Bierfeld, J., Seelig, J. D., Wilson, D. E., Scholl, B., Mohar, B., Tanimoto, M., Koyama, M., Fitzpatrick, D., Orger, M. B. and Ji, N. (2017). Video-rate volumetric functional imaging of the brain at synaptic resolution. *Nature Neuroscience* 20(4): 620-628.

Marcuse, D. (1982). Influence of Curvature on the Losses of Doubly Clad Fibers. *Applied Optics* 21(23): 4208-4213.

Marhic, M. E., Kagi, N., Chiang, T. K. and Kazovsky, L. G. (1996). Broadband fiber optical parametric amplifiers. *Optics Letters* 21(8): 573-575.

McGloin, D. and Dholakia, K. (2005). Bessel beams: Diffraction in a new light. *Contemporary Physics* 46(1): 15-28.

Menashe, D., Tur, M. and Danziger, Y. (2001). Interferometric technique for measuring dispersion of high order modes in optical fibres. *Electronics Letters* 37(24): 1439-1440.

Michalska, M., Mikolajczyk, J., Wojtas, J. and Swiderski, J. (2016). Mid-infrared, super-flat, upercontinuum generation overing the 2–5 μm spectral band sing a fluoroindate fibre pumped with picosecond pulses. *Scientific Reports*: 6:39138.

Minsky, M. (1957). Microscopy apparatus. U. S. Patent Office. US3013467A.

Mitschke, F. M. and Mollenauer, L. F. (1986). Discovery of the Soliton Self-Frequency Shift. *Optics Letters* 11(10): 659-661.

Mollenauer, L. F., Stolen, R. H. and Gordon, J. P. (1980). Experimental-Observation of Picosecond Pulse Narrowing and Solitons in Optical Fibers. *Physical Review Letters* 45(13): 1095-1098.

Negus, D. K., Spinelli, L., Goldblatt, N. and Feuget, G. (1991). Sub-100 fs pulse generation by Kerr lens modelocking in Ti: Al203. *Advanced Solid State Lasers*, SPL7.

Nicholson, J. W., DeSantolo, A., Westbrook, P. S., Windeler, R. S., Kremp, T., Headley, C. and DiGiovanni, D. J. (2015). Axicons for mode conversion in high peak power, higher-order mode, fiber amplifiers. *Optics Express* 23(26): 33849-33860.

Nicholson, J. W., Fini, J. M., DeSantolo, A. M., Liu, X., Feder, K., Westbrook, P. S., Supradeepa, V. R., Monberg, E., DiMarcello, F., Ortiz, R., Headley, C. and DiGiovanni, D. J. (2012). Scaling the effective area of higher-order-mode erbium-doped fiber amplifiers. *Optics Express* 20(22): 24575-24584.

Oheim, M., Beaurepaire, E., Chaigneau, E., Mertz, J. and Charpak, S. (2001). Two-photon microscopy in brain tissue: parameters influencing the imaging depth. *Journal of Neuroscience Methods* 111(1): 29-37.

Ouzounov, D. G., Moll, K. D., Foster, M. A., Zipfel, W. R., Webb, W. W. and Gaeta, A. L. (2002). Delivery of nanojoule femtosecond pulses through large-core microstructured fibers. *Optics Letters* 27(17): 1513-1515.

Ouzounov, D. G., Wang, T. Y., Wang, M. R., Feng, D. D., Horton, N. G., Cruz-Hernandez, J. C., Cheng, Y. T., Reimer, J., Tolias, A. S., Nishimura, N. and Xu, C. (2017). In vivo three-photon imaging of activity of GCaMP6-labeled neurons deep in intact mouse brain. *Nature Methods* 14(4): 388-390.

Ozbay, B. N., Futia, G. L., Ma, M., Bright, V. M., Gopinath, J. T., Hughes, E. G., Restrepo, D. and Gibson, E. A. (2018). Three dimensional two-photon brain imaging in freely moving mice using a miniature fiber coupled microscope with active axial-scanning. *Scientific Reports* 8.

Paschotta, R., Nilsson, J., Tropper, A. C. and Hanna, D. C. (1997). Ytterbium-doped fiber amplifiers. *IEEE Journal of Quantum Electronics* 33(7): 1049-1056.

Pawley, J. B. (2006). *Handbook of Biological Confocal Microscopy*. Springer Science+Business Media.

Peng, X., Kim, K., Mielke, M., Booth, T., Nicholson, J. W., Fini, J. M., Liu, X. P., DeSantolo, A., Westbrook, P. S., Windeler, R. S., Monberg, E. M., DiMarcello, F. V., Headley, C. and DiGiovanni, D. J. (2013). Higher-order mode fiber enables high energy chirped-pulse amplification. *Optics Express* 21(26): 32411-32416.

Planas, S. A., Mansur, N. L. P., Cruz, C. H. B. and Fragnito, H. L. (1993). Spectral Narrowing in the Propagation of Chirped Pulses in Single-Mode Fibers. *Optics Letters* 18(9): 699-701.

Ploetz, E., Laimgruber, S., Berner, S., Zinth, W. and Gilch, P. (2007). Femtosecond stimulated Raman microscopy. *Applied Physics B-Lasers and Optics* 87(3): 389-393.

Poletti, F. and Horak, P. (2008). Description of ultrashort pulse propagation in multimode optical fibers. *Journal of the Optical Society of America B-Optical Physics* 25(10): 1645-1654.

Prabhakar, G., Gregg, P., Rishoj, L. and Ramachandran, S. (2016). In-Fiber Monomode Octave-Spanning OAM Supercontinuum. *Conference on Lasers and Electro-Optics (CLEO)*, AM4J.3.

Prabhakar, G., Liu, X., Demas, J., Gregg, P. and Ramachandran, S. (2018). Phase Conjugation in OAM fiber modes via Stimulated Brillouin Scattering. *Conference on Lasers and Electro-Optics (CLEO)*, FTh1M.4.

Ramachandran, S. (2005). Dispersion-tailored few-mode fibers: A versatile platform for in-fiber photonic devices. *Journal of Lightwave Technology* 23(11): 3426-3443.

Ramachandran, S., Fini, J. M., Mermelstein, M., Nicholson, J. W., Ghalmi, S. and Yan, M. F. (2008). Ultra-large effective-area, higher-order mode fibers: a new strategy for high-power lasers. *Laser & Photonics Reviews* 2(6): 429-448.

Ramachandran, S., Ghalmi, S., Nicholson, J. W., Yan, M. F., Wisk, P., Monberg, E. and Dimarcello, F. V. (2006a). Anomalous dispersion in a solid, silica-based fiber. *Optics Letters* 31(17): 2532-2534.

Ramachandran, S. and Kristensen, P. (2013). Optical vortices in fiber. *Nanophotonics* 2(5-6): 455-474.

Ramachandran, S., Nicholson, J. W., Ghalmi, S. and Yan, M. F. (2003). Measurement of multipath interference in the coherent crosstalk regime. *IEEE Photonics Technology Letters* 15(8): 1171-1173.

Ramachandran, S., Nicholson, J. W., Ghalmi, S., Yan, M. F., Wisk, P., Monberg, E. and Dimarcello, F. V. (2006b). Light propagation with ultralarge modal areas in optical fibers. *Optics Letters* 31(12): 1797-1799.

Ramachandran, S., Wang, Z. Y. and Yan, M. (2002). Bandwidth control of long-period grating-based mode converters in few-mode fibers. *Optics Letters* 27(9): 698-700.

Ramachandran, S., Yan, M. F., Jasapara, J., Wisk, P., Ghalmi, S., Monberg, E. and Dimarcello, F. V. (2005). High-energy (nanojoule) femtosecond pulse delivery with record dispersion higher-order mode fiber. *Optics Letters* 30(23): 3225-3227.

Rishoj, L., Prabhakar, G., Demas, J. and Ramachandran, S. (2016). 30 nJ, similar to 50 fs All-Fiber Source at 1300 nm using Soliton Shifting in LMA HOM Fiber. *Conference on Lasers and Electro-Optics (CLEO)*, STh3O.3.

Rishoj, L., Tai, B., Kristensen, P. and Ramachandran, S. (2018). Discovery of Soliton Self-Mode Conversion in Multimode Optical Fibers. *arXiv*: 1805.06037.

Shimomura, O., Johnson, F. H. and Saiga, Y. (1962). Extraction, purification and properties of aequorin, a bioluminescent protein from the luminous hydromedusan, Aequorea. *Journal of Cellular and Comparative Physiology* 59(3): 223-239.

Skryabin, D. V., Luan, F., Knight, J. C. and Russell, P. S. (2003). Soliton self-frequency shift cancellation in photonic crystal fibers. *Science* 301(5640): 1705-1708.

Snyder, A. W. and Love, J. D. (1983). *Optical Waveguide and Theory*. Chapman and Hall.

Spence, D. E., Kean, P. N. and Sibbett, W. (1991). 60-Fsec Pulse Generation from a Self-Mode-Locked Ti-Sapphire Laser. *Optics Letters* 16(1): 42-44.

Steinvurzel, P., Tantiwanichapan, K., Goto, M. and Ramachandran, S. (2011). Fiber-based Bessel beams with controllable diffraction-resistant distance. *Optics Letters* 36(23): 4671-4673.

Stolen, R. H. (1975). Phase-Matched-Stimulated 4-Photon Mixing in Silica-Fiber Waveguides. *IEEE Journal of Quantum Electronics* Qe11(3): 100-103.

Stolen, R. H., Bjorkholm, J. E. and Ashkin, A. (1974). Phase-Matched 3-Wave Mixing in Silica Fiber Optical-Waveguides. *Applied Physics Letters* 24(7): 308-310.

Stolen, R. H. and Ippen, E. P. (1973). Raman Gain in Glass Optical Waveguides. *Applied Physics Letters* 22(6): 276-278.

Stuart, B. C., Feit, M. D., Rubenchik, A. M., Shore, B. W. and Perry, M. D. (1995). Laser-Induced Damage in Dielectrics with Nanosecond to Subpicosecond Pulses. *Physical Review Letters* 74(12): 2248-2251.

Taddeucci, A., Martelli, F., Barilli, M., Ferrari, M. and Zaccanti, G. (1996). Optical properties of brain tissue. *Journal of Biomedical Optics* 1(1): 117-123.

Takayanagi, J., Sugiura, T., Yoshida, M. and Nishizawa, N. (2006). 1.0-1.7-mu m wavelength-tunable ultrashort-pulse generation using femtosecond Yb-doped fiber laser and photonic crystal fiber. *IEEE Photonics Technology Letters* 18(21-24): 2284-2286.

Tan, K. M., Mazilu, M., Chow, T. H., Lee, W. M., Taguchi, K., Ng, B. K., Sibbett, W., Herrington, C. S., Brown, C. T. A. and Dholakia, K. (2009). In-fiber common-path optical coherence tomography using a conical-tip fiber. *Optics Express* 17(4): 2375-2384.

Theer, P. and Denk, W. (2006). On the fundamental imaging-depth limit in two-photon microscopy. *Journal of the Optical Society of America A-Optics Image Science and Vision* 23(12): 3139-3149.

Theer, P., Hasan, M. T. and Denk, W. (2003). Two-photon imaging to a depth of 1000 mu m in living brains by use of a Ti : Al2O3 regenerative amplifier. *Optics Letters* 28(12): 1022-1024.

Tsien, R. Y. (1998). The green fluorescent protein. *Annual Review of Biochemistry* 67: 509-544.

Tsuchida, Y., Saitoh, K. and Koshiba, M. (2005). Design and characterization of single-mode holey fibers with low bending losses. *Optics Express* 13(12): 4770-4779.

van Howe, J., Lee, J. H., Zhou, S., Wise, F., Xu, C., Ramachandran, S., Ghalmi, S. and Yan, M. F. (2007). Demonstration of soliton self-frequency shift below 1300 nm in higher-order mode, solid silica-based fiber. *Optics Letters* 32(4): 340-342.

Wang, J., Yang, J. Y., Fazal, I. M., Ahmed, N., Yan, Y., Huang, H., Ren, Y. X., Yue, Y., Dolinar, S., Tur, M. and Willner, A. E. (2012). Terabit free-space data transmission employing orbital angular momentum multiplexing. *Nature Photonics* 6(7): 488-496.

Wei, L., Chen, Z. X., Shi, L. X., Long, R., Anzalone, A. V., Zhang, L. Y., Hu, F. H., Yuste, R., Cornish, V. W. and Min, W. (2017). Super-multiplex vibrational imaging. *Nature* 544(7651): 465-470.

Weigelin, B., Bakker, G. J. and Friedl, P. (2016). Third harmonic generation microscopy of cells and tissue organization. *Journal of Cell Science* 129(2): 245-255.

Wise, F. W. (2012). Femtosecond Fiber Lasers Based on Dissipative Processes for Nonlinear Microscopy. *IEEE Journal of Selected Topics in Quantum Electronics* 18(4): 1412-1421.

Wright, L. G., Christodoulides, D. N. and Wise, F. W. (2015). Controllable spatiotemporal nonlinear effects in multimode fibres. *Nature Photonics* 9(5): 306-310.

Xu, C. and Wise, F. W. (2013). Recent advances in fibre lasers for nonlinear microscopy. *Nature Photonics* 7(11): 875-882.

Yan, L., Kristensen, P. and Ramachandran, S. (2016). All-fiber STED microscopy illumination system. *Conference on Lasers and Electro-Optics (CLEO)*, SM4P.3.

Yilmaz, Y. O., Mehta, A., Mohammed, W. S. and Johnson, E. G. (2007). Fiber-optic beam shaper based an multimode interference. *Optics Letters* 32(21): 3170-3172.

Youngquist, R. C., Brooks, J. L. and Shaw, H. J. (1984). 2-Mode Fiber Modal Coupler. *Optics Letters* 9(5): 177-179.

Zhang, C. and Cheng, J. X. (2018). Perspective: Coherent Raman scattering microscopy, the future is bright. *Applied Photonics* 3(9).

Zhou, G. J., Xin, M., Kaertner, F. X. and Chang, G. Q. (2015). Timing jitter of Raman solitons. *Optics Letters* 40(21): 5105-5108.

Zumbusch, A., Holtom, G. R. and Xie, X. S. (1999). Three-dimensional vibrational imaging by coherent anti-Stokes Raman scattering. *Physical Review Letters* 82(20): 4142-4145.

Curriculum Vitae